Bioactive Materials 15 (2022) 214–249

Contents lists available at ScienceDirect

Bioactive Materials

journal homepage: www.keaipublishing.com/en/journals/bioactive-materials

Additively manufactured metallic biomaterials

Elham Davoodi [a,b,c,d], Hossein Montazerian [b,c,d], Anooshe Sadat Mirhakimi [e], Masoud Zhianmanesh [f], Osezua Ibhadode [a], Shahriar Imani Shahabad [a], Reza Esmaeilizadeh [a], Einollah Sarikhani [g], Sahar Toorandaz [a], Shima A. Sarabi [h], Rohollah Nasiri [d], Yangzhi Zhu [d], Javad Kadkhodapour [i,j], Bingbing Li [k,d], Ali Khademhosseini [d,**], Ehsan Toyserkani [a,*]

[a] Multi-Scale Additive Manufacturing (MSAM) Laboratory, Mechanical and Mechatronics Engineering Department, University of Waterloo, Waterloo, Ontario N2L 3G1, Canada
[b] Department of Bioengineering, University of California, Los Angeles, California 90095, United States
[c] California NanoSystems Institute (CNSI), University of California, Los Angeles, California 90095, United States
[d] Terasaki Institute for Biomedical Innovation, Los Angeles, California 90024, United States
[e] Department of Mechanical Engineering, Isfahan University of Technology, Isfahan, Isfahan 84156-83111, Iran
[f] School of Biomedical Engineering, University of Sydney, Sydney, New South Wales 2006, Australia
[g] Department of Nanoengineering, Jacobs School of Engineering, University of California, San Diego, California 92093, United States
[h] Mechanical and Aerospace Engineering Department, University of California, Los Angeles, California 90095, United States
[i] Department of Mechanical Engineering, Shahid Rajaee Teacher Training University, Tehran, Tehran 16785-163, Iran
[j] Institute for Materials Testing, Materials Science and Strength of Materials, University of Stuttgart, Stuttgart 70569, Germany
[k] Department of Manufacturing Systems Engineering and Management, California State University, Northridge, California 91330, United States

ARTICLE INFO

Keywords:
Additive manufacturing
Metal implant
Porous scaffold
Tissue engineering
Biomaterials

ABSTRACT

Metal additive manufacturing (AM) has led to an evolution in the design and fabrication of hard tissue substitutes, enabling personalized implants to address each patient's specific needs. In addition, internal pore architectures integrated within additively manufactured scaffolds, have provided an opportunity to further develop and engineer functional implants for better tissue integration, and long-term durability. In this review, the latest advances in different aspects of the design and manufacturing of additively manufactured metallic biomaterials are highlighted. After introducing metal AM processes, biocompatible metals adapted for integration with AM machines are presented. Then, we elaborate on the tools and approaches undertaken for the design of porous scaffold with engineered internal architecture including, topology optimization techniques, as well as unit cell patterns based on lattice networks, and triply periodic minimal surface. Here, the new possibilities brought by the functionally gradient porous structures to meet the conflicting scaffold design requirements are thoroughly discussed. Subsequently, the design constraints and physical characteristics of the additively manufactured constructs are reviewed in terms of input parameters such as design features and AM processing parameters. We assess the proposed applications of additively manufactured implants for regeneration of different tissue types and the efforts made towards their clinical translation. Finally, we conclude the review with the emerging directions and perspectives for further development of AM in the medical industry.

1. Introduction

Traumatic injuries, congenital defects, and cancer are increasingly growing the need for hard tissue replacements each year [1]. The standardized conventional metal implants are currently used for the fixation and replacement of those tissue types. These implants suffer from poor integration with the host tissue, leading to more advanced complications including implant failure and rejection, which eventually raise the need for burdensome revision surgeries. The advent of additive manufacturing (AM) has opened new avenues towards patient-specific implants to meet the customized needs of individual patients [2]. The AM-based approaches enabled manufacturability of multifunctional

Peer review under responsibility of KeAi Communications Co., Ltd.
* Corresponding author.
** Corresponding author.
E-mail addresses: khademh@terasaki.org (A. Khademhosseini), ehsan.toyserkani@uwaterloo.edu (E. Toyserkani).

https://doi.org/10.1016/j.bioactmat.2021.12.027
Received 6 October 2021; Received in revised form 17 December 2021; Accepted 21 December 2021
Available online 30 December 2021

complex-shaped implants with the engineered osteoconductive interconnected porous architectures which could not be fabricated through the traditional methods. These properties have led to the quick growth of AM in the areas of dental, craniofacial, spinal cord, and skeletal bone regeneration. In these applications, AM techniques aim to mimic the lost bone tissue more precisely in terms of physical, mechanical, chemical, and biological properties. The AM techniques offer versatility in terms of material choice. Metallic biomaterials such as titanium (Ti), tantalum (Ta), cobalt-chromium, *etc.* have been adopted for the fabrication of surgical tools and medical implants due to their biocompatibility [3], high fracture toughness [4], tunable stiffness for matching with the host tissue, high wear and corrosion resistance [5]. Hence, an ongoing effort is made to advance multiple aspects of AM in biomedical sectors including AM technology development, physical and chemical biomaterial design for AM, as well as optimization of quality control and structural performance of the AM parts.

Many studies have focused on the synergy between design optimization and AM processes. Recent advances have resulted in topology optimization procedures for AM to address multiple physical and biological design criteria for successful bone regeneration and tissue integration within porous implants [6,7]. The mismatch between mechanical properties of the host tissue and fabricated implants, known as stress shielding, causes serious issues such as osteopenia and implant loosening [8]. With the aid of topology optimization methods, metallic implants are aimed to mimic physical properties of the host tissue by introducing designed macropores within the solid implants [9]. The design of internal pore architecture in porous implants not only enables engineering of the physical and mechanical performance but also controls biopermeability for cell integration [10]. Due to the contradictory design criteria for mechanical enhancement and biopermeability, a surge of interest has been directed towards functionally graded microporosity as a potential solution to mechanobiological design problems [11].

Manufacturing defects drive another class of research towards improving the structural quality of the medical AM parts. Geometrical deviations or microstructural imperfections may be induced in additively manufactured parts [12]. These imperfections are originated from improper AM process parameters or metal powder impurity. The AM defects can deteriorate the mechanical properties of the implants including decreased fatigue life and diminish the impact performance of the implant. Hence, quality control techniques for inspecting the manufactured parts for any defects as well as *in situ* monitoring during the AM process are necessary [13,14]. In addition, physical and chemical surface characteristics of the AM parts govern the cell interactions, and thereby, they have been paid significant attention in the recent literature. Surface engineering principles and processing techniques have been conducted in multiple examples for improving bone regeneration and cell adhesion to the AM medical parts [15]. To meet the above-mentioned requirements simultaneously, proper material selection, design optimization, and advanced manufacturing techniques should be implemented which requires a deep multidisciplinary insight into the structure-property relationships from both physical and biological perspectives.

With this picture in mind, the current review comprehensively discusses the latest literature engaging the metal AM techniques for the development of functional implants. First, we focus on the fundamentals of the well-known AM techniques and metallic biomaterials employed for this purpose. Then, various design procedures used to define internal pore shapes in additively manufactured porous implants are highlighted in the context of their mechanical and biological responses. The typical structural defects observed in the additively manufactured implants and the implant's responses in various physiological conditions such as fatigue and impact are discussed. Then, applications of various types of implants in regenerative medicine as well as the clinical translation approaches are discussed. Finally, we conclude the review and elaborate on the future perspectives and opportunities for improvement.

2. Metal additive manufacturing technologies

The AM technologies for the fabrication of metallic structures rely on the local binding of metal powders (using a binder, or *via* sintering approaches) in a layer-by-layer fashion. The metal AM techniques have been capable to form fine features at certain levels for biomedical purposes. Those features, as defined during the computer-aided design (CAD) modeling, are the basis for the selection of a suitable technique for implant fabrication. The CAD models prepared in a proper AM format, such as stereolithography (STL), are converted to 2D slices to determine the scanning toolpath for local solidification. Subsequently, AM processes can be used to manufacture the designed models. In the following sections, the most widely used AM techniques for the fabrication of metallic biomaterials are introduced.

2.1. Powder bed fusion

Powder bed fusion (PBF) is one of the most popular classes widely used in the fabrication of implants. The PBF processes can produce excellent dimensional accuracy at high relative densities [16,17] often with high surface roughness and acceptable repeatability [18]. In this process, the powder left over from the process can be recycled for further use. Some of the major limitations of PBF processes include high residual stresses, generally anisotropic properties, difficult depowdering, especially when it comes to small size channels, powder agglomeration inside small conformal channels, and long print time [19]. There are two popular AM processes under PBF: laser PBF and electron-beam PBF.

2.1.1. Laser powder bed fusion

Laser powder bed fusion (LPBF), also known as selective laser melting (SLM) or direct metal laser sintering (DMLS), is the most frequently used AM technique for fabrication of the metal implants (Fig. 1A). The LPBF process begins with spreading a thin layer of powder over the build area by a powder layering system called re-coater, and a high power-density laser that selectively scans over the powder layer and locally melts the powder particles in a layer-by-layer fashion [20]. The process is implemented in an inert gas chamber, usually argon or nitrogen, to remove the condensate, reduce oxidation throughout the process, and prevent the potential explosion of powders due to high localized temperature. The AM quality can be tuned by the processing parameters including laser power, scanning speed, hatching spacing, layer thickness, post exposure, pre-exposure, and many more parameters [21] which entails an optimization process depending on the target application to obtain the desired mechanical properties, surface roughness, and geometrical accuracy [22,23]. The minimum geometrical feature size formed by the LPBF process ranges between 40 and 200 μm [24]. The microstructure of metallic parts alloys produced by LPBF for materials such as Ti may consist of the columnar grains grown epitaxially from the previously solidified substrate. In some of the metal powders (*e.g.*, Ti alloys), rapid solidification due to high laser scanning speeds and small melt pool sizes may lead to a fine microstructure morphology entailing a cellular structure inside the columnar grains. High thermal cyclic gradients and fast cooling rates during the melting and solidification stages result in significant residual stresses [25]. The geometrical features of the fabricated parts consist of agglomerated powder particles partially solidified at the vicinity of the melting pool, which results in unwanted surface roughness in the order of a few particles size. It should be noted that the rough surface finish of these implants can stimulate bone growth compared to those of conventionally manufactured counterparts because of the higher available surface area and cell entrapment in the free gaps between the particles [26]. A controlled surface roughness may promote cell adhesion and osteoconductivity. Although the LPBF process offers flexibility and precision in manufacturing complex implants, some limitations necessitate more improvements in terms of low production rate (for implant mass production), difficult switching between metal powder types, and restricted

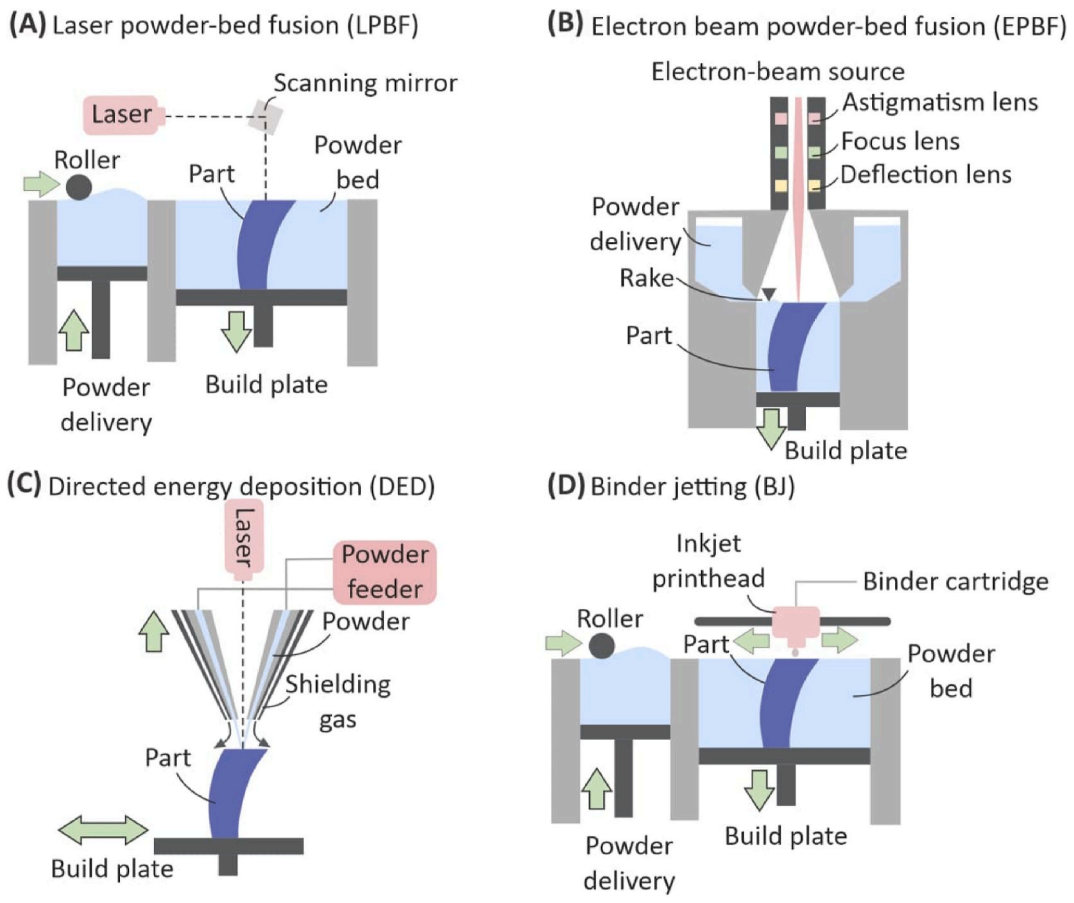

Fig. 1. The most widely used metal additive manufacturing processes for fabrication of metal implants. (A) Laser powder bed fusion (LPBF), (B) electron beam powder bed fusion (EPBF), (C) Directed energy deposition (DED) with blown powder, and (D) binder jetting (BJ) process.

specifications for selecting the metallic powder to be compatible with the AM systems [27]. These limitations hinder the manufacturing of multi-material AM parts using LPBF technique.

2.1.2. *Electron beam powder bed fusion*

The electron beam powder bed fusion (EPBF), also known as electron beam melting (EBM), operates similarly to the LPBF technology. This process employs high-energy electron beams for melting metal powder particles (see Fig. 1B). As opposed to LPBF where the 3D printing is performed under inert gas, EPBF requires a high vacuum to prevent the smoking phenomenon, contamination, and powder oxidation [28]. The vacuum condition in this process is necessary due to the oxygen sensitivity of metals [28]. In this process, a defocused electron beam is initially irradiated to raise the temperature (from ~300 to 1100 °C). This pre-heating process is required to minimize the smoking phenomenon due to the electron charge dissipation. In addition, a partial sintering of the particles during this process locally enhances powder integrity before the main electron beam scanning [22]. Various types of metallic biomaterials can be additively manufactured using the EPBF process such as 316L stainless steel, cobalt-based superalloys, nickel-based superalloys, and Ti-based alloys [29]. Preheating is also required before scanning each layer. Arcam, founded in 1997, pioneered the manufacturing of the EPBF systems [30]. The EPBF system, as shown in Fig. 1B, consists of three main parts including the electron beam unit, powder delivery mechanism, and the build chamber. In the electron beam unit, the electrons are emitted from different sources such as tungsten (W) filament, lanthanum hexaboride (LaB_6) and field-emission gun (FEG), which can be controlled *via* magnetic lenses. The metal powders are delivered through a hopper and then spread by a powder layering system over the build plate [31]. The typical range of layer thickness for this technology is between 40 μm and 200 μm, depending on the powder material [32]. Each layer of powder bed is scanned, preheated, and melted by the electron beam and the build plate is lowered to allow for spreading another powder layer. This process continues until the part is entirely 3D printed. The above-mentioned limitations for the case of LPBF (*i.e.*, difficult switching between the different powder types and limited opportunity for integrating multi-material fabrication systems) are also applied to the EPBF. Nevertheless, EPBF is still extensively used for the fabrication of medical implant prototypes from Ti alloys due to their excellent stiffness and proper metallurgical quality.

2.2. *Directed energy deposition*

Directed energy deposition (DED) with different heat sources such as laser, electron beam, plasma, and lasers, has been used for the fabrication of implants. This method is also known as laser metal deposition (LMD), or laser energy net shaping (LENS), or laser cladding (LC), and is classified as one of the laser-based AM processes [33]. In this process, the metal material is either in powder or wire form that is fed through a nozzle and melted simultaneously using a focused laser beam (see Fig. 1C) to form the melt pool. In most DED systems, the overhead nozzle moves upward in a layer-by-layer fashion, whereas in other metal AM systems the substrate is repositioned downward with a stationary nozzle [32]. Besides, the melt pool is not surrounded by the powder bed, so the process could be more cost-effective than *e.g.*, LPBF and EPBF, as a lower amount of waste material is left for recycling. The DED process utilizes a high-power laser of up to 4–10 kW. The oxygen level during the 3D printing process could be lowered (<10 ppm) inside an inert chamber to prevent oxidation of the material [34]. One of the advantages of DED

compared to LPBF is the high build rate and volumes [32]. The maximum building rate >300 cm^3/h has been reported depending on the process parameters (including scanning speed, laser power, laser beam diameter, and layer thickness). The layer thickness is normally in the range of 40 μm to 1 mm [35,36]. The amount of energy needed for melting depends on the powder material and powder feed rate. As the powder feed rate decreases, less energy is required for melting the feeding material, and thereby, a deeper melt pool is formed. The powder feed rate depends on the material type; for instance, the feed rate for the deposition of Ti–6Al–4V is in the range of 4 g/min to 30 g/min [37]. The laser beam diameter ranges from 0.3 mm to 3 mm [38] and the laser scan speed varies between 150 mm/min and 1.5 m/min. The shielding gas, which is also fed through the nozzle, provides higher control on the deposition by increasing the cooling rates [39]. The DED process can be integrated into sophisticated robotic systems to increase the motion degree of freedom. In this way, the need for support structures that are required in LPBF and EPBF is minimized. The DED process can be employed for surface repairing and modification [40]. A wide range of metallic biomaterials such as that of cobalt (Co) alloys [41], Ti alloys [42], Ta [43], and nickel titanium (NiTi) [44] has been successfully fabricated using the DED process. Other advantages of DED include easy switching between materials enabling multi-material printing, high density, improved mechanical properties as high as wrought or casting materials, high build rate, and printability of larger parts compared to PBF [45]. The use of powder with a larger particle size compared to PBF leads to lower costs. This process can also be used for coating or repairing applications. Major limitations of DED however, are residual stresses, shrinkage, and deformation because of local temperature variations, lower-dimensional resolution, and higher surface roughness compared to PBF, limited complexity of parts, and need for post-processing [45]. Nevertheless, this technique has demonstrated the capability for manufacturing porous biomedical implants and functionally graded materials [41,46]. Recent studies have demonstrated the DED fabrication of load-bearing implants. For instance, Marattukalam et al. [44] studied the effect of DED process parameters on the corrosion properties and microstructure of NiTi alloy for bone implant application.

2.3. Binder jetting

Binder jetting (BJ) is a powder-based AM process that employs a liquid binder, instead of a laser or electron beam source, for locally binding the powders and forming the complex metallic, polymeric, and ceramic structures [24]. This technology was first developed in 1993 at the Massachusetts Institute of Technology [47] and ExOne, ZCorp, and Xoxeljet have led to the manufacturing of this technology [48]. Fig. 1D demonstrates the schematic of the BJ process. In this process, a roller spreads the metal powder over the build plate and a liquid binder is selectively injected by a printhead (similar to the printhead on a paper printer). Then, the subsequent layers are added until the part is fully 3D printed. The 3D printed part, which is typically referred to as the “green part”, is removed from the build plate and then depowdered. Then, the green part is placed in a furnace to burn out the binder. At this stage, void and microporosity are formed in the structure. Since the green part is fragile, a secondary step including infiltration and/or sintering is required to strengthen the structure [49] where a powder with low-melting temperature (*e.g.,* bronze) is infiltrated into the voids using the capillary effect to decrease microporosity. Through the sintering/-heat treatment process, the “green part” is placed in a high-temperature furnace, so that not only the binder burns out, but also the metal powder is partially melted and bound together to produce the so-called “brown part” [50,51]. The sintering process aid in filling the voids by the powders that eventually enhance the final density [52].

One major advantage in this process is that support structures are not required for complex geometries. In addition, due to the low cooling rate, the residual stress is significantly decreased. As opposed to the LPBF process, BJ enables the manufacturing of high reflectivity materials [53]. Some of the other advantages of BJ include a lower cost compared to the abovementioned methods, high scalability, and a broad range of applicable materials [54–56]. However, the major limitation associated with BJ is that despite the sintering process, the final products have more voids (microporosity) compared to the *e.g.*, LPBF counterparts [57]. Moreover, the post-printing steps are necessary, which makes the total manufacturing process time-consuming and costly. Among the other disadvantages of BJ are high shrinkage, relatively low density, and low mechanical properties [54–56].

Powder-binder system compatibility is enhanced in BJ-based systems. Fabrication of the non-metallic biomaterial powders with BJ technology (such as poly (L-lactide) (PLLA) [58], calcium phosphate [59], calcium silicate [60], and hydroxyapatite (HA) [61]) has been extensively demonstrated. In this class of biomaterials, chloroform, pure water, water-polymer solutions, and acid-based binders [61] have been used as the binding agent. Metal BJ for biomedical applications, however, has been paid less attention as the current binding processes fail to form strong structures as the other technologies such as LPBF and EPBF.

2.4. Other techniques

Besides the abovementioned widely used techniques for the fabrication of metal implants, other AM methods have been evolved to enable their biomedical application. Metal sheet lamination, known as laminated object manufacturing (LOM), is a relatively inexpensive 3D printing technique for metallic and ceramic materials [62]. In this technique, instead of using metal powders or wires as a feedstock, rolled metallic sheets coated with sticky substances are utilized to fabricate 3D structures [63,64]. The first layer of metallic sheet is rolled over the building platform and a beam of laser or a razor cuts through the metal sheets according to a CAD model. Then, the building platform is lowered along the z-direction allowing the 3D printer to feed the second layer, and the process continues until the final part is formed. The thickness of the metal sheets is usually between 0.07 and 0.20 mm [65]. The metal sheets are commonly glued together; however, other techniques such as hot pressing, clamping, and ultrasound irradiation can also be used [66]. The LOM technique has a variety of benefits compared to other AM methods. The LOM process does not need supporting materials. Moreover, LOM can be easily used for 3D printing of multi-metal parts by simply alternating the sheets in each layer [67]. Although LOM offers several benefits, a large amount of waste materials, and low printing speed (especially for complex objects [63,68]) are among the limiting factors for its scalability. In addition, the likelihood of layer delamination in printed components used in a harsh environment is high.

Extrusion-based metal AM, also known as atomic diffusion AM (ADAM), is a 3D printing technique with a similar process as fused deposition modeling (FDM) wherein thermoplastic polymers are melt-extruded to build layers [69,70]. The filament in ADAM is usually a composite of metallic nanoparticles in thermoplastic polymer matrices (as binding agents), which can be extruded at high temperatures. Here, subsequent sintering processes can be implemented to sinter the metal nanoparticles [68,71]. The main advantages of the ADAM technique involve simplicity, high controllability, and the ability to fabricate metallic composite biomaterials. The ADAM process is slower than laser scanning-based AM [68]. Extrusion-based metal AM has not been widely applied to biomedical applications yet. Recently, XJet Co. introduced a novel jetting-based metal AM using a technology similar to the conventional material jetting systems. Metal nanoparticles are dispersed in an engineered liquid and loaded into a cartridge. Then, thousands of printheads jet the small droplets (pico-liter volume range) of build and support materials simultaneously. The liquid is rapidly evaporated at high temperatures, thereby metal nanoparticles are sintered into the dense parts, followed by the support removal process.

3. Metallic biomaterials for additive manufacturing

Various types of metal alloys have been integrated with AM platforms. Table 1 summarizes the most common metallic biomaterials in AM along with their applications, advantages, and limitations. The latest advances made thus far to adapt those materials with AM are also discussed in the following subsections.

3.1. Titanium alloys

Titanium (Ti) alloys are among the most biocompatible candidates for the fabrication of metal implants where high strength, lightweight, as well as corrosion resistance, are demanded [72]. A titanium oxide (TiO_2) layer is usually formed on the surface of Ti-based implants that protects the Ti alloy from the surrounding harsh chemical environment and corrosive bodily fluids (such as blood) [73]. The TiO_2 layer is also associated with improved cell proliferation. The Ti alloys, however, have poor tribological properties (*e.g.*, in comparison with Co–Cr alloys) due to their lower hardness and are not the best choice when high wear resistance is needed [34].

Conventional methods for fabrication of the Ti-based implants (*e.g.,* machining, forging, and milling) are associated with multiple challenges: (i) tool fracture and chattering is common during the manufacturing process (due to the low thermal conductivity of Ti), (ii) those methods are often costly since they are subtractive-based and lead to a significant amount of material waste. (iii) Tool trajectory generation for computer numerical control (CNC) manufacturing of implants is a costly and time-consuming process. (iv) Manufacturing processes can introduce microcracks on the metal surface which can deteroriate mechanical function of the implants. (v) It is extremely costly to fabricate patient-specific implants using conventional methods such as forging. Hence, AM of Ti-based implants is an excellent alternative manufacturing route towards the efficient fabrication of customized implants for hard tissue replacements [74]. The bulk Ti has a higher Young's modulus of 110 GPa compared to natural bone (cancellous bone ~0.5–1 GPa and cortical bone ~20 GPa). This mechanical mismatch can cause stress shielding, bone weakness, and implant loosening complications. With the aid of AM techniques, ordered porous Ti implants aim to lower stiffness closer to that of natural bone [75].

A well-known medical grade Ti alloy, *i.e.*, Ti–6Al–4V has been extensively used for biomedical applications. From a metallurgical standpoint, the microstructure of the as-built LPBF processed Ti–6Al–4V alloys is acicular martensitic or α' phase structure with high dislocation density because of the high cooling rates [76]. This microstructure type could be changed to lamellar ($\alpha + \beta$) phases after heat treatment and hot isostatic pressing (HIP) [77]. The higher strength of the LPBF manufactured Ti–6Al–4V samples in comparison with their wrought counterparts is due to the altered microstructure during the manufacturing process [78]. High thermal gradients and high cooling rates in the fusion-based metal AM process often result in a very fine microstructure and columnar grains, especially in Ti alloys [79]. These Columnar grains can lead to anisotropic mechanical properties in the additively manufactured parts [35]. Zhang et al. [80] studied the anisotropic behavior of additively manufactured Ti alloys. They fabricated two different geometries perpendicular to (horizontal) and parallel to (vertical) the build direction under two different heat treatments. All samples showed similar columnar β grains and very different α laths. Horizontal samples indicated stronger strength and inferior ductility than the vertical samples. In another study, Wu et al. [81] characterized anisotropy in terms of impact toughness for Ti alloys. The horizontal specimen was found to have ~96% higher impact energy compared to the vertical specimen. It has been reported that hardness at the X-plane (refers to the cross-section perpendicular to the direction of laser motion) was about 20% lower than Y- and Z-planes [82]. Post-annealing of the additively manufactured parts has been proposed as a solution to reduce anisotropic properties in these structures [83]. It should be noted that additively manufactured Ti–6Al–4V parts are more susceptible to thermal distortion and composition changes compared to stainless steel 316 [84]. Nevertheless, Ti–6Al–4V (as well as stainless steel 316) alloys are less vulnerable to the lack of fusion defects.

Among the safest alloying elements for biocompatible Ti alloys are Nb, Ta, and Zr, which are non-allergic and non-toxic [85]. To address the safety and manufacturing issues and to reduce the stress shielding effect, low modulus beta Ti alloys with non-allergic and non-toxic alloying elements have been produced. Zhang et al. [86] additively manufactured near full density (>99%) Ti–24Nb–4Zr–8Nb (Ti2448)

Table 1
Summary of the metallic biomaterials used for additive manufacturing of implants.

Biomaterial	Advantages	Limitations	Applications	References
Titanium (Ti) alloys	Biocompatible, high specific strength, high corrosion resistance, lightweight, less lack of fusion defects	Poor hardness and tribological properties compared to some other alloys (*e.g.*, Co–Cr), stress shielding issues (can be improved by defining porosity within implant)	Many of the metallic implants such as joints, cranial, dental implants, *etc.*	[34,72,75,85]
Tantalum (Ta) alloys	Biocompatible, high corrosion resistance, high strength and elastic modulus, bioactivity	High cost and density, Stress shielding issues (higher elastic modulus compared to Ti)	Small implant components, porous implants, coating for implants to enhance osseointegration properties	[88,89,91]
Ferrous alloys	Acceptable biocompatibility, high tensile strength and elastic modulus, low fabrication costs, availability, toughness, higher thermal conductivity and consequently finer surface finish compared to Ti alloys	Potential inflammatory responses due to long-term degradation and release of alloying elements. The release of Fe can have detrimental effects on cells	Mostly for short-term implants and screws as well as surgical tools. Applications as dental and orthopedic implants as well as surgical instruments are also reported	[93–95]
Cobalt-Chrome (Co–Cr) alloys	Biocompatible, high hardness, wear, and corrosion resistance	Most Co–Cr alloys include Ni that can cause allergic reactions	Mostly as short-term implants, dental replacements and implants which are excessively used such as hip and knee substitutes	[34,78,100,102,128]
Magnesium (Mg) alloys	Biocompatible, adjustable biodegradation, biomechanical compatibility with bone, density and elastic modulus compatible with bone, cell ingrowth acceleration and faster bone formation	Printing challenges related to high surface energy and electronegativity as well as oxidation when exposed to oxygen, mechanical properties not sufficient for load-bearing applications	Mostly used as temporary bone substitutes	[106–108,114,129,130]
Smart alloys	Biocompatible, recovering original shape upon applying external stimuli, near body transformation temperature, near bone elastic modulus	Release of Ni ions due to corrosion may cause safety issues and implants may fail in long-term, precise control over the composition and AM parameters, as well as post-processing conditions, is necessary to assure both shape memory effect and printability	Cardiovascular stents, orthodontic wires, and dental braces	[115,116,121–125]

acetabular hip cup scaffolds using LPBF with a yield strength of 563 MPa and Young's modulus of 53 GPa. The higher ductility of these alloys ensures the required toughness and prevents fracture.

3.2. Tantalum alloys

Most metallic implants such as Ti alloys are bioinert and lack sufficient osseointegration, which postpones integration with host tissue and implant fixation [87]. Tantalum (Ta) alloys are gaining attention due to their unique corrosion resistance, mechanical properties, and bioactivity to stimulate bone regeneration. An attractive feature of the Ta implants is bone-like apatite layer formation on their surface in presence of simulated body fluids that lead to strong implant-bone bonding [88]. High hardness and ductility of Ta hamper using the traditional subtractive manufacturing techniques for fabrication of the complex-shaped implants [89]. Complex Ta implants can be manufactured by AM processes while the mechanical properties and bioactivity can be tuned by mixing with other metallic powders, design optimization, and adjusting the printing parameters. Because of the promising biological properties of Ta and the efficient manufacturing of large-scale Ta implants with AM techniques, the Ta alloys have been paid increasing attention during the past decade [43]. However, due to the high cost and density, pure Ta application has been limited to small implant components. The bulk Ta has an elastic modulus in the order of Ti alloys which is significantly higher than natural bone (cancellous bone ~0.5–1 GPa and cortical bone ~20 GPa). Hence, efforts have been made to produce Ta implants with mechanical properties close to the host tissue. Balla et al. [43] used LENS technology to manufacture porous Ta implants with various porosity levels (27%–55%) and a wide range of mechanical properties, yield strength (100–746 MPa), and Young's modulus (2–20 GPa), which were close to that of human bone. In other studies [90], it was observed that Ta-coated surfaces contribute to a higher cell density and adhesion compared to Ti surfaces. Note that the porous Ta implants cannot substitute those made of Ti due to the high density, cost, and high melting point that makes Ta more challenging to process [91]. Mixing Ta alloy with Ti alloys has been undertaken as a strategy to take advantage of both material types. Sing et al. [92] manufactured Ti–50Ta structures with a high yield strength (882.77 MPa) and low modulus (75.77 GPa) using the LPBF process [92]. Since the superior biocompatibility, corrosion resistance, and improved Young's modulus, Ti–50Ta was a promising alloy for biomedical applications.

3.3. Ferrous alloys

The ferrous alloys were traditionally used as biomedical implants and stents, but the release of Fe can trigger reactions with peroxides and produce radicals. Interaction of these radicals with lipids, proteins, DNA and eventually living cells can cause detrimental effects such as heart failure, liver failure, shock, coma, and even death [93,94]. Stainless steel 316L is considered as a subclass of ferrous alloys that contains chromium (Cr) and nickel (Ni) and is one of the well-known food and drug administration (FDA) approved ferrous metals vastly used for dental and orthopedic implants as well as surgical instruments [94]. Surgical grade 316L stainless steel has been used in the total hip arthroplasty and load-bearing implants due to the corrosion resistance, excellent mechanical properties, tensile strength, and biocompatibility. Note that Ti alloys have shown similar strength while having ~50% lighter weight and higher resistance to repeated cyclic loadings. Long-term degradation of implants in the physiological environment and release of alloying elements such as Ni in stainless steel causes inflammatory responses, allergies, and consequently failure of the implant [95]. However, due to their low-cost fabrication, availability, toughness, and acceptable biocompatibility stainless steel remains a popular temporary implant option. Recent efforts to address the Ni release and improve the biocompatibility of stainless steels led to the development of Ni-free stainless steels with high nitrogen content [96,97]. Stainless steel 316L has a lower fusion point compared to the Ti–6Al–4V that can be explained by the higher thermal conductivity of 316L which leads to the finer surface finish of the additively manufactured 316L parts. Anisotropic properties are also inevitable in ferrous alloys. Jeon et al. [98] investigated the microstructural and mechanical anisotropy of 316L stainless steel fabricated *via* LPBF by performing tension and compression tests. The results revealed that there is significant anisotropy in terms of yield strength and strain hardening under compression. They demonstrated that the shape of pores and the boundary of the molten pool are the main causes of mechanical anisotropy. Yu et al. [99] compared mechanical anisotropy of additively manufactured Ti–6Al–4V alloys with 304 stainless steel. The Ti–6Al–4V samples showed a larger anisotropic behavior compared to 304 stainless steels. The yield strengths and ultimate tensile strength of the horizontally printed Ti–6Al–4V and 304 stainless steel samples were higher than those of vertically printed tensile test parts. Heat treatment as an effective method to eliminate columnar structures and thus reduce mechanical anisotropies was demonstrated. However, the ductility and microhardness of the samples were reduced after the heat treatment process. Therefore, more efforts are required to avoid anisotropic behavior in additively manufactured metal parts without compromising their mechanical properties.

3.4. Cobalt-chrome alloys

The cobalt-chrome (Co–Cr) alloys have been used for dental implants due to biocompatibility as well as superior hardness leading to promising wear and corrosion resistance [34]. Among various Co–Cr alloys, cobalt-chromium molybdenum (Co–Cr–Mo) has been widely processed by AM techniques [46]. The Co alloys have shown greater ductility and wear resistance in comparison to Ti alloys and stainless steel [100]. In the Co–Cr–Mo alloys, the Cr element protects the implant from the corrosive environment by forming a thin continuous oxide layer on the surface and Mo improves the bulk strength and corrosion resistance [101]. The Co–Cr alloys contain Ni that can cause allergic reactions as of the stainless steel [102]. This problem is addressed by introducing an ASTM F799 alloy that is a Ni-free Co–28Cr–6Mo wrought alloy [85]. It has been shown that the wear resistance of Co–Cr–Mo alloys is highly microstructure-dependent. The martensitic transformation is known to be effective in the reduction of the wear rate by introducing the hexagonal close-packed (HCP) ε in the microstructure of low carbon Co–Cr–Mo from a metastable face-centered cubic (FCC) phase [103]. Hence, Co–Cr–Mo alloys are considered to be suitable candidates for hip implants under excessive wear due to their promising wear resistance properties [78]. Comparative *in vitro* study of the LPBF processed and cast Co–Cr alloy demonstrated that LPBF processed structures show a significantly lower ion release to the surrounding fluid. Moreover, the LPBF processed structures showed higher cell proliferation than their casted counterparts indicating higher biocompatibility of parts fabricated by AM [104]. Stress shielding problems may be expected due to the much higher elastic modulus of Co–Cr alloys compared to bone. Hence, novel design strategies for developing meta-biomaterial structures with interconnected porosities should be developed for Co–Cr implants [105].

3.5. Magnesium alloys

Metal implants are non-biodegradable and remain stable *in vivo*. Magnesium (Mg) and a number of its alloys have been recently recognized as promising candidates for fabricating biodegradable metallic orthopedic scaffolds that can be completely degraded over time to be replaced with the newly formed tissue [106,107]. The biodegradation rate of the implants can be tuned by manipulating the composition of the alloys to assure gradual degradation at the same rate as bone healing. Mg alloys offer superior biomechanical compatibility with bone compared to the other metallic biomaterials. The released ions from

Mg-based implants (Mg^{2+}) can accelerate cell ingrowth and bone formation. The Mg^{2+} can act as a compelling catalyst to activate more than 300 required enzymes in the human body [108].

Comprehensive studies have been undertaken to moderate the degradation rate of Mg in three different manners and enable widespread clinical applications. For instance, Li et al. [109] added rare earth elements to Mg to fabricate LPBF processed biodegradable scaffolds with lower degradation rates. The results showed that around 20% of the volume of the scaffold was degraded after ~4 weeks. Generally, alloying Mg with different elements or incorporating it with some polymers such as polylactide-*co*-glycolide (PLGA)/tricalcium phosphate (TCP) enhances strength and lowers the degradation rate [108,110]. Xie et al. [111] suggested that alloying Mg with manganese (Mn) can decrease the biodegradation rate mostly due to the formation of a Mn oxide film on the surface (acting as a protective layer). Incorporating Mn into Mg alloys decreased the metal grain size that can be attributed to the enhanced number of nucleation sites. The LPBF processed alloy showed antibacterial properties and cytocompatibility for application as bone implants. Coatings and surface treatment are the other alternatives to control corrosion of the Mg [112]. The AM of various Mg alloys (*e.g.*, AZ91D, Mg–9%Al, ZK60, and WE43) has been demonstrated using LPBF technology [113]. However, there are several challenges associated with the 3D printing of Mg powder mostly due to its high surface energy and electronegativity as well as oxidation when exposed to oxygen. The Mg powder can also be integrated within a polymeric matrix to develop a printable paste for 3D printing *via* extrusion-based techniques [114].

3.6. Smart alloys

Smart alloys (also known as shape memory alloys) are a unique category of metals that can remember and recover their original shape upon applying external stimuli such as light, heat, magnetic field, electrical field, and exposure to chemicals [115]. Nickel-titanium (Nitinol) is the most well-known shape memory alloy for medical applications that contain nearly equal concentrations of Ni and Ti [116,117]. Nitinol alloy can recover its original shape upon heating after undergoing plastic deformation. The shape memory effect happens due to phase transition in solid-state form martensite (the low temperature phase) to austenite (the high temperature phase), and *vice versa*, known as martensitic thermoelastic transformation [118,119]. Nitinol can be processed by metal AM techniques; however, the content of Ni is of high importance for the processability of the material. This is because the temperature of martensitic thermoelastic transformation is significantly increased with a decrease in the Ni content. Increasing the Ni element above a specific point (depending on the other components) may not result in the shape memory effect. Hence, precise control over the composition and AM parameters as well as post-processing conditions is necessary. Various AM techniques including LPBF, EPBF, and LENS have been used for 3D printing of nitinol, each of which have their own challenges and limitations. Since EPBF has a higher energy density and consequently higher powder temperature, a higher temperature of martensitic thermoelastic transformation is observed. In the LENS technique, a mixture of Ni and Ti can be directly fed to the nozzle, which has been shown to form high-quality alloys at the expected phase transformation temperature [119]. Thermal post-processing is mostly utilized to decrease the temperature of martensitic thermoelastic transformation after the AM processes [119]. Further evolution in the processing of the shape memory alloys should be directed toward four-dimensional (4D) printing of the medical implants with spatial controlled thermal history [120].

Nitinol alloys have been studied for implants, cardiovascular stents [121] orthodontic wires [122,123], and dental braces [124] due to their near body transformation temperature, near bone elastic modulus, corrosion resistance, and biocompatibility [125]. Nonetheless, the release of Ni ions due to corrosion can cause safety concerns, and nitinol implant may fail in long-term implementation. However, TiO_2 coating on nitinol structures could reduce Ni ion leaching. Constant et al. [126,127] studied nitinol degradation in biological and physiological fluids and evaluated the corrosion resistance of nitinol along with surface morphology. Here, Ni and Ti release from the specimen was recorded over six months of incubation in synovial fluids.

4. Design methodologies for implant additive manufacturing

The topological design of implants has gained increasing attention as AM technologies enable the manufacturing of complex-shaped metal structures. Pore characteristics in porous scaffolds have been particularly employed to tune the mechanical and biological responses. These architectures are classified as stochastic [131] and ordered geometries. There are multiple approaches towards the design of implants at micro- and macro-scales, each of which is based on specific design algorithms. Objective functions in topology optimization techniques are defined to attain final design through iterative design processes. In addition, patterned periodic porous structures are designed based on a large library of unit cell types. These pore shapes have been well-established and studied in the literature based on lattice networks and mathematically defined surfaces (*i.e.*, triply periodic minimal surface (TPMS)-based architectures). Advanced design procedures develop functionally porous gradient structures where pore characteristics spatially vary to obtain multiple target functionalities in the scaffold design. In the following sections, the above-mentioned categories of design methodologies are discussed in detail.

4.1. Topology optimization of implants

Topology optimization aims at obtaining the optimal structural layout of a design for a set of objectives under certain constraints [132]. Optimization processes continuously take place in the natural organs of the body. Bone remodeling is the core aspect of bone tissue engineering, adapting the bone's internal structure to the external loading conditions. This process entails reorienting the principal stress paths to maximize mechanical efficiency leading to an optimal structure [133]. Another emerging utility of the topology optimization techniques is to mitigate the anisotropic behavior of the porous structures. Using the curvature wall thickness adjustment algorithms, in combination with finite element methods, anisotropic architectures could be reshaped to their isotropic equivalents [134,135].

Most topology optimization algorithms are based on a pseudo-density design variable (considering the mechanical modulus of the material); hence, they can be readily tailored for bone scaffold and implant design. The resulting topologies often consists of intricate features, which are difficult or impossible for production by conventional manufacturing processes. Fortunately, AM processes are capable of producing parts with complex features as long as certain manufacturing constraints are adhered to. Therefore, there exists a synergistic partnership between topology optimization and AM that enables flexible design solutions.

Over the years, several efforts show that most designs using topology optimization for AM have focused on implants for the head and pelvic regions, as summarized in Table 2. There are a variety of topology optimization methods or approaches, such as the bi-evolutionary structural optimization (BESO), solid isotropic material with penalization (SIMP), and the level set methods (LSM) [136]. Among those methods, SIMP is by far the most used in the literature due to its robustness, decent range of application to several physics, and relative simplicity in implementation. It is also observed that most efforts employed the polymer-based materials extrusion AM technology, *e.g.*, FDM, mostly for prototyping and visualization.

A common adverse phenomenon in bone-implant interaction is stress shielding where a much stiffer implant compared to surrounding bone regions causes inaccurate or inefficient bone remodeling [137]. Topology optimization is an excellent mathematical tool to achieve such

Table 2
Design of medical implants and devices using topology optimization tailored for additive manufacturing.

Implant type	Topology optimization approach	Implant material	AM technology	Reference
Subperiosteal implant	SIMP	Ti–6Al–4V	Metal AM (no specific process mentioned)	[138]
Generic implant-to-trabecular model	SIMP	Ti–6Al–4V and porous tantalum (Ta)	SLS	[139]
Lumbar fusion cage	SIMP (global and local topology optimization)	Ti–6Al–4V	Direct metal laser sintering (DMLS)	[140]
Osteosynthesis plates	Not mentioned	Ti–6Al–4V	EPBF	[141]
Bone plates	SIMP	Ti–6Al–4V	EPBF	[142]
Trabecular bone	SIMP	Not mentioned	SLS	[143]
Hip prosthesis	SIMP with lattice structure design	Implant head: Cobalt-chromium alloy Implant stem: Ti–6Al–4V	LPBF	[144]
Mandibular implant and bond analog	SIMP	Ti–6Al–4V	LPBF	[145, 146]
Pelvic prosthesis	SIMP	Ti–6Al–4V	EPBF	[9]

implant solutions because popular approaches are based on minimizing compliance (maximizing stiffness) while significantly reducing material volume.

Most of computational platforms developed in the literature define their objective functions based on mechanical responses. In the following sections, the main topology optimization approaches demonstrated for biomedical applications are introduced, and their principles are discussed in detail.

4.1.1. Solid isotropic material with penalization

As mentioned above, the solid isotropic material with penalization (SIMP) method is the most widely used approach for topology optimization in biomedical applications. The SIMP approach is a gradient-based approach that utilizes a power-law relationship to establish the material properties as functions of a pseudo-density design variable. The design domain is discretized to finite elements with a pseudo-density design variable assigned to every element. The collective pseudo-density variables become the design variables. In essence, the number of finite elements in the discretized model defines the number of design variables. Most algorithms are based on minimizing the compliance (maximizing the stiffness) of the structure while placing a constraint on the material volume. Mathematically, the problem can be expressed according to the following definitions:

Objective function (Equation (1)):

$$\text{minimize } C = F^T U = U^T K U = \sum_{e=1}^{n} E_e(\rho_e) u^T k_0 u \tag{1}$$

Finite element or structural analysis (Equation (2)):

$$K(\rho)U(\rho) = F \tag{2}$$

Volume constraint (Equation (3)):

$$\frac{\sum_{e=1}^{n} V(\rho_e)}{fV_0} \leq 1 \tag{3}$$

Pseudo-density variable constraint (Equation (4)):

$$0 \leq \rho_e \leq 1 \tag{4}$$

where C, F, U, E, K, V, f, and, ρ are the compliance, force, displacement response, Young's modulus, stiffness, volume, volume fraction, and pseudo-density design variables of the design problem, respectively. Here, V_0 is the original/initial material volume, k_0 is the stiffness of a finite element assuming a uniform and homogenous mesh strategy is utilized, u is the elemental displacement, subscript e identifies an elemental parameter while n signifies the number of elements in the discretized domain.

The Young's Modulus of every element is given by a power-law expression in Equation (5):

$$E_e(\rho_e) = E_{min} + \rho_e^p (E_0 - E_{min}) \tag{5}$$

where E_0, E_{min}, and p are Young's modulus values of the solid material and "void" material, and the SIMP penalty value, respectively. E_{min} is adopted to avoid singularities in the displacement response computation. The sensitivity of the objective as well as constraint functions must be obtained in order to solve the optimization problem. The sensitivity functions are simply the first-order derivatives given in Equations (6) and (7):

Compliance derivative (Equation (6)):

$$\frac{dC}{d\rho} = -U^T(\rho)\frac{dK}{d\rho}U(\rho) \tag{6}$$

Volume derivative for a mesh with constant elements' volumes throughout the optimization (Equation (7)):

$$\frac{dV(\rho)}{d\rho} = V \tag{7}$$

These derivatives are obtained either by direct method [147] or adjoint method [148] and are used by an optimizer to update the pseudo-density design variables. After they are updated, the change in their values between the current iteration and the previous one is compared with a convergence value, and if the criterion is met, the post-processing is initiated. Otherwise, the displacement response is computed again usually by the finite element method. Since the basic framework of topology optimization has been established, several methodologies that have been implemented to topologically optimize implant designs are introduced below.

4.1.2. Weighted multi-objective topology optimization

Many implants are subjected to a variety of mechanical loads under a biological-mechanical environment as a result of the several daily activities carried out by the associated physiological region [9]. Each load is taken as a load case that results in unique strain energy or compliance function. Therefore, there are as many strain energy functions as there are loads in this algorithm. To optimize these implants for the loads, a weighted multi-objective topology optimization enables assigning different weights to the strain energy functions with a greater weight given to a load associated with higher functionality. The compliance function in (1) can be rewritten as a consolidated function [9,149–151] (Equation (8)):

$$\text{minimize } \left(C = \sum_{i}^{n} w_i C_i = \sum_{i}^{n} w_i F_i^T U_i \right) \quad i = 1, 2, 3, \ldots, n \tag{8}$$

w_i is the weight factor for every load i. The sensitivity function can be written as Equation (9):

$$\frac{dC}{d\rho} = -\sum_{i}^{n} w_i U_i^T(\rho)\frac{dK}{d\rho}U_i(\rho) \tag{9}$$

A multi-objective topology optimized pelvic prosthesis is shown in Fig. 2A for four different resection types. The Figure shows the extracted

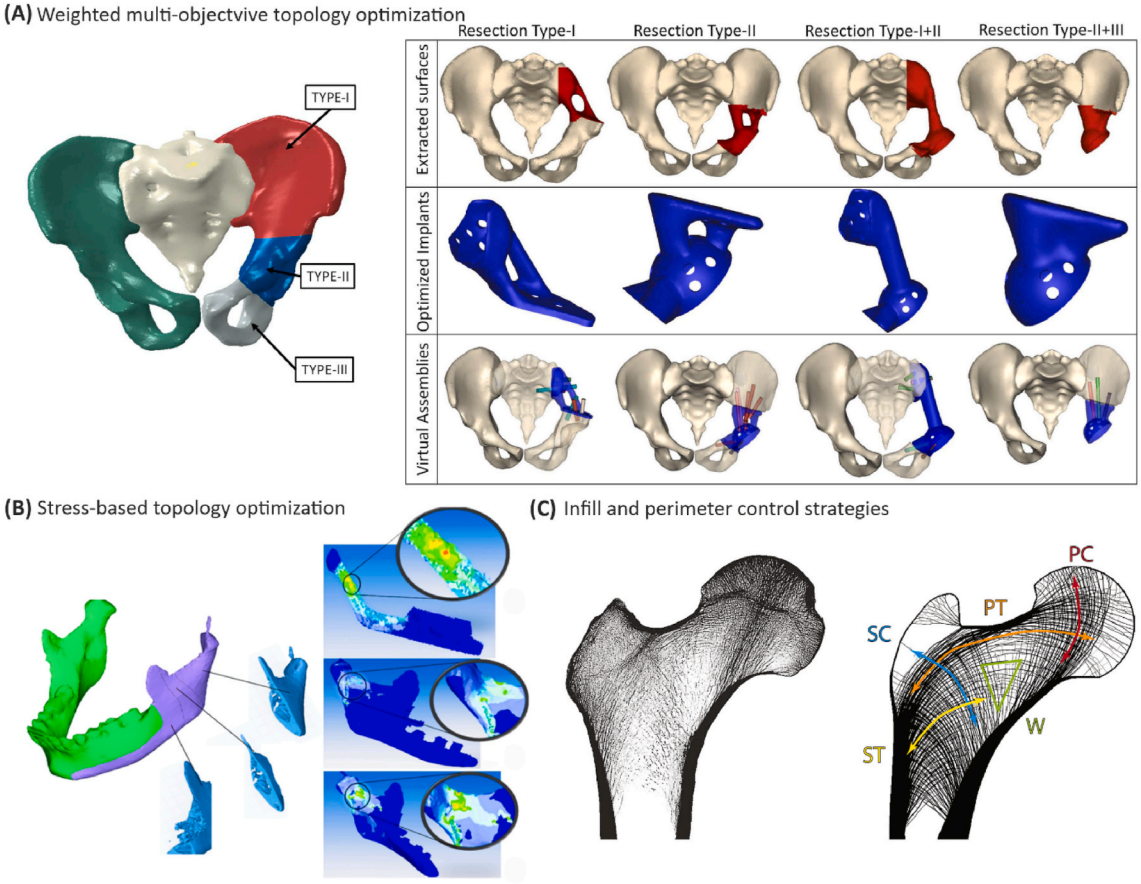

Fig. 2. Topology optimization approaches utilized for design of bone replacements. (A) Topology optimized pelvic prosthesis for four resection types. Reproduced with permission from Ref. [9]. Copyright 2019, Elsevier. (B) Stress-based topology optimized temporomandibular prosthesis showing different sections of the design. Reproduced with permission from Ref. [152]. Copyright 2017, Scientific Research Publishing (C) Venous-like topologies after applying perimeter control constraint. Reproduced with permission from Ref. [137]. Copyright 2018, Elsevier.

surfaces, optimized implants, and virtual assemblies of all optimized prostheses.

4.1.3. Stress-based topology optimization

In some instances, the optimization is done by minimizing the implant's worst-case state which is failure [152]. Besides, because stress singularity is a possibility when optimal topologies are derived using a different objective function, a stress-based approach can be attractive. Considering the theories of elastic failure, several researchers have attempted to use the maximum distortion energy theory (von Mises) to describe the failure criterion (Equation (10)):

$$\sigma_{vm} = \frac{1}{2}\sqrt{\left(\sigma_x - \sigma_y\right)^2 + \left(\sigma_y - \sigma_z\right)^2 + \left(\sigma_x - \sigma_z\right)^2 + 6\left(\tau_{xy}^2 + \tau_{yz}^2 + \tau_{xz}^2\right)} \tag{10}$$

Obtaining the derivative of Equation (10) with respect to the pseudo-density variable is non-trivial. Additionally, it is very computationally expensive to compute the stress derivative and/or constraint on every element for practical or industrial type designs [30]; therefore, the problem minimization is done on an aggregated maximum stress variable derived by a *p-norm* function as expressed in Equation (11) [152]:

$$\sigma_{vm}^{p-norm} = \left(\sum_{i=1}^{N}\left(\frac{\sigma_{vm}}{\sigma_{\max}}\right)^q\right)^{\frac{1}{q}} \quad i = 1, 2, 3\ldots\ldots, N \tag{11}$$

The objective function and pseudo-density design variable definition of the stress minimization topology optimization problem can then be formulated as Equations (12) and (13):

$$\text{minimize} \sigma_{vm}^{p-norm} \tag{12}$$

$$\text{s.t.} \quad 0 < \rho < 1 \tag{13}$$

σ_{vm}^{p-norm} is the p-norm function of the aggregated maximum stress in the discretized domain, $\sigma_{\max}$ is the maximum allowable stress and q is the *p-norm* power where a higher power results in a more accurate maximum value but at a significant computational cost. The sensitivity function is given in Refs. [152,153]. A temporomandibular prosthesis designed by a stress-based topology optimization model is shown in Fig. 2B.

4.1.4. Infill and perimeter control strategies

In a bid to model the venous and porous nature of bone structures, a topology optimization algorithm can be modified by either reformulating the problem statement and/or introducing some constraints. Wu et al. [143] introduced a per-voxel local volume constraint (infill constraint) given in Equations (14) and (15):

$$\underbrace{\text{maximize}}_{\forall e}\left(\overline{\rho}_e\right) \approx \overline{\rho}_e = \left(\sum_e \overline{\rho}_e^q\right)^{\frac{1}{q}} \tag{14}$$

where

$$\left(\sum_e \overline{\rho}_e^q\right)^{\frac{1}{q}} \leq \left(\sum_e \alpha^q\right)^{\frac{1}{q}} \tag{15}$$

here, Equation (12) can be rearranged into

$$\left(\frac{1}{n}\sum_{e}\bar{\rho}_{e}^{q}\right)^{\frac{1}{q}} \leq \alpha \tag{16}$$

In Equation (13), $\bar{\rho}_e$ is the percentage of solid voxels over a given region, while α is the local volume constraint in that region. As mentioned in the previous section, the constraint is a *p-norm* function that aggregates the maximum local density over the discretized design domain. This function replaces the volume constraint in the conventional problem statement and ensures that the local volume in a specified region is no more than the prescribed local volume, α. In turn, it generates vein-like features throughout the optimized topology. In a similar approach, Park et al. [137] introduced a 'perimeter control' constraint such that a lower bound is placed on the perimeter of every feature. The perimeter function $P(\rho)$, is given in Equation (17):

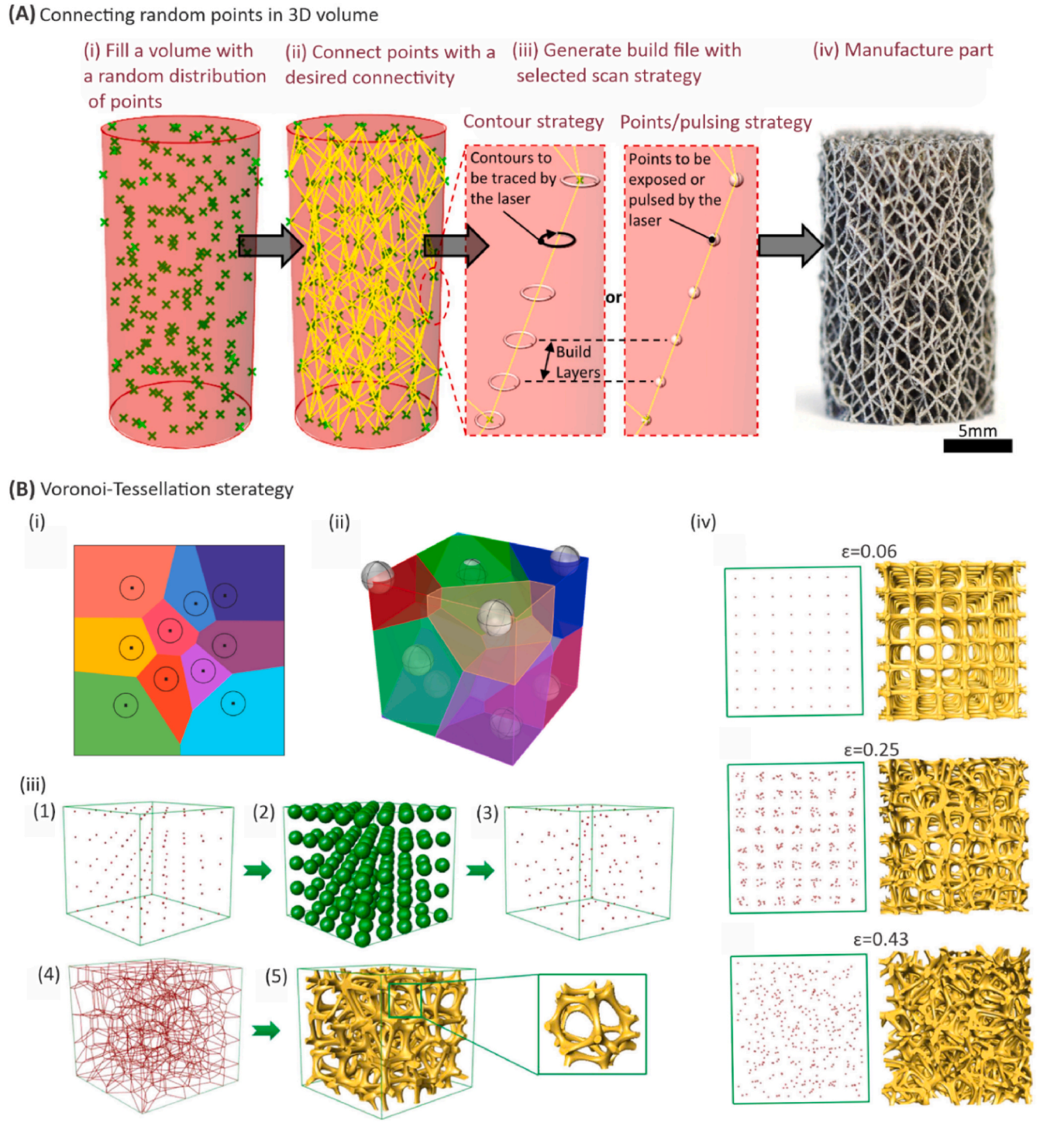

Fig. 3. Design strategies for the scaffolds with stochastic structures. (A) Porosity design based on connecting random points in the design volume. Reproduced with permission from Ref. [165]. Copyright 2018, Elsevier. (B) Voronoi-tessellation diagrams in (i) two-dimension (2D) and (ii) three-dimension (3D). Reproduced with permission from Ref. [167]. Copyright 2021, Elsevier. (iii) Design steps based on 3D Voronoi-Tessellation and (iv) controlling irregularity of the random geometries. Reproduced with permission from Ref. [172]. Copyright 2018, American Chemical Society.

$$P(\rho) = \int_{\Omega} |\nabla \rho| d\Omega \tag{17}$$

the lower bound on the perimeter is expressed as Equation (18):

$$P \geq P_{\min} \tag{18}$$

where $P_{\min}$ is the minimum perimeter value allowed in the final topology. Similar to the local volume constraint, the perimeter control function is added as a constraint, and the derivative is obtained for the optimizer. The resulting topologies after applying local volume constraint and perimeter control constraint are shown in Fig. 2C.

In many efforts, the use of the conventional topology optimization approaches either by the SIMP method [142,154–156] or other methods [133,157] have been demonstrated. It is important that the adopted method incorporates the biomechanical considerations of the implant-bone interaction to uphold the relevance of the optimal topology obtained.

4.2. Scaffold internal pore architecture design

Porous structures can be classified based on their pore interconnectivity (as open and closed pores) as well as the regularity of their pore topology and size (as stochastic and non-stochastic) [158–160]. Ordered pore shapes satisfy the interconnectivity required for cell ingrowth facilitating integration with the host tissue. The porous structures with non-stochastic design involve lattice and TPMS based unit cells [161–164]. To satisfy mechanobiological conformation and reliable integration of the porous implant with host bone tissue, optimization of physical characteristics such as pore shape, pore size, porosity, pore interconnectivity, and micro-topological surface features are required [11]. In the sections below, different types of pore shapes and the relevant tools employed to meet the design requirements for those topologies in metal scaffolds are discussed.

4.2.1. Stochastic topologies

A stochastic porous structure (known as foam), involves the pores with random shape and size distribution such as those formed using conventional techniques (*e.g.*, salt-leaching and gas-foaming) [160]. Despite their random pore distribution, manufacturing parameters could be used to control the pore shape and pore size. Stochastic structures have also been designed for AM *via* computer modeling and mathematical algorithms. Networked stochastic constructs are defined by a framework consisting of a random joint distribution in a volume. The points are then connected to obtain a connective network and scanned either based on point/pulsing or contour strategy (Fig. 3A) [165]. Voronoi tessellation diagrams as shown in Fig. 3Bi, ii [166,167] is another tool for generating stochastic material structures. In this method, a set of points (known as seeds) are randomly distributed in the design volume. The space is then partitioned into discrete regions called Voronoi cells [168,169]. Subsequently, a thickness is specified for the edges to form a 3D model [170,171]. The design process for the 3D Voronoi diagram is represented in Fig. 3 Biii. Here, the irregularity of the random geometries can be controlled by a tuning factor ε in the range of 0–1 (Fig. 3Biv) [172].

Note that the native bone microstructure comprises of struts with various thicknesses and nonuniform pore diameters. To better mimic the natural structure of bone, many studies have focused on designing functionally graded heterogeneous stochastic implants by spatially changing unit cell size, strut thickness, and porosity [167,172,173]. To design stochastic models with controlled properties, a new Voronoi method is introduced based on a top-down design approach and probability spheres. In the proposed models the porosity of the stochastic structure could gradually change laterally, which was illustrated by the graded distribution of pore spheres [168,172,174]. Gradient mechanical properties can also be achieved by varying the laser parameters during the AM process resulting in struts with various thicknesses distribution [175]. Bone-like stochastic structures can also be inspired by the native bone tissue. In a study, the 3D STL model of the implants was reconstructed from the computed tomography (CT) scanning data of the stochastic bone tissue and imported to a 3D printing system for prototyping [176]. Finding the optimal distribution of the seeding points based on the CT data from bone tissue is the main objective of this class of research.

4.2.2. Lattice networks

Lattice structures are defined as complex architectures containing an array of interconnected struts or plates that are repeatedly aligned in the 3D space [177,178]. Incorporation of lattice structures within the metal implant structures has enabled constructs with mechanical properties close to surrounding bone tissue. Besides, lattice structures pose an interconnected pore architecture allowing for cell ingrowth and better tissue integration. Examples of well-known lattice topologies include cubic, octahedron, and truncated as demonstrated in Fig. 4A. Lattice structures with simple geometries have been manufactured using traditional fabrication techniques such as water jet cutting, casting, electroless plating, and electrodeposition [179]. Though, these techniques are very time-consuming, costly, and unable to fabricate high-resolution complex structures. Whereas, using metal AM techniques, one can fabricate thin struts and lattice geometries in high resolutions and complex shapes with a lower cost and time [158]. Although there are some limitations in metal AM of very small features (*e.g.,* less than 100–150 μm in case of LPBF), the deviation of the manufactured structures from the CAD models are usually low enough to be ignored or compensated with post-processing and usually the experimental data can be reliably validated by simulation [11,180]. Lattice structures can be modeled by various CAD software such as Solidworks, Meshmixer, MATLAB, *etc*., to generate STL files for AM [181,182]. Modeling of lattice networks allows the design of scaffolds across the full range of relative density (zero to 100%) without losing interconnectivity. However, poor flexibility in designing highly merged lattice structures with a large number of patterned unit cells is computationally expensive. Likewise, the lack of compatible finite element software for analysis of models with large unit cell repeats (especially for element/mesh generation), as well as limitations in developing optimized topologies is a major challenge in the design and analysis of lattice-based AM implants.

The physical properties of lattice-based structures strongly depend on the design of pore characteristics (*i.e.*, pore size, pore shape, and relative density) as can be seen in the example of Fig. 4B [183]. Several studies have been conducted to illustrate the effect of geometrical parameters on the mechanical properties and permeability of lattice structures. In terms of porosity, it is evident that the permeability is enhanced with porosity, whereas compressive strength and elastic modulus are inversely proportional to porosity [184]. Optimization approaches and design maps are required to address such conflicting design requirements. The mechanical properties of lattice struts are correlated to their mechanism of failure. For instance, cube and truncated cube unit cell types are classified as stretching-dominated structures where compressive failure is dominated by a layer-by-layer collapse mechanism. In these structures, the internal linkages are oriented along with the loading direction. On the contrary, unit cell types such as diamond consist of diagonal struts angled relative to the loading direction. These structures are referred to as bending-dominated architectures wherein the compressive failure is typically originated from progressive shear bands across the porous structure (Fig. 4Ci,ii). In general, bending-dominated pore shapes are characterized with lower elastic modulus and compressive strength compared to that of stretching-dominated structures (Fig. 4 Ciii) [185]. This behavior is attributed to the generally larger strength of metals under axial versus shear deformations. The larger strength of cubic pore share relative to the diamond was also confirmed both experimentally and numerically using finite element simulations on Ti-based scaffolds [186]. The fluid

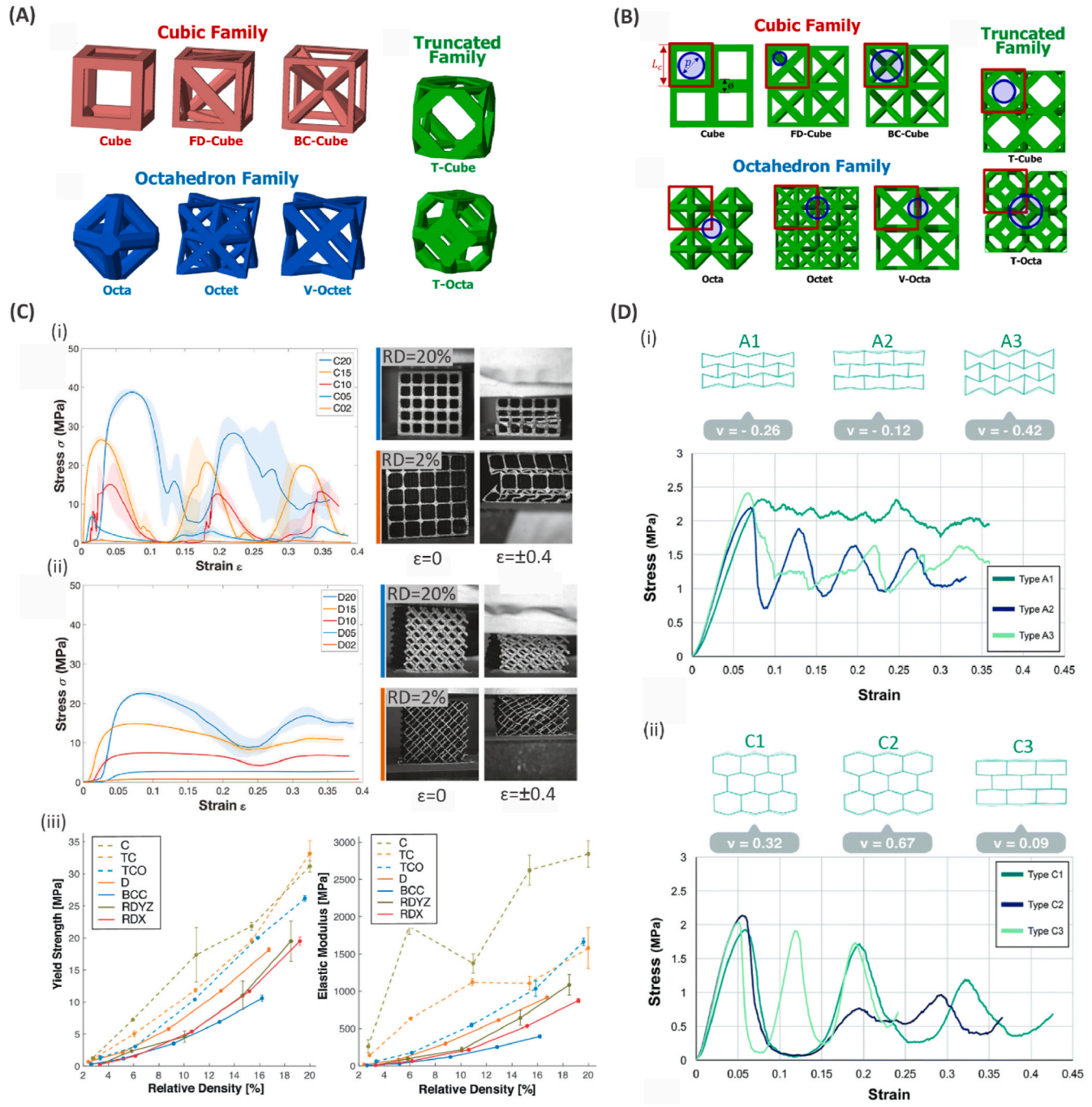

Fig. 4. Examples and mechanical properties of additively manufactured metal lattice structures. (A) Schematic illustration of famous lattice network topologies. (B) Unit cells are marked with red rectangle and pore sizes are represented with blue circles in each lattice design. Reproduced with permission from Ref. [188]. Copyright 2017, Public Library of Science. (C) Stress-strain curves of (i) cube and (ii) diamond lattice. (iii) Yield strength and elastic modulus change with relative density for various conventional lattice structures. Reproduced with permission from Ref. [185]. Copyright 2021, Elsevier. (D) The stress-strain curves of (i) auxetic and (ii) conventional lattices. Reproduced with permission from Ref. [187]. Copyright 2018, Royal Society of Chemistry.

permeability of lattice networks (a representative of cell ingrowth capability of the scaffold) has been extensively characterized in the literature. It was shown that the permeability of the porous structures with lower relative densities was more sensitive to the pore shape [11].

Note that conventional bulk materials as well as most lattice structures, are typically characterized with a positive Poisson's ratio. A recent trend in the literature emphasizes the auxetic metamaterials (negative Poisson's ratio), where the structure transversely shrinks when subjected to compressive loads. Auxetic porous structures have provided many opportunities for the design of porous implant structures. In a study by Kolken et al. [187], they demonstrated that at the same relative density, auxetic structures fabricated using LPBF, show higher pre-fracture stress and higher ultimate compressive strength compared to that of conventional structures (Fig. 4D).

4.2.3. *Triply periodic minimal surfaces*

Triply periodic minimal surfaces (TPMS) are smooth infinite tortuous surfaces with zero mean curvature dividing the 3D space into two co-continuous phases [189]. Similar to lattice architectures, TPMS-based designs allow for tuning the mechanical properties to match the

implant with the host tissue, and also tissue ingrowth for better integrity and durability. Various pore shapes, porosity, and unit cell sizes can be mathematically defined and applied to each unit cell, which can be patterned along the global axes [190]. The TPMS geometries can be defined by the generalized Equation (19):

$$\Gamma(\mathbf{r}) = \sum_{l=1}^{L} \sum_{m=1}^{M} \mu_{lm} \cos\left(2\pi\kappa_l \left(\mathbf{P}_m^T.\mathbf{r}\right)\right) = C \tag{19}$$

where $\mathbf{P}_m = [a_m, b_m, c_m]^T$ shows the basis vector in 3D space, $\mathbf{r} = [x, y, z]^T$ indicates the location vector, κ_l and μ_{lm} represent the scale parameter and periodic moment, respectively. The left side of Equation (1) dictates the topology of the unit cells. The constant C (offset value) in the right-side of the equation controls the relative density (in the case of solid network TPMS structures) [191]. To design scaffolds, $\varphi < C$ or $\varphi > C$ defines the solid phase for solid network TPMS types. One major limitation in solid network TPMS structures involves the lack of interconnectivity at the extreme design relative densities as the TPMS structures lose their continuousness at those ranges of offset values (C) [192,193]. The surface discontinuation threshold depends on the TPMS pore shape. Sheet networks however can be defined either by thickening the TPMS surfaces or defining $-C < \varphi < C$ as the solid phase (Fig. 5A) [194] and the full range of relative density is accessible in design *via* the thickening parameters. Based on the above general equation, the equations corresponding to P-, D-, and G-surface topologies can be obtained as $\Gamma_P(r) = \cos x + \cos y + \cos z = C$ and $\Gamma_D(r) = \cos x \cos y \cos z - \sin x \sin y \sin z = C$, and $\Gamma_G(r) = \sin x \cos y + \sin y \cos z + \sin z \cos x$, respectively (Fig. 5Bi). The typical commercial modeling software such as SolidWorks, and CATIA lack specific modules for modeling mathematically defined patterned surfaces. Modeling massive TPMS structures containing a high number of unit cells is also computationally expensive. Hence, the CAD design of TPMS scaffolds has entailed auxiliary computer programs that work based on point clouds, and image processing approaches [195].

Similar to lattice networks, not only pore shape, but also relative density and specific surface area can be engineered to tune the mechanical properties in TPMS designs, as represented in Fig. 5 Bii, iii [196]. As discussed for lattice networks, TPMS solid networks also can be classified as stretching-dominated (such as P-surface) and bending-dominated (such as G-surface and D-surface). Accordingly, the failure mechanism of the TPMS structures can be characterized by either 45° shear band formation (mostly in bending dominated structures) or layer-by-layer collapse (mostly in stretching dominated structures) [197,198] as shown in Fig. 5Ci. Typical compressive stress-strain curves for these structures follow that of typical porous materials where it begins with an elastic linear region followed by fluctuations corresponding to the progressive failure of the internal layers (Fig. 5 Cii).

The cubical strut-based lattices with straight struts and sharp turns and corners (without uniform transition surfaces) show poor manufacturability in the AM processes (especially for the horizontal struts in large unit cell sizes and low volume fractions). These features can also result in thermal deformation in long overhanging features. TPMS structures enhanced additive manufacturability due to their smooth surfaces and uniform curvatures that can allow their self-supporting manufacturing [199]. Besides, cubical strut-based lattices with sharp corners show higher stress concentration compared to TPMS scaffolds with smooth curvy surfaces [200,201]. The superior mechanical and biological properties of the TPMS structures compared to that of lattice structures have been reported in the literature [202–205]. In a study by Davar Ali et al. [206], TPMS-based scaffolds showed higher permeability compared to lattice structures and the maximum wall shear stress (WSS) was attributed to the lattice structures. Besides, the *in vitro* studies confirmed that the open, interconnected TPMS structures show improved cell ingrowth compared to the scaffolds fabricated by traditional salt leaching (stochastic design) [196,207].

4.3. Functionally gradient scaffolds

The distribution of pore characteristics in AM-processed porous structures can be either uniform or non-uniform based on the target function. Uniform scaffolds include unit cells with the specific shape and porosity periodically patterned in 3D space, while non-uniform (gradient) scaffolds involve unit cell arrays where pore characteristics spatially vary across the design space to achieve one or more function(s) in a scaffold [158]. Defining gradient models is particularly simple for TPMS-based scaffolds by defining the constants of TPMS equations (such as offset value C for porosity gradients) as a function of space vectors (Equation (19)) [209]. Gradient implants have been recently utilized to address multiple conflicting design requirements [208]. In the following sections, major trends and opportunities enabled by the advanced gradient scaffolds are thoroughly reviewed.

4.3.1. Porosity and cell size gradients

Among the design parameters, the porosity of the scaffold is considered as a key parameter to locally control mechanical properties and permeability [11]. Porosity gradients are a main feature of the natural bone internal structure. Interestingly, the local pore characteristics vary dynamically to keep its structure the most robust and mechanically optimal according to the person's specific patterns of daily activities. Hence, one approach for the design of optimal scaffolds is based on the learned lessons from bone porosity distribution itself. For this purpose, the relative density of the bone at different sections is studied using CT imaging, and their local stiffness is determined based on the density-stiffness relationships. The thickness of the struts at the corresponding sections of the scaffold can be designed accordingly as shown in Fig. 6A. A similar method can be used to fabricate the graded scaffolds by Voronoi-Tessellation *via* changing the size of the probability spheres to mimic the host tissue (Fig. 6B). Han et al. [210] showed that pore size and porosity can be engineered in gradient TPMS-based scaffolds to mimic the internal architecture of the natural bone tissues for an improved bone tissue growth.

With the aid of gradient design, the conflicting requirements can be met *via* combining functions of different pore characteristics in one scaffold structure. For instance, it is evident that high relative density is required for high strength; however, bone ingrowth and scaffold integration is favored at the low relative density. It has been reported that high porosity (or high permeability) promotes bone formation, whereas cartilage formation occurs at a lower porosity [211]. One potential solution to achieve both mechanical function and high peripheral permeability is based on radial gradient patterns where a low relative density at the implant/tissue interface gradually increases towards the center of the scaffold to reinforce the structure along the axis of loading. The computational and experimental studies on the cylindrical scaffolds [11,212] suggest that radially graded porous TPMS scaffolds show enhanced fluid biopermeability compared to uniform porosity counterparts. Al-Saedi et al. [213] illustrated that the relative plateau strength in graded aluminum-based lattice structures is ~two times larger than that of uniform-based structures. Besides, the graded lattice structures showed a lower relative Young's modulus that mimics better with the native bone tissue [213,214].

Apart from relative density, the unit cell size has been designed to gradually change to mimic natural bone structure (Fig. 6C). Liu et al. [215] used LPBF technology to fabricate graded G and D porous scaffolds using Ti–6Al–4V powder. According to the micro-CT and scanning electron microscopy (SEM) technology, they indicated that gradient structures were accurately formed with an acceptable manufacturing fidelity. Vijayavenkataraman et al. [196] fabricated functionally graded sheet-based G-surface scaffolds with various thicknesses to mimic the stiffness demanded by different tissue types (Fig. 6D). Li et al. [216] showed that bone regeneration in P-surface topologies with graded porosity was about three times higher compared to those of non-porous scaffolds. This was further confirmed by higher push-out forces observed

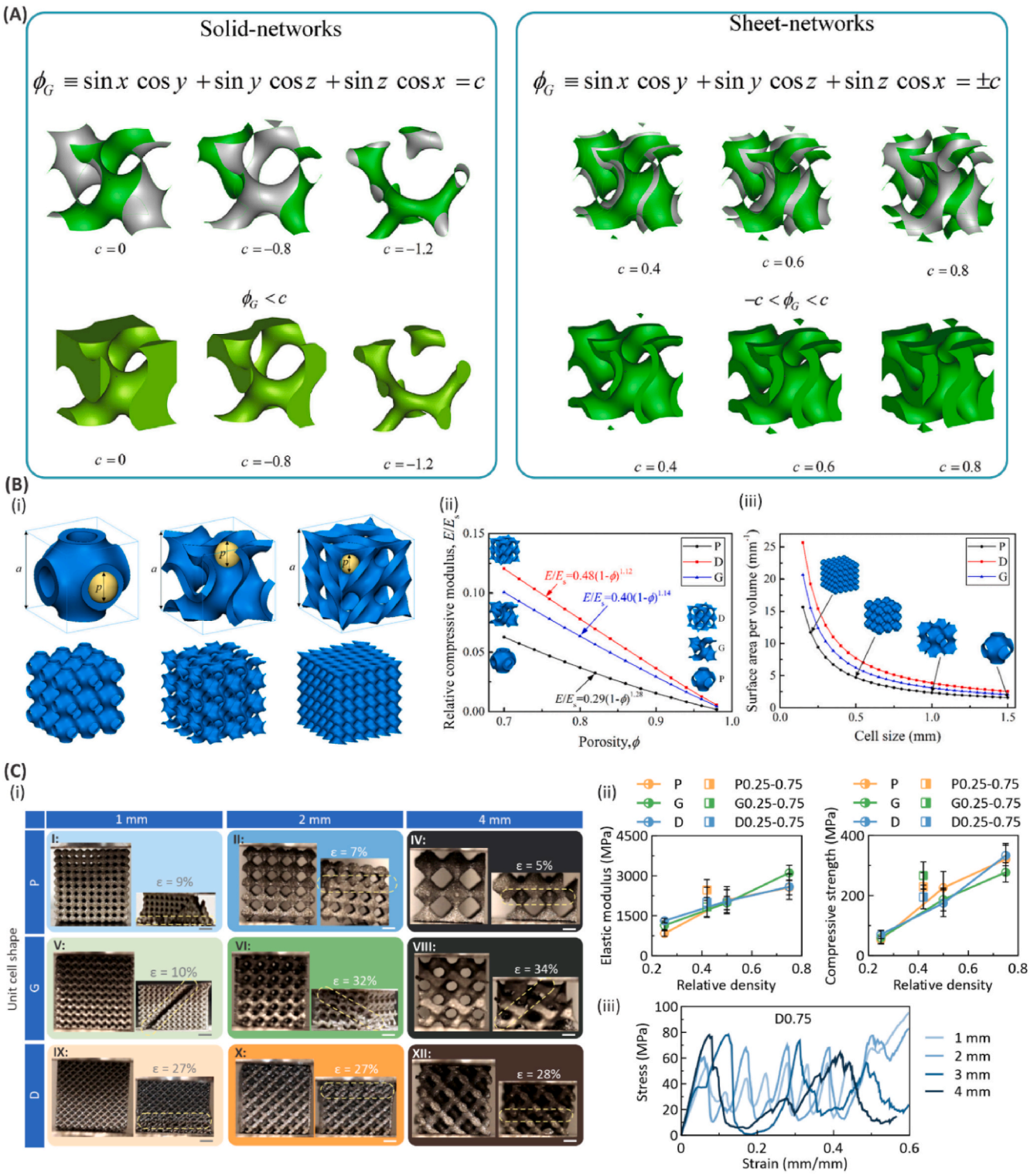

Fig. 5. Mechanical characterization of triply periodic minimal surface (TPMS)-based scaffolds manufactured by metal additive manufacturing (AM) techniques. (A) Solid and sheet-based gyroid topologies with various relative densities. Reproduced with permission from Ref. [194]. Copyright 2020, Elsevier. (B) (i) Schwarz P (P), gyroid (G), and diamond (D) unit cell geometries. Pore sizes are demonstrated in yellow. (ii) Relative compressive modulus changes with porosity and (iii) Surface area changes with unit cell size. Reproduced with permission from Ref. [196]. Copyright 2018, American Chemical Society. (C) (i) Failure mechanism of P, G, and D scaffolds. (ii) Elastic modulus and compressive strength change with relative density. (iii) Stress-strain curves of the D-surface scaffolds with various unit cell sizes. Reproduced with permission from Ref. [208], Copyright 2021, American Chemical Society.

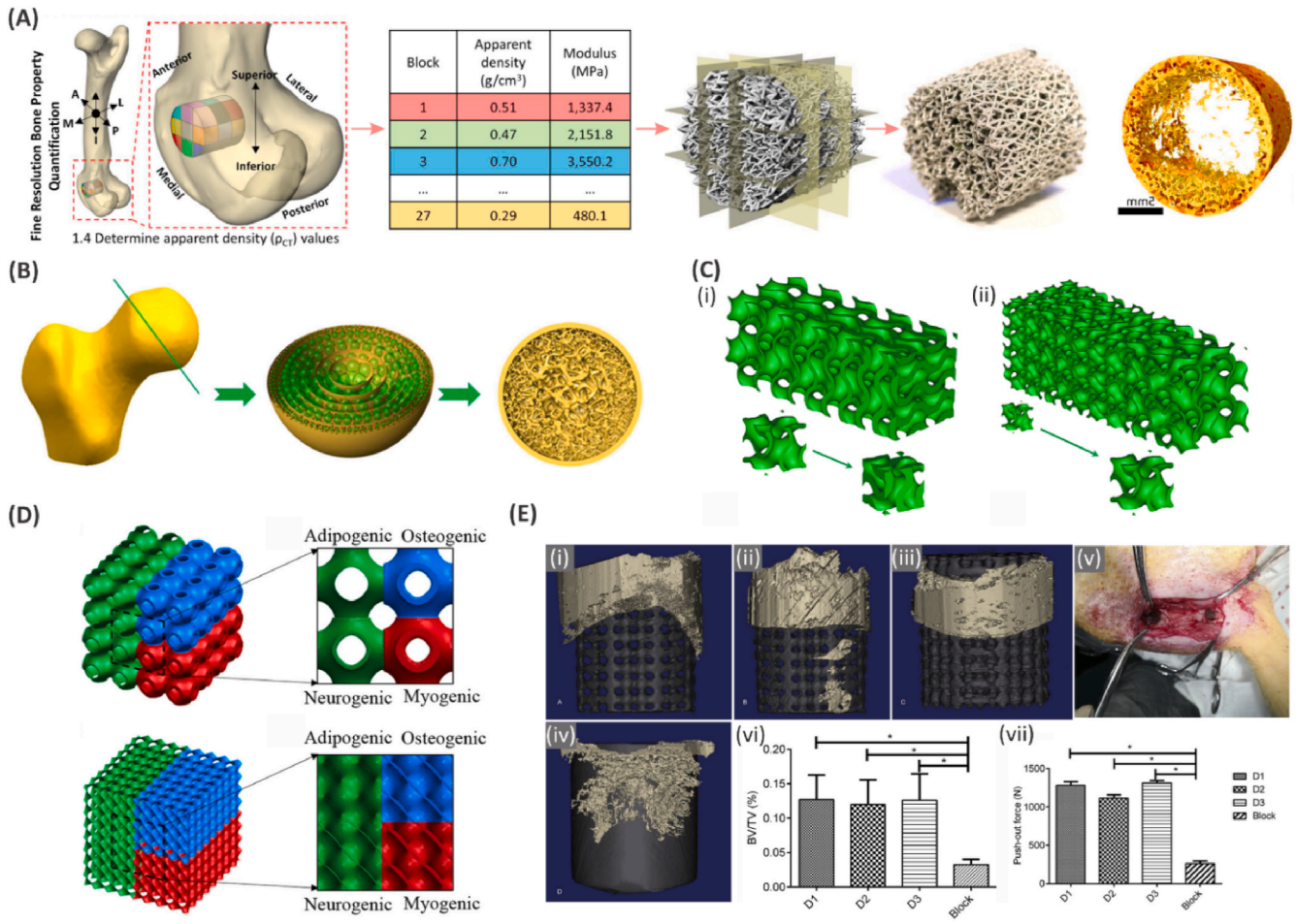

Fig. 6. Examples of functionally graded scaffolds designed to meet conflicting requirements in bone constructs. (A) Stochastic porous scaffold with gradient porosity designed based on the bone's local stiffness. Reproduced with permission from Ref. [175]. Copyright 2019, Elsevier. (B) The steps for generating porous scaffolds using probability spheres with various sizes based on Voronoi-Tessellation approach. Reproduced with permission from Ref. [172]. Copyright 2018, Applied Chemical Society. (C) The sheet-based gyroid architecture with (i) graded porosity generated by varying the sheet thickness and (ii) unit cell size. Reproduced with permission from Ref. [194]. Copyright 2020, Elsevier. (D) Localized stiffness design within the scaffold by changing the sheet thickness to mimic specific tissue types. Reproduced with permission from Ref. [196]. Copyright 2018, American Chemical Society. (E) Bone regeneration within the scaffolds with various pore sizes including (i) 300–500 μm, (ii) 200–600 μm, (iii) 100–700 μm, and (iv) non-porous after the (v) implantation surgery. (vi) Bone volume per total volume and (vii) push-out force (N) of the scaffolds. Reproduced with permission from Ref. [216]. Copyright 2019, Elsevier.

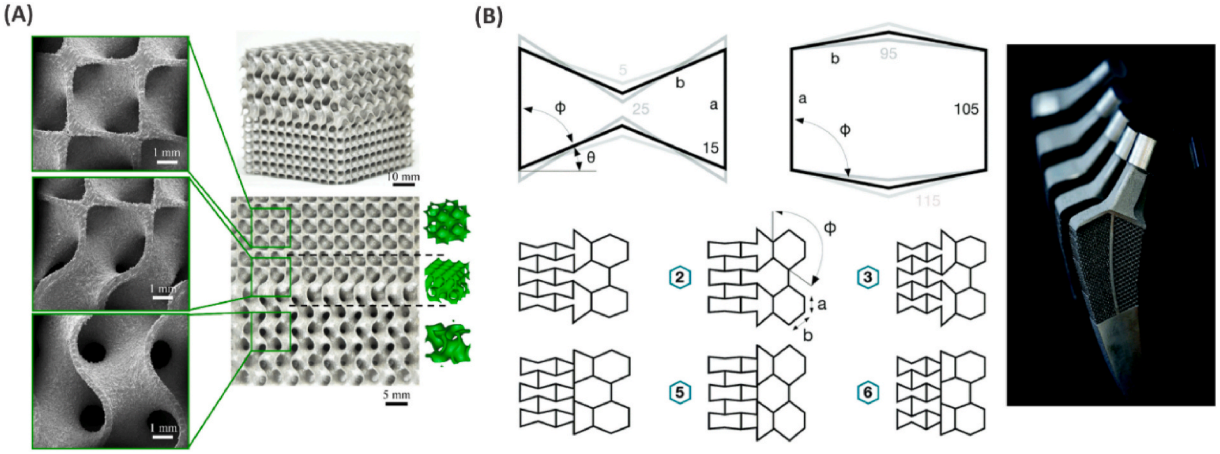

Fig. 7. Examples of porous metallic biomaterials with pore shape gradient. (A) Multiple topologies within the sheet-based TPMS scaffold with a smooth transition from diamond to gyroid. Reproduced with permission from Ref. [194]. Copyright 2020, Elsevier. (B) Hybrid implant designs including conventional and auxetic lattices with various internal angles. Reproduced with permission from Ref. [187]. Copyright 2018, Royal Society of Chemistry.

in porous scaffolds (Fig. 6E). The promoted performance of the scaffolds with graded porosity in osteochondral reconstruction was also confirmed by *in vitro* and *in vivo* studies [215,217,218].

4.3.2. Pore shape gradients

Spatially-varying pore topology is naturally present in porous tissue structures such as trabecular bone. The smooth changes of pore shape enable local control on micro- and macro-scale properties that may not be feasible in uniform topologies. The TPMS designs can be employed for designing multi-pore shape structures with sharp and/or smooth transitions over the pore shapes (Fig. 7A) [194] by defining the weighing functions in the TPMS constitutive equation (Equation (19)). Topology optimization techniques can also be employed to design functionally graded scaffolds with varying pore shapes [219]. Several studies have discussed the effect of scaffold pore shape on tissue ingrowth and vascularization [220,221]. Di Luca et al. [222] fabricated a 3D scaffold with pore shape gradient and analyzed its influence on human-derived mesenchymal stem cells (hMSCs) for osteochondral tissue regeneration applications. This study revealed that rhomboidal pores can facilitate the osteogenic differentiation of hMSCs whereas cubic pores are favored for chondrogenic differentiation. In a recent study, the loosening of hip replacement implants was addressed with a graded pore shape design. Implant loosening primarily arises from the microscale deformations frequently disintegrating implant from the natural bone. Conventional and auxetic pore topologies were designed at the compressive and tensile regions of the hip implant, respectively, to prevent retraction from the host bone during the physiological activities [187]. The designed hybrid implants have been shown to promote integration at the bone-implant interface by generating compressing force onto the bone on both sides of the implant (Fig. 7B).

4.3.3. Material gradients

To mimic the physiological properties of native tissue, scaffolds are required to pose the physical and chemical cues of the native tissue [223–227]. The scaffolds with gradients in the physical and chemical properties have shown promise in mechanical and biological performance [227,228]. For example, it was demonstrated that the scaffolds with functionally graded material distribution could accelerate healing the osteochondral (OC) defects compared to those composed of single and multiphasic material types that individually support bone and cartilage formation [229]. Multimaterial 3D printing is one of the well-known methods for fabricating scaffolds with physical and chemical properties gradients; however, it is mostly used for ink-based 3D printing of multi-material non-metallic implants [230]. Laser-directed energy deposition is the most popular method for multi-material 3D printing of metals. Li et al. [231] used the laser melting deposition method to fabricate a functionally gradient composite of Ti–6Al–4V reinforced with TiC particles while the concentration of TiC was gradually varying from 0% to 50% from bottom to top (Fig. 8A). The amount of unmolten powder and internal microporosity of the structures increased with TiC concentration. The results revealed that increasing TiC particles enhanced the hardness of TiCp/Ti–6Al–4V composites up to 94%. The tensile properties were improved by adding up to 5% TiC while exceeding this amount led to diminished tensile properties. Zhang et al. [232] Fabricated a compositionally graded structure including layers of Ti–6Al–4V, Al_2O_3, and Ti–6Al–4V + Al_2O_3 using LENS process (Fig. 8B). Microhardness and elemental compositions varied over the different layers. Also, taking advantage of LENS fabrication method, Gualtieri et al. [233] manufactured a compositionally gradient structure of vanadium carbide (VC) and stainless steel 304. Various ratios of VC from 5 to 100 wt% were mixed with stainless steel 304 to achieve a wide range of wear resistance and hardness.

5. Characterization of additively manufactured implants

Additively manufactured implants have been studied from different perspectives *via* a variety of numerical and experimental methods to evaluate their performance in terms of quality control, mechanical robustness, as well as a biological function. In the following sections, those aspects of implant characterization that are taken as objective functions in the implant design process, and the approaches followed to meet the requirements are highlighted.

5.1. Structural defects

The AM defects are deviations and manufacturing imperfections raising the risk of failure under physiological loadings. Those defects are due to the inherent layer-by-layer deposition process in the additively manufactured metal implants. The presence of defects can lead to the complete pore occlusion that impedes bone ingrowth or diminish the mechanical strength and lead to implant failure [234]. Therefore, significant attention has been directed at producing defect-free products. There is also a vast literature focused on the types and sources of defects formed during the AM process to understand ways for minimizing defect

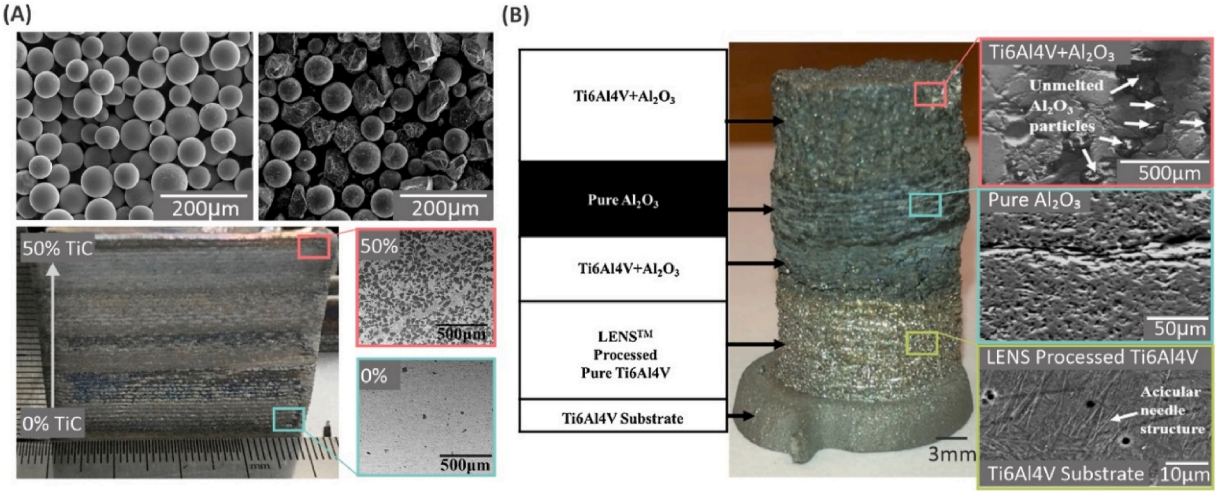

Fig. 8. Examples of the material gradient in metal additive manufacturing (AM) of biomedical structures. (A) Laser melting deposition of Ti–6Al–4V reinforced with TiC particles with various TiC concentrations from 0% to 50% from bottom to top. Reproduced with permission from Ref. [231]. Copyright 2017, Elsevier. (B) Laser-engineered net shaping of multi-material structure with layers of pure Ti–6Al–4V, Ti–6Al–4V + Al_2O_3, and pure Al_2O_3. Reproduced with permission from Ref. [232]. Copyright 2018, Elsevier.

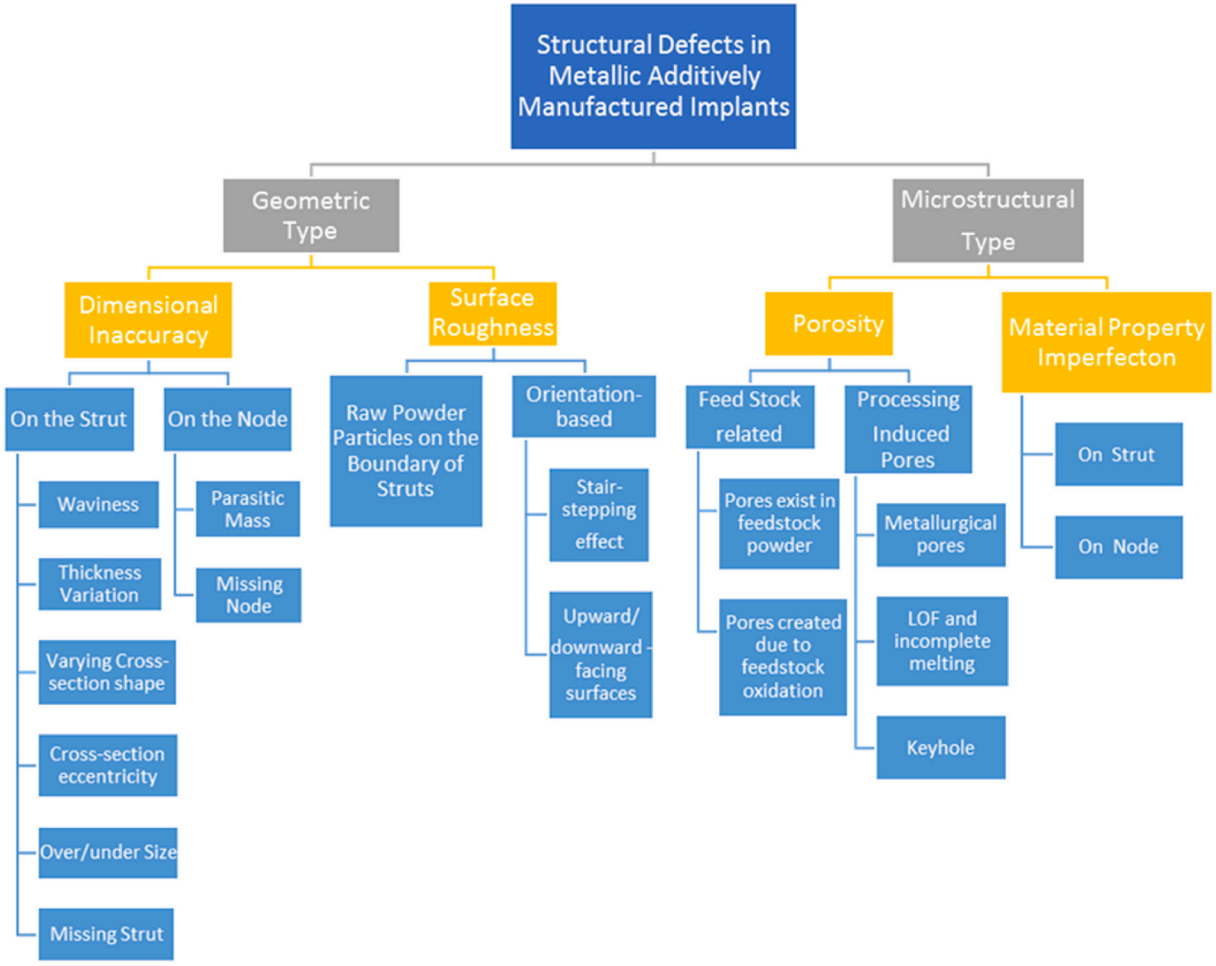

Fig. 9. Classification of different defect types commonly occur in the microstructure of metallic additively manufactured implants (involving nodes and struts) in terms of their sources, components affected, and their effects.

formation. The AM defects are classified into geometric and microstructural imperfections. As shown in Fig. 9, each imperfection type may occur at the nodes or struts and can be sub-categorized based on their effect, source, and the structural elements affected. According to the critical role of the defects in the implant failure and mechanical properties, this section yields a comprehensive review of different aspects of those defects as well as their formation mechanisms in additively manufactured metallic implants.

5.1.1. Geometrical imperfections

Geometric deviations of the AM-made structures from the CAD model can be related to the shrinkage, induced anisotropic residual stresses, and surface roughness (Fig. 10B). These imperfections may happen due to improper process parameters, thermal distortion, and unsuitable laser trajectory [235]. Structural failure and depowdering failure are the most common types of geometrical defects in metal AM of porous scaffolds. The former happens in the case of delicate and tiny features that fail to form completely and the latter is due to clogging of the internal pores that hinders depowdering process (Fig. 10A).

The dimensional accuracy of implants is an important requirement for implant fixation and bone regeneration [235,236]. In lattice structures, dimensional inaccuracies are observed either on the struts or nodes. The strut defects can be classified as strut waviness, strut thickness variations, strut cross-section eccentricity and shape mismatch, strut over-and-under size, and missing/interrupted strut (Fig. 10Ci-iii) [237]. The geometrical deviation of struts because of parasitic mass can cause localized stress concentration [234]. These inconsistencies primarily depend on the orientation of the struts with respect to the building direction. Overhanging struts are affected by accumulation of molten material, regarded as over melting. In the EPBF processed lattice structures, the dimensional errors were generated due to the unoptimized input energy especially around the horizontal strut [238]. They also stem from low heat transfer between solid struts and their circumferential powder [239]. This effect increases the as-built thickness of the struts and offsets the barycenter of the cross-sections from the visionary axis of the struts, thereby leading to waviness, varying thickness, and cross-sectional deviation (circular to ellipsoidal) [240]. Arabnejad et al. [241] demonstrated that the strut diameter is highly influenced by the strut orientation. The vertical struts up to 45% smaller, and the horizontal struts by over 100% larger than the design models were reported. Dimensional inaccuracies on the nodes include two cases of node oversizing and missing nodes. The node oversizing can be attributed to mass agglomeration due to the balling phenomenon and partially molten particles during the AM process which is more obvious in scaffolds at higher relative densities. Fig. 10Civ shows SEM images of mass agglomeration and parasitic mass at the node. This changes the strut geometry from a cylindrical shape to an hourglass [234,242,243].

The surface finish of additively manufactured implants is of utmost importance due to its cell behavior regulatory effect and is primarily engineered at the post-processing steps [242]. In the AM processes, surface roughness is influenced by process type, process parameters, powder size, geometry, and strut inclination angle. Inclination angle affects upward-and-downward facing surfaces and incurs a stair-stepping effect on diagonal struts. The surfaces facing the build bed

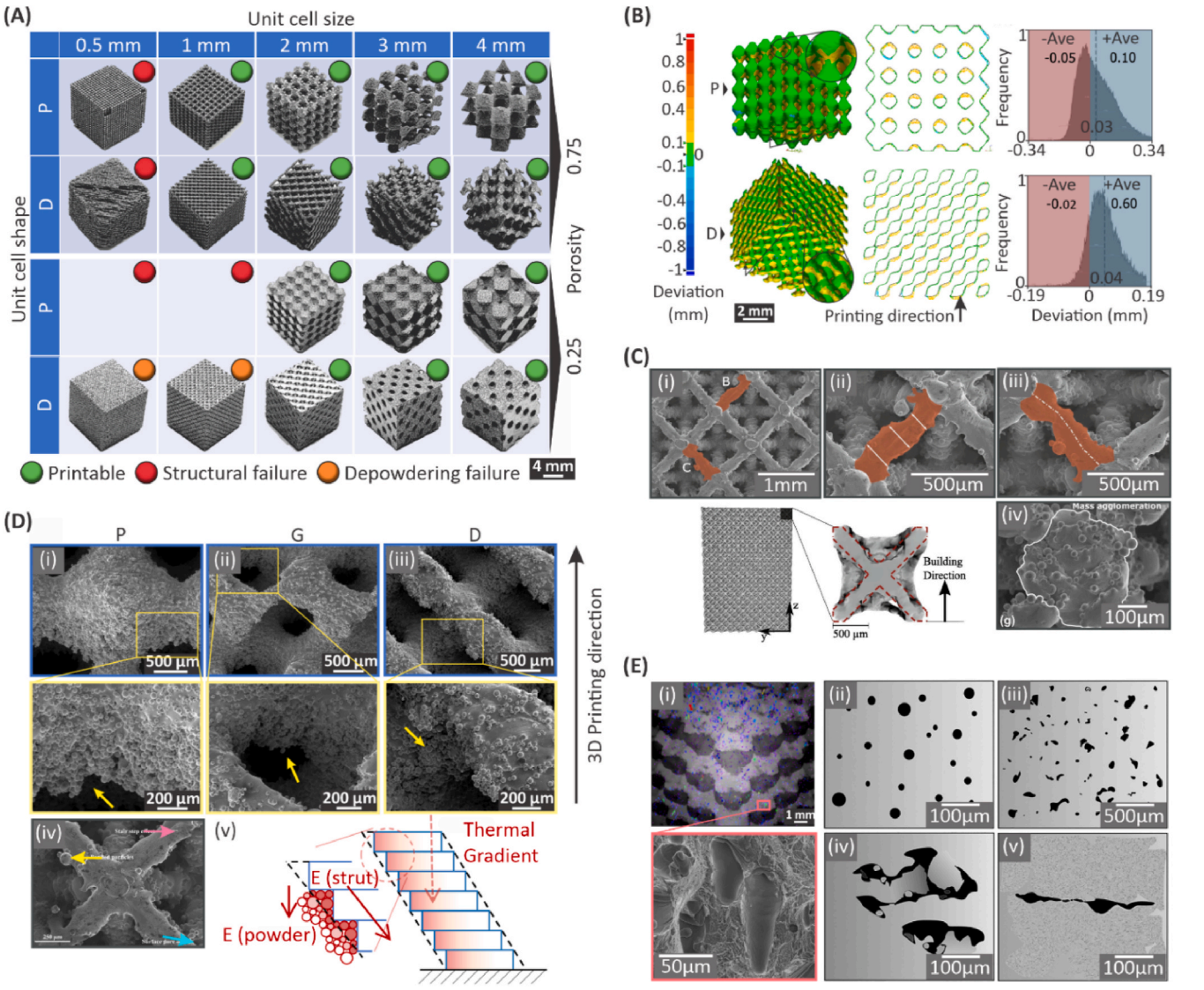

Fig. 10. Structural defects in additively manufactured metal implants. (A) Printability of the triply periodic minimal surface (TPMS) with P and D topologies at various unit cell sizes and macroporosity. Reproduced with permission from Ref. [208]. Copyright 2021, American Chemical Society. (B) Deviation of additively manufactured P and D scaffolds from the computer-aided design (CAD) models. The green color represents a deviation of less than 0.1 mm. Reproduced with permission from Ref. [208]. Copyright 2021, American Chemical Society. (C) (i-iii) heterogeneous thickness, waviness, and misalignment of the structs in a lattice structure. Reproduced with permission from Ref. [237]. Copyright 2017, Elsevier. (iv) Parasitic mass on the nodes. Reproduced with permission from Ref. [243]. Copyright 2020, Cambridge University Press. (D) (i-iii) Aggregation of unmolten powder bonded to the hanging features. Reproduced with permission from Ref. [208]. Copyright 2021, American Chemical Society. (iv) Bonded powders (yellow arrow), stair-step defect (pink arrow), and porosity defect (blue arrow). Reproduced with permission from Ref. [243]. Copyright 2020, Cambridge University Press. (v) Heat transfer in the laser powder bad fusion (LPBF) process resulting in powder bonding defect in the hanging features. Reproduced with permission from Ref. [252]. Copyright 2018, Multidisciplinary Digital Publishing Institute. (E) X-ray tomography of the LPBF processed structure showing the trapped keyhole micropores within the solid phase. Reproduced with permission from Ref. [208]. Copyright 2021, American Chemical Society. Defects in the structures due to the (ii) entrapped gas porosity, (iii) incomplete melting, (iv) lack of fusion (LOF), and (v) cracks. Reproduced with permission from Ref. [246]. Copyright 2019, Wiley-VCH.

are called downward-facing surfaces, and the surfaces with normal vectors away from the bed are called upward-facing. Upward-facing surfaces are fully exposed to the electron/laser beam during the AM process and the heat can be dissipated by the underneath layers; consequently, powders are fully molten. The downward-facing surfaces with no underneath support structure touching the powder bed, overheat due to the poor heat transfer by the unmolten powders. Therefore, when the melt pool solidifies, the unmolten powders adhere to the downward-facing surfaces and augment the surface roughness (almost two times higher than the upward-facing surfaces), as shown in Fig. 10Di-iii. Increasing the inclination angle of the downward-facing surface leads to a smoother surface [235,238]. Yang et al. [244] found that the particles on the downward-facing surfaces of Ti–6Al–4V scaffolds with gyroid architecture fabricated by LPBF were loosely attached while the particles on upward-facing surfaces adhered more rigidly. Besides, the SEM images in this study were indicative of the considerable influence of surface orientation on the surface roughness in the AM processed gyroid structures. In the oriented struts, the thermal gradient leads to a slower heat transfer compared to those of vertical struts (Fig. 10Dv). Therefore, unmolten particles could adhere to the underside surface. Another surface defect that happens due to the layer-wise fabrication of additively manufactured parts is the stair-stepping effect. This effect depends on the factors like the amount of inclination angle and layer thickness. Several studies have reported that the stair-stepping effect is less prominent in the surface-based porous structures (*e.g.*, TPMS-based scaffolds) due to their continuous

topology [238]. In a recent study on LPBF processed lattice structures [243], surface defects such as powder particles bounded to the surface due to the unstable melt pool, spherical surface pores with an average diameter of 80 μm, and stair-stepping effect around the fabricated lattice's nodes were reported (Fig. 10Div). One other type of process-induced surface roughness which is related to the insufficient volumetric energy density is the discontinuous bulging melt track called balling phenomena. Balling effect leads to the formation of spherical beads which cause a rough surface [245]. The surface roughness can impact the fatigue performance, static strength, frictional behavior, fluid flowability, as well as heat transfer in the implant. Therefore, the poor surface quality of the internal struts can diminish the mechanical performance of the porous structures [236]. Nevertheless, certain levels of surface roughness can be biologically favored since the surface roughness has been demonstrated to promote bone growth and osseointegration on the implant surface.

5.1.2. Microstructural imperfections

Internal voids and undesired closed porosities are the defect types that commonly happen in additively manufactured metal structures and must be avoided or minimized to restrict their detrimental effects on mechanical properties. Different types of undesired porosities can be classified based on their origin into (i) feedstock-related pores and (ii) processing-induced pores [246]. These undesired porosities are observed in both bulk and porous structures. Feedstock-related pores are referred to as the pores that originally exist in the feedstock or are created in feedstock due to oxidation [247]. A substantial fraction of internal pores is considered to arise from gas pores that are small spherical pores entrapped in the feedstock. These pores are mobile in the melt pool, and then they are transferred to the as-built parts during metal powder manufacturing [248]. Processing-induced pores can be classified into the following categories: (i) Metallurgical pores (less than 100 μm) with a spherical shape are generated due to rapid solidification during the melting process. They are usually formed along the struts due to the entrapped gases during the manufacturing process [242]. (ii) Lack-of-fusion (LOF) is known as incomplete melting during the AM process. Zhang et al. [236] assigned the formation of the irregular LOF defects to: (i) internal pores from the feedstock powder, (ii) the unstable melt flow, (iii) evaporation of chemical elements, and (iv) insufficient melting between successive layers because of the high scan speed or low laser power. In one study on Al–Si–10Mg alloys [238], the formation of oxide layers was reported to reduce wettability, hinder the flow of melt pool, and thereby incomplete fusion defects. (iii) Keyholes are recognized with large and rounded shapes with sizes of more than 100 μm (Fig. 10Ei). They are usually formed close to the nodes due to rapid solidification of metals that fail to fill the gaps because of high laser power or the low scan speed [242]. The formation of keyholes is attributed to the interactions of solid-liquid-gas phases during the AM process in the melt pool [249]. At the temperatures higher than the powder boiling point, the metal elements can evaporate and push the melts away from the melting zone. Then, a recoil pressure is formed, as a result of which the vapor capillary driven keyhole is developed. Du Plessis [247] reported that LOF is more detrimental than metallurgical and keyhole pores in the structures. Internal pores create stress concentration that has a destructive effect on fatigue properties. Morphology of the microporosities formed due to the trapped keyholes within the solid phase is illustrated in Fig. 10Eii-v. This type of imperfection also depends on the geometrical properties of the structure. Yan et al. [250] showed that, at a constant design relative density, by increasing the unit cell size from 2 mm to 8 mm, the relative density of the manufactured structures reduced by ~9%. The lower relative density of manufactured scaffolds was attributed to the micropores formed during the printing process since the larger printing area led to longer scanning vectors and longer cooling time, thereby forming more micropore void defects. As a result, it was reported that the yield strength and Young's modulus was also decreased with unit cell size due to those defects.

Attenuation of the material properties due to AM process is also a type of imperfection in porous implants. The material properties can be affected by the AM process parameters, and building orientation. Elmi et al. [243] studied the effect of AM defects such as surface, microstructural, as well as material property imperfections on the mechanical properties of lattice structures fabricated *via* the LPBF process. Their results suggest that the nodes demonstrate the largest average local Young's modulus (~6% more than diagonal struts and ~13% greater than horizontal struts). This phenomenon was attributed to the strong material texture and molecular bonding at the node sites. The formation of thermal hotspots in the additively manufactured implants can also lead to uncontrolled and spatially gradient properties throughout the product. The regions with such local heat accumulations experience grain nucleation and growth for more extended periods, leading to different crystalline properties than the surrounding areas. This also leads to residual stresses that cause part distortions and failure sites at the structural scale [251].

5.1.3. Defect prevention

The defect minimization methods can be classified into (i) process parameter optimization, (ii) post-processing methods, (iii) design strategies, and (iv) defect simulation [238] (see Fig. 11). Optimization of AM process parameters can effectively reduce the defects as many studies have been targeting to study the role of process parameters on defect formation. For instance, Sing et al. [253] demonstrated that the LPBF process parameter effects such as hatch space, spot size, scanning speed, laser power, and layer thickness have a significant impact on the porosity, dimensional accuracy, yield strength, as well as the elastic modulus of the as-built lattice structures. In another study, to reduce the dimensional inaccuracy, Maconachie et al. [235] suggested using a laser scan vector that could shift ~50% of laser spot size inwards. Besides, the melt pool size was reduced by decreasing the laser power as well as increasing the scan velocity. In addition to parameters related to the volumetric energy density, powder morphology and size distribution could affect the structure fidelity. Alomar [242] indicated that employing fine metallic powders could improve the surface quality of the additively manufactured structures.

Various post-processing techniques have been introduced to reduce defects. Zhang [236] indicated that hot isostatic pressing (HIP) could heal gas pores, LOFs, and large internal pores; however, surface-connected pores may remain after HIP. For complex geometries such as lattices, chemical treatments (*e.g.* chemical etching, chemical polishing, *etc.*) are more effective than mechanical treatments because they are highly confined by the part's geometry [254]. To satisfy the biological requirements and tailor the interactions of metallic AM Ti–6Al–4V implants with bone, researchers have used hydroxyapatite coatings to reduce surface roughness and improve bioactivity [19]. During the post-processing step, the bonded metal powders are eliminated, and the surface quality excels the original surfaces [255].

Another approach to mitigate AM defects is to design strategies to compensate for deviation from the CAD model. In this regard, Bagheri et al. [239] introduced a design-oriented strategy to reduce strut size deviations in Ti–6Al–4V porous biomaterials manufactured by LPBF. They first built a spider web geometry model by LPBF and after analyzing the errors, established a thickness compensation relation as a function of the strut orientation. Afterward, they applied this strategy to fabricate a tetrahedron-based topology structure. The results exhibit a reduction in thickness deviation of 60%–3% for horizontal struts. Besides, it was illustrated that setting constraints related to the overhanging features can significantly improve the surface roughness and reduce the defects. Calignano et al. [256] illustrated that to minimize the stair-stepping effect, the minimum overhang angle (relative to the bed) in strut-based lattices should be ~30° for LPBF processed Al–S–10Mg and Ti–6Al–4V samples.

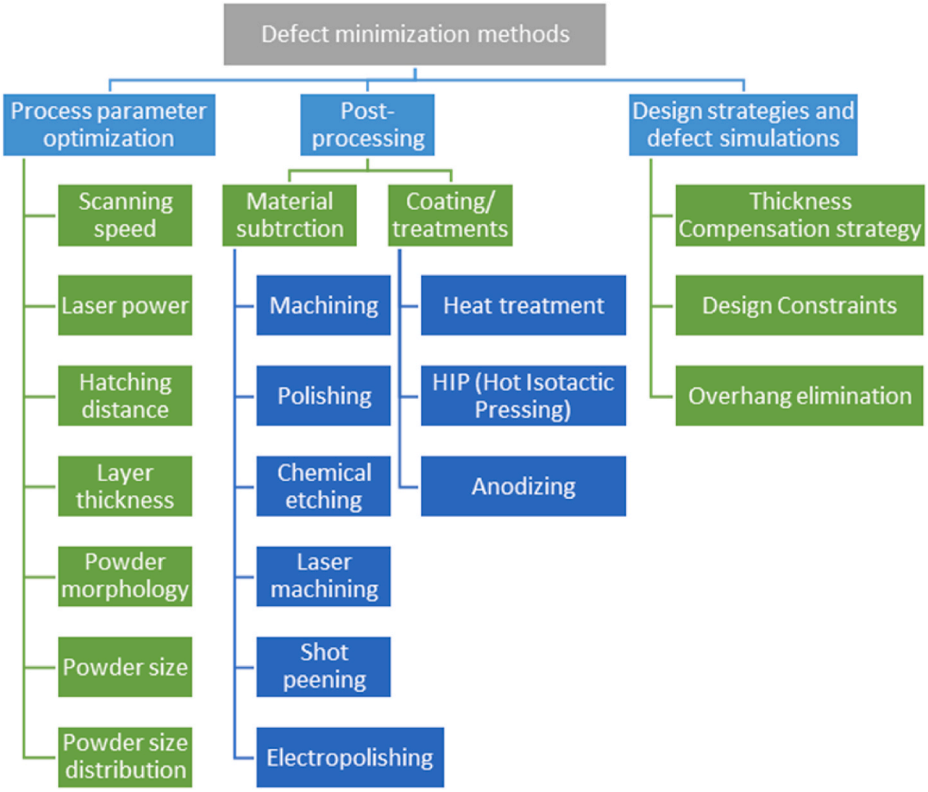

Fig. 11. Classification of methods for minimization of AM defects.

5.1.4. Numerical analysis of manufacturing defects

Introducing defect effects in the numerical modeling techniques reduces the error between numerical and experimental results. This approach enables quantifying the deviations in order to calculate compensation factors [235,257,258]. Various methods exist in the literature for numerical modeling of imperfection effects. For instance, using several beam elements to capture thickness variation defects in struts is one of the potential approaches [258]. Image-based finite element modeling is another method to define defects into numerical models. In this technique, micro-CT analysis is used to capture the fabricated morphology and build a continuum element-based finite element model by the micro-CT results. Since the micro-CT-reconstructed models are computationally expensive, recent studies used the stochastic finite element method (SFEM) to insert defects with their respective statistical distribution. Adopting SEFM in place of the deterministic finite element model enables considering the randomness of the system which leads to higher efficiency [242,259]. Lozanovski et al. [259] used a combination of Markov chains, Monte Carlo simulation (MCS), and finite element analysis to investigate the mechanical properties of lattices that suffer from surface roughness and strut varying thickness defects. They employed CT data to obtain the as-built strut dimension data. Afterward, these digital realizations were applied in the MCS method to calculate the strut thickness distribution and explore the mechanical response of the structure. Liu et al. [234] investigated a combined approach of experiment and numerical simulation to develop a beam-based model with the statistical representation of defects to determine the influence of morphological mismatch between as-designed and as-built lattice structures. Dallago et al. [260] investigated the effect of geometrical AM defects as well as the resulting residual stress on the static and fatigue resistance of the Ti–6Al–4V alloys *via* statistical and finite element simulation. As the impact of defects on the mechanical properties and optimum design of the lattices were indicated earlier, researchers established techniques to implement topology optimization with imperfect unit cell models to do a more accurate investigation. For example, Moussa et al. [257] used probabilistic density distribution of defects to introduce geometric and material uncertainties in the numerical models and formulated a gradient-based topology optimization problem to investigate the influence of process-induced defects on the mechanical properties and density distribution of optimally graded lattices. It was shown that the mechanical properties, unit cell anisotropy, and optimized relative density distribution can be affected by the geometrical defects. For instance, they reported a 23% and 25% difference between the Young's modulus of as-designed and as-built tetrahedron-based structures at an angle of 60° with respect to the build direction and octet-truss structures at an angle of 45°, respectively.

5.2. Elastic mechanical match

Most of the current metal implants have much higher Young's modulus compared to the native bones. The elastic modulus of the cortical bone is in the order of ~20 GPa. Trabecular bone has a significantly lower elastic modulus of ~2 GPa [261,262]. Most bulk metals however, have an elastic modulus of 1–2 orders of magnitude larger than native bone. This mismatch between the mechanical properties would lead to stress shielding, bone weakening, and implant loosening that necessitate follow-up surgeries [263]. After the implantation of the metal implants, most of the physiological loading is carried by the metallic implant and not the host bone tissue. In this process, bone continuously resorbs and loses mass, which causes implant loosening [261]. The orthopedic implants with functionally graded porosity suggest improved biological and mechanical properties. Introducing graded porosity to the solid metallic implants has been introduced as an approach to reduce the local stiffness of the implants at the tissue interface and to mechanically mimic the host tissue. Consequently, this method can prevent stress shielding thereby promoting osseointegration [264]. This approach has motivated many numerical and experimental research studies to enhance long-term stability by optimizing the

gradient parameters [261,263].

5.3. Surface properties

The physical and chemical surface properties of the metallic implants have played a crucial role in osteointegration and stability of the implants. Hence, several studies have suggested surface treatment methods to tailor the cell behavior in response to implantation. To improve osseointegration and suppress the relief of possible cytotoxic compounds such as Al or V in Ti–6Al–4V, the implant surface can be modified with stable oxides to improve integration between bone and implant [265]. It is shown that micro-oxidation of the additively manufactured Ti–6Al–4V leads to the formation of a homogenous thin layer of microporous TiO_2 as well as calcium-phosphate. The *in vivo* studies showed that in the case of treated scaffolds, bone was formed over the entire scaffold's surface and entangled within the porous features, while

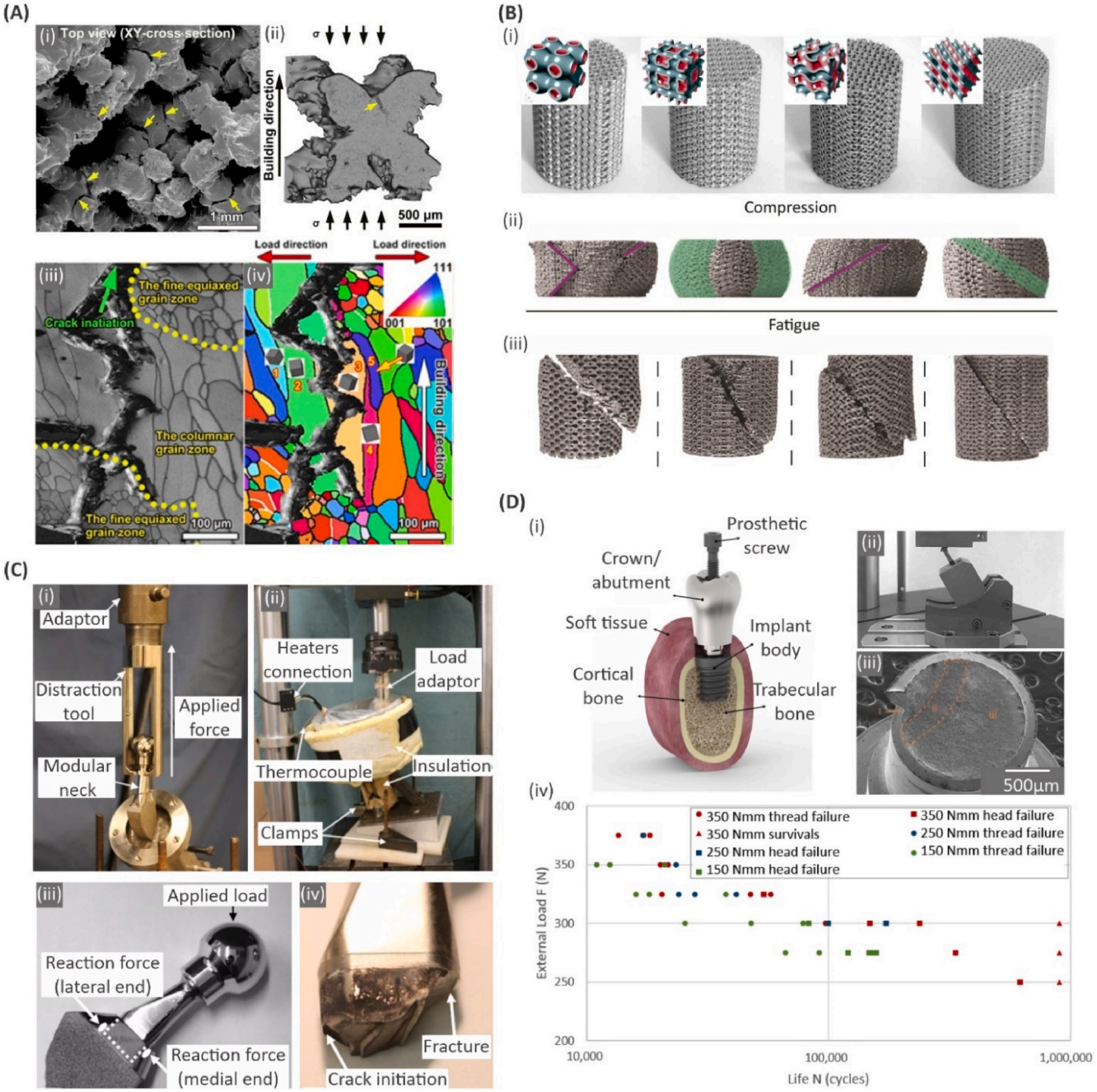

Fig. 12. Fatigue and impact responses in metal implants. (A) Lattice structure (i) after the fatigue test and (ii) the location of the fatigue crack initiation. Detection of fatigue crack propagation in Ti2448 lattice structure using scanning electron microscopy (SEM)-based electron backscatter diffraction (EBSD) technique showing (iii) morphology of single β grains and (iv) EBSD analysis of the struts along the building direction. Reproduced with permission from Ref. [268]. Copyright 2017, Elsevier. (B) Failure modes in (i) P, I-WP, gyroid, and diamond under (ii) static compression loading and (iii) fatigue test. The shear lines are represented in purple. Barreling and diagonal collapsing of layers are highlighted in green. Reproduced with permission from Ref. [270]. Copyright 2017, Elsevier. (C) The hip implant setup for (i) distraction, (ii) fatigue. (iii) Reaction force on the implant's neck. (iv) Crack initiation and fracture locations in the solid hip implant. Reproduced with permission from Ref. [274]. Copyright 2016, Wiley-VCH. (D) Dental implant (i) assembly and (ii) fatigue test setup. (iii) Crack region on the screw thread of the dental implant after fatigue test. (iv) External load-fatigue life (F–N) data for the dental implants under various screw tightening torques. Reproduced with permission from Ref. [275]. Copyright 2020, Multidisciplinary Digital Publishing Institute.

in the untreated scaffolds, bone formation was limited to the periphery of the scaffolds [266]. It was demonstrated that coating Ti–6Al–4V porous scaffolds with polydopamine-hydroxyapatite can enhance the adherence and proliferation of mouse preosteoblast cells (MC3T3). The improved osteointegration, osteogenesis, and cell differentiation were further approved by *in vivo* studies through implantation in a rabbit femoral defect [15]. Bacterial infection at the tissue interface is one of the main complications after implantation. It was shown that the LPBF processed components such as Ti–6Al–4V-xCu with 4 and 6 wt% Cu have robust antibacterial properties and outstanding cytocompatibility with bone marrow cells [267]. Another major concern for implant rejection is debris particles releasing at the bone and implant interface and their contribution to promoting macrophages that trigger osteoclasts [263]. As mentioned earlier, one of the primary defects in additively manufactured implants is poor surface roughness due to the presence of unmolten and partially molten powders that loosely adhere to the implant's surface and cause osteolysis, which is one reason for implant failure due to aseptic loosening. Therefore, surface finish is a necessary step before implantation [262].

5.4. Fatigue performance

Physiological loading applied to the implants during the daily activities is dynamic and repetitive. These types of loads often lead to fatigue crack initiation, propagation, and eventually failure. Fig. 12A demonstrates SEM-based electron backscatter diffraction (EBSD) images of the fatigue fracture surface for a Ti2448 lattice structure, wherein β grains (including columnar and equiaxed grains) are surrounded by fatigue cracks. Here, the crack deflections observed in the columnar grain zone are attributed to the misorientation of the neighboring grains. Fatigue cracks cause major deflections in both equiaxed grain zones and the coarse columnar grain zones [268].

Additively manufactured metals are generally characterized by a shorter fatigue life compared to those of bulk counterparts fabricated by conventional techniques. This mechanical decay is primarily due to the internal defects as well as high surface roughness in additively manufactured structures which can accelerate the crack initiation process. Thus, the fatigue strength of the AM processed metal structures can be partly improved by implementing proper surface finish procedures [269] along with the processes mentioned in section 5.1.3. The sharp regions with the maximum local stress concentration are the most susceptible for fatigue crack initiation and propagation. Hence, lattice nodes in the porous scaffold structures are the most critical components. In this respect, TPMS-based scaffolds offer smooth curvatures, and thereby, they can improve fatigue durability. The fatigue behavior of TPMS structures was studied by Bobbert et al. [270]. In terms of failure mechanism, the static compressive tests demonstrated barreling, layer-by-layer collapse, and 45° shear bands for different pore types (Fig. 12Bi,ii). Fatigue tests results, however, resulted in the formation of 45° shear bands for all pore shapes (Fig. 12Biii). The fatigue life of the structures was in the range of 30,000 to 700,000 cycles where the P topology experienced the shortest fatigue life compared to G, I-WP, and diamond counterparts (despite P structure is known to be a strong stretching dominated architecture compared to the other bending dominated pore architectures). Lietaert et al. [271] designed Ti–6Al–4V lattice scaffolds with radial porosity gradient and studied quasi-static tension, tension-tension, compression-compression, and tension-compression fatigue responses. The fatigue life in tension-tension mode was found to be significantly lower than compression-compression mode. Zhang et al. [272] studied the low cycle fatigue (LCF) performance of additively manufactured Ti–6Al–4V constructs processed *via* LPBF and EPBF technologies. The results showed that compared to LPBF, the EPBF process led to a better fatigue performance at low strain amplitudes but a weaker LCF performance at high strain amplitudes.

Customized fatigue test setups are required for fatigue testing of the implant with complex external geometries. For instance, based on the ISO 7206-4 standard [273], the hip implants are required to be oriented in specific angles while the lower portion of the implant is embedded in a cement-based casting material [274] (Fig. 12Ci, ii). Fatigue cracks in hip implants usually initiate at the modular neck due to the highest stress concentrations in this region (Fig. 12Ciii, iv). The fatigue testing of dental implants is also standardized by ISO 14801 [275]. Fatigue cracks in dental implants usually initiate in the valley of the threads. The fatigue tests on the implants tightened with various screw tightening torques illustrated that although some of the dental implants may fail at the screw head, still, most of the failures relate to the thread section (Fig. 12D).

5.5. Impact performance

Metal implants are commonly exposed to various dynamic impact loads due to physiological movements or external loadings [276]. Similar to fatigue behavior, the intrinsic defects of the additively manufactured constructs lead to their weaker impact resistance compared to that of bulk biomaterials [277]; hence, defect minimization approaches are necessary to enhance the impact response of the implants. The impact resistance and dynamic response of implants can be investigated by operating a direct impact Hopkinson pressure bar system [276]. A high-speed imaging system aligned with the Hopkinson bar can be used to observe the progressive collapse and shock effects in real-time with stress-time data [278]. Harris et al. [279] studied the out-of-plane compression of stainless-steel cellular materials fabricated using LPBF and compared the impact response of two different square honeycomb structures (solid wall and lattice wall). It was shown that the honeycomb structures with lattice walls have a greater energy absorption efficiency at the medium impact velocity (100 ms^{-1}). In another study [280], the mechanical performance of the additively manufactured Ti–6Al–4V lattice structures with uniform and functionally graded porosity under strain rates up to 1000 s^{-1} were investigated by an electronic universal machine and Split Hopkinson Pressure Bar system. The results showed that the specific energy absorption in the graded structures is about 28% higher than the uniform structures. It was also demonstrated that by increasing the strain rate from 0.001 s^{-1} to 1000 s^{-1}, the collapse strength of the graded lattices elevates by ~25%. Radford et al. [281] specified three features playing role in the dynamic response of square honeycomb structures of the stainless steel samples. These features include rate sensitivity of the material, inertial stabilization of buckling phenomena, and plastic wave propagation effects. When the impact velocity increased (from 0 to 50 ms^{-1}), the two first features resulted in the front and back face stresses. However, by raising the impact velocity above 50 ms^{-1}, the third feature was dominant in the front face stress while back face stress was relatively independent of speed.

5.6. Mass transport and permeability

Mass transport plays a crucial role in the effective exchange of nutrients and wastes required for cell proliferation and differentiation [282,283]. To facilitate this process, porous scaffolds are required to be highly interconnected thereby supporting biofluid flow from inside the pores. Permeability and diffusivity are important design criteria, by which the pore characteristics (such as pore shape, porosity, and pore size [284]) are evaluated in terms of their potential for conducting internal fluid flow to quantify the tissue ingrowth capability of the scaffold [285,286]. In essence, permeability and diffusivity represent how easy it is for the cells inside the porous implants to be nurtured and oxygenated, and the wastes or metabolic byproducts to be carried away. Many studies have declared significant correlations between permeability and biological characteristics of the scaffolds. According to Darcy's law, the permeability coefficient (k) relates pressure gradient to mass flux according to Equation (20) [287]:

$$k = \frac{Q\mu L}{A\Delta P} \tag{20}$$

where Q, μ, L, A, and ΔP represent flow rate, the dynamic viscosity of the fluid, sample length, cross-section area, and pressure drop within the scaffold, respectively. Based on Fick's first law, the diffusivity also relates diffusion flux to the concentration gradient according to Equation (21) [288].

$$J = -D\frac{dc}{dx} \tag{21}$$

where D is the diffusion coefficient of penetrant and $\frac{dc}{dx}$ represents the concentration gradient along the *x*-direction. Computational fluid dynamics (CFD) is a popular design tool for predicting the microscale flows and analysis of permeability [282]. In addition to permeability, fluid dynamics-induced shear stress plays an important role as mechanical stimuli for cell growth. Accordingly, cell nutrition, cell oxygenation, and eventually, cell proliferation and differentiation are strongly interrelated with the analysis of fluid-solid interactions in scaffold structures [283,289].

Recent studies have emphasized matching scaffold permeability to that of natural bone tissue [284]. Zhang et al. [290] studied the permeability of graded Ti–6Al–4V scaffolds over a wide range of porosity (38–75%) and pore size (250–450 μm). Their findings suggest that the permeability of graded scaffolds (0.129×10^{-9} m^2-0.491×10^{-9} m^2) was in the range of human bone. Li et al. [282] assessed the mass transport properties of porous lattice structures with diamond, octet truss, and rhombic dodecahedron unit cell types. The diamond structure was characterized with a more homogeneous shear stress distribution compared to octet truss and rhombic dodecahedron, offering a better environment for tissue regeneration and improved fixation. However, octet truss and rhombic dodecahedron exhibited higher maximum velocity compared to diamond structure. Ali et al. [291] studied cubic gyroid and lattice-based scaffolds with various porosities. The results of CFD analysis suggested that high porosity leads to the decreased wall shear stress and increased permeability for both architectures. However, at the same porosity, gyroid models showed a lower permeability and higher wall shear stress compared to those of lattice-based architectures. Shuai Ma et al. [284] evaluated the relationships between permeability and cell ingrowth in the gyroid scaffolds with various porosities (75.1–88.8%) and pore sizes (500–1300 μm) (Fig. 13B). To measure experimental permeability, a piezometric pressure sensor was used to measure the pressure drop between the two ends of the samples and permeability at different flow rates was calculated based on the experimental setup shown in Fig. 13Bi. The measured permeability for the samples ranged in 0.29×10^{-9} to 3.91×10^{-9} m^2, which was close to trabecular bones. Permeability decreased with flow rate specially in the case of scaffolds with larger macropores (Fig. 13Bii). Additionally, the pressure and velocity fields were studied using CFD simulations (Fig. 13Biii-v). The *in vitro* studies here showed that permeability plays a key role in cell proliferation as the highest cell numbers was observed in scaffolds with the largest porosity (~88%) after 7 days of cell culture.

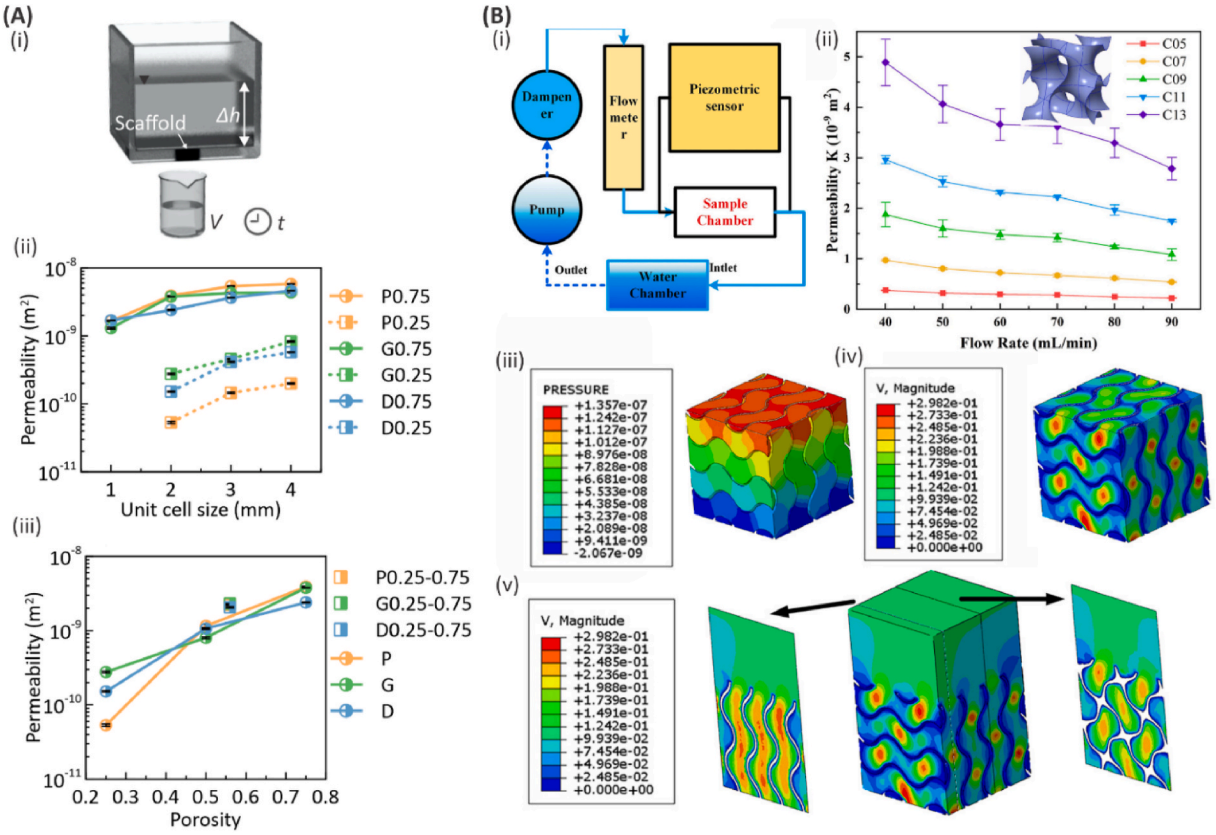

Fig. 13. Permeability analysis of porous metal additively manufactured scaffolds. (A) (i) Permeability setup for measuring the permeability of triply periodic minimal surface (TPMS) cubic scaffolds with P, G, and D topologies at different (ii) unit cell sizes and (iii) porosities. The value beside P, G, and D illustrate the porosity of the scaffolds and P0.25–0.75 represent the scaffolds with gradient macroporosity. Reproduced with permission from Ref. [208]. Copyright 2021, American Chemical Society. (B) Permeability analysis of TPMS scaffolds with G topology. (i) The schematic diagram of permeability setup. (ii) Permeability changes with flow rate for the scaffolds with various pore sizes. The samples labeled with C05, C07, C09, C11, and C13 have pore sizes of 500, 700, 900, 1100, and 1300 μm. (iii) Pressure distribution, (iv) velocity distribution, and (v) velocity distribution within vertical and horizontal cross-sections of the scaffold. Reproduced with permission from Ref. [284]. Copyright 2020, Elsevier.

6. Applications in regenerative medicine

Recent studies have demonstrated the capability of additively manufactured metal implants at promoting tissue integration through various *in vitro* and *in vivo* studies [292]. In addition, metal AM has led to enormous success in advancing customized medicine and personalized prostheses [293] as well as quick operation planning of surgical guides [294] by integrating different bioactive materials as discussed in section 3. For instance, Ti alloys are the most popular medical grade metallic materials mainly due to superior biocompatibility and corrosion resistance, making them a great candidate for cranial replacements, dental implants, joint replacement, *etc*. Besides, Ta has a high biocompatibility and corrosion resistance comparable to Ti, although the higher elastic modulus and density can increase the risk of stress-shielding issues. Incorporating porosity within Ta implants enables their application in bone implants. Ta can also be used as a coating for bone/implant interface due to their osseointegration properties [295]. Co–Cr alloys not only offer high corrosion resistance, but also enhance hardness and strength compared to Ti alloys. Hence, they are mostly used as dental substitutes and knee replacements [128]. Ferrous alloys such as stainless steel have lower corrosion resistance compared to Ti and Co–Cr alloys, so they are mostly suitable as temporary implants and screws, as well as surgical tools. While the implants fabricated from metallic alloys are usually non-biodegradable, Mg alloys enable biodegradation to allow bone regeneration [129]. Due to the unique shape memory performance of smart alloys, they are mostly used for making actuators, stents, and

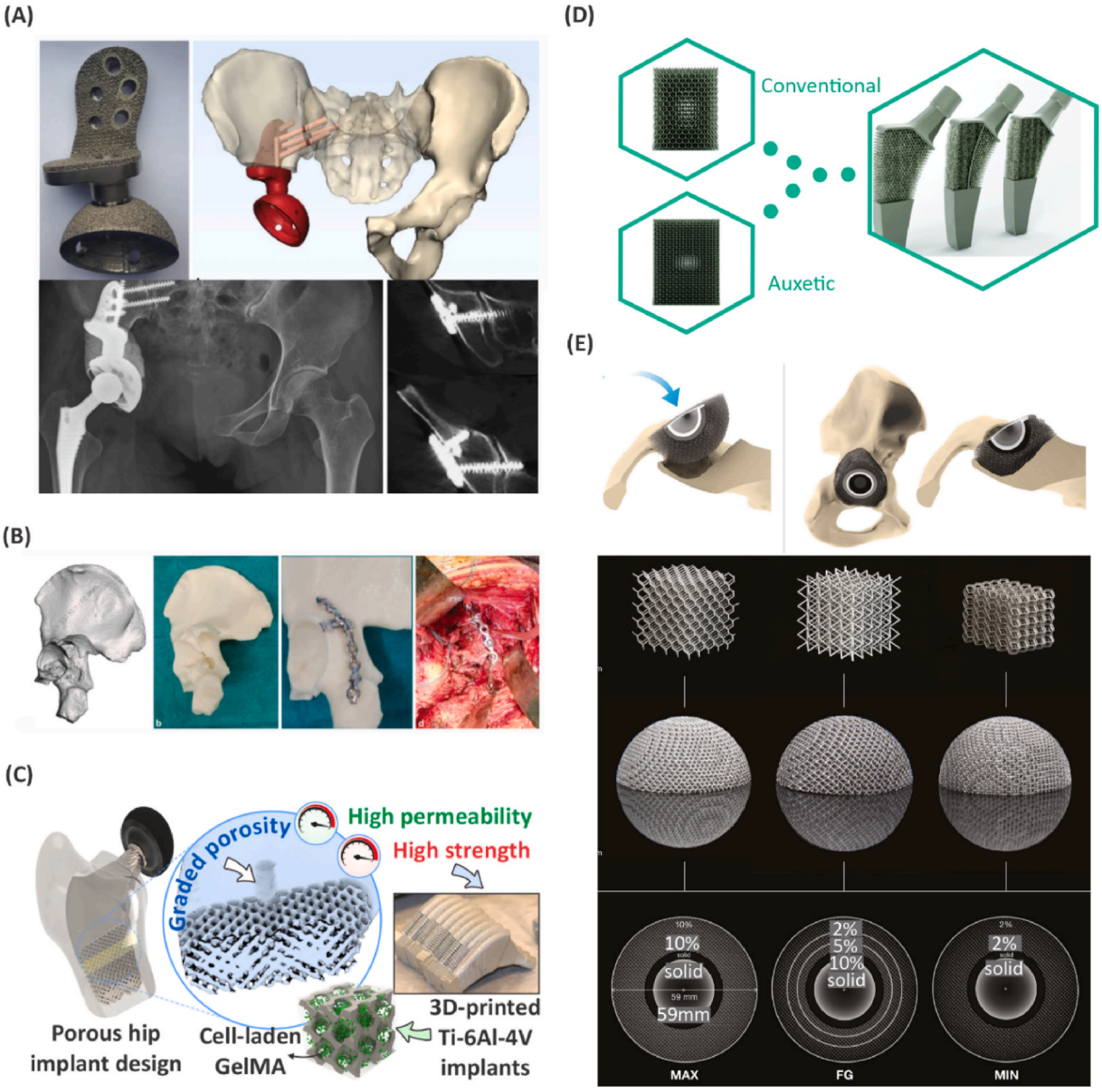

Fig. 14. Application of metal additive manufacturing (AM) for skeletal bone implants. (A) Metallic pelvic prosthesis fabricated by electron beam powder bed fusion (EPBF) technology. Reproduced with permission from Ref. [308]. Copyright 2019, Springer Nature. (B) Fracture fixation in the pelvis by an additively manufactured metallic prosthesis. Reproduced with permission from Ref. [308]. Copyright 2019, Springer Nature. (C) Functionally graded porous metallic hip implant for biopermeability (higher designed macroporosity at the periphery) and enhanced mechanical strength (lower macroporosity at the center) can be integrated with cell-laden gelatin methacryloyl (GelMA) due to its high peripheral permeability. Reproduced with permission from Ref. [208]. Copyright 2021, American Chemical Society. (D) Hybrid hip implants including conventional and auxetic lattice topologies to prevent implant retraction from the bone. Reproduced with permission from Ref. [187]. Copyright 2018, Royal Society of Chemistry. (E) Deformable orthopedic implants architected with conventional lattice design at various relative densities. Reproduced with permission from Ref. [185]. Copyright 2021, Elsevier.

shape memory wires or springs for cardiovascular applications. In the following sections, the latest contributions of AM in addressing the needs for regeneration of different tissue types are elaborated.

6.1. Skeletal bone

Skeletal bone is the essential internal framework that performs vital functions, including supporting, moving, protecting, and storing minerals. Events such as accidents, trauma, war casualties, obesity, and even aging, may cause significant bone loss, raising the need for bone and joint replacements (Fig. 14A and B). Natural bone consists of an anisotropic complex internal microstructure. Replicating such delicate features requires advanced AM techniques [296,297]. The common AM materials for implants include Ti-based blends, Co–Cr-based compounds, NiTi shape memory alloys, firm stainless steels, and Ta [298].

Next-generation implants are aimed to customize these implant structures according to the patient needs with engineered internal porosity for tissue integration. The high stiffness of the bulk Ti alloys such as Ti–6Al–4V (Young's modulus of 17–20 GPa and yield strength of 131–224 MPa) compared to natural bone, is one of the main reasons for long-term bone resorption [299–301]. Gradient pore designs can be applied to implant structures to provide mechanical matching at the tissue interface. Fig. 14C represents a functionally graded porous hip implant with higher porosity at the periphery (tissue interface) for enhanced biopermeability and reduced stiffness closer to natural bone, as well as less porosity at the center for improved mechanical strength. Kolken et al. [187] manufactured a hybrid meta-implant including negative (auxetic) and positive Poisson's ratios materials, which could prevent implant retraction from the adjacent bone upon physiological loadings (Fig. 14D). In another study [185], they designed an acetabular cup including outer lattice layers with different relative densities (Fig. 14E). The porous layer could deform upon movements leading to the improvement in stability and fixation of the implant. The other advantages of the designed porous implants include reduction of stress shielding and maintaining bone density (osteopenia). Attar et al. [302] fabricated porous composite specimens based on Ti–TiB with various porosities of 10%, 17%, and 37% using LPBF. It was observed that elastic modulus, yield, and ultimate strengths were reduced with porosity in specimens. A 37% porous Ti–TiB compound showed an elastic modulus and yield strength similar to the human skeletal bone [303]. Li et al. [304] proposed Ti–Nb–Ta–Zr compounds with stiffness of about 48–55 GPa (almost half of Ti–6Al–4V) for the fabrication of metal implants. To further push the elastic modulus close to that of cortical bone, the Ti–45Nb alloy with 13% porosity and compressive elastic modulus of about 11 GPa was made by the LPBF technique [305].

Biodegradable metal alloys have also been reported as load-bearing skeletal bone implants for temporary applications to support bone regeneration [286]. Carluccio et al. [306] proposed an LPBF processed Fe–35Mn bone implant with mechanical properties suitable for load-bearing applications. The implants were characterized by biocompatibility, cell adhesion, and biodegradation properties. Shuai et al. [307] used a mechanical alloying technique to prepare a supersaturated solid solution. The newly developed alloy could improve the degradation rate of the Fe–Mg LPBF processed implants to mimic the bone regeneration rate.

6.2. Spinal cord

Spinal cord injury (SCI), also known as the central nervous system (CNS) disorder, is a major burden to the healthcare system. It has been reported that in the United States alone, near 450,000 patients struggle with this disease each year. Although significant progress has been made thus far in clinical treatments, still therapeutics are failed to completely recover the nerve functions [309]. Biomimetic 3D scaffolds have been a potential solution as an alternative approach to restore the damaged nervous system. Additive manufacturing of spinal cord implants for repairing damaged spinal cords has been a potential solution. Many requirements should be met in the scaffold design for the treatment of SCI. Biocompatibility is an essential factor for axonal growth since axonal regeneration is promoted by contact-mediated guidance by the scaffolds. Functionalizing the surface of the scaffolds with biological molecules, such as full-length proteins enhances axonal growth and mimics a natural extracellular matrix [310,311]. Moreover, the biostability (refers to stability in response to the physiological environment) of the spinal implants is crucial along with choosing the optimal material with proper mechanical characteristics [312]. The Ti-based alloys are well-known in AM of metallic implants for the treatment of spinal cord injuries due to their attractive properties such as biocompatibility and corrosion resistance [313]. Various types of additively manufactured metallic prostheses have been introduced for reconstructing anterior column and vertebral defects (Fig. 15). Girolami et al. [314] illustrated the anterior column reconstruction using a customized metal prosthesis fabricated by EPBF technology. The prosthesis included a lattice design at the center of the implant (mimicking cancellous bone structure) and a fine shell to resemble the cortical bone (Fig. 15A). Willemsen et al. [315] developed a customized 3D printed prosthesis to bridge the unstable parts to the nearest stable vertebra. As demonstrated in Fig. 15B, the implant involved a solid main cylindrical part, proximal protrusion (supporting the inferior endplate) as well as a distal protrusion (supported on the superior endplate).

Additively manufactured fusion cages can be utilized for the treatment of cervical spondylotic myelopathy (CSM) by cervical corpectomy which is common in individuals older than 55 years and patients with cervical spondylosis [316]. Yang et al. [317] implemented an *in vivo* study on the artificial vertebral body (AVB) developed by the EPBF technique. They illustrated that the mechanical properties of the manufactured implants with interconnected porosity were comparable to that of cancellous bone and can be effective in minimizing the stress-shielding effect (Fig. 15D). The porous ultrastructure of the AVB could encourage osteoinduction. In a case study by Chung et al. [318], a large vertebral defect was substituted with a 3D printed Ti cage fusion for a patient who had a car accident and whose thoracic spine was injured. It was concluded that 3D-printed implants can be adequate options for the treatment of severe spinal injuries.

6.3. Craniofacial bone

The craniofacial skeleton plays an essential role in supporting overlaying facial soft tissue including muscles, nerves, and blood vessels. Traumatic head injuries, congenital defects, and cancer are the common conditions that lead to loss of craniofacial bones and arise the need for craniofacial surgeries and bone substitutions [1]. Although autografts and allografts have been the first choices for the treatment of craniofacial defects, they have some disadvantages such as limited resources and fitting with the shape of the defected tissue. The precise design of the craniofacial substitutions and mimicking the shape of the defected tissue is critical due to the essential role of the craniofacial bones in eating, vision, airway, audition, speech, brain function, facial symmetry, and social stigmatization [319].

New imaging technologies in combination with metal AM have enabled personalized solutions. Bone defects can be scanned by a CT scanner to generate the CAD model of the defected area. Bone substitutions then can be designed in accord with the patient's bone topology. Finite element analysis can be integrated with these platforms for the mechanical design of bone constructs. The human skull is composed of 22 bones each of which has different physical properties. Cranium implants should be fabricated of tough materials to assure effective protection of the brain from intense stresses. Orbital floor bones, however, do not require as high strength as the cranium. The Ti alloys are the most common metallic substitutions used in craniofacial surgeries, among which Ti–6Al–5V is well-known as a biocompatible metal widely used in AM cranium fixation components (*e.g.*, screws,

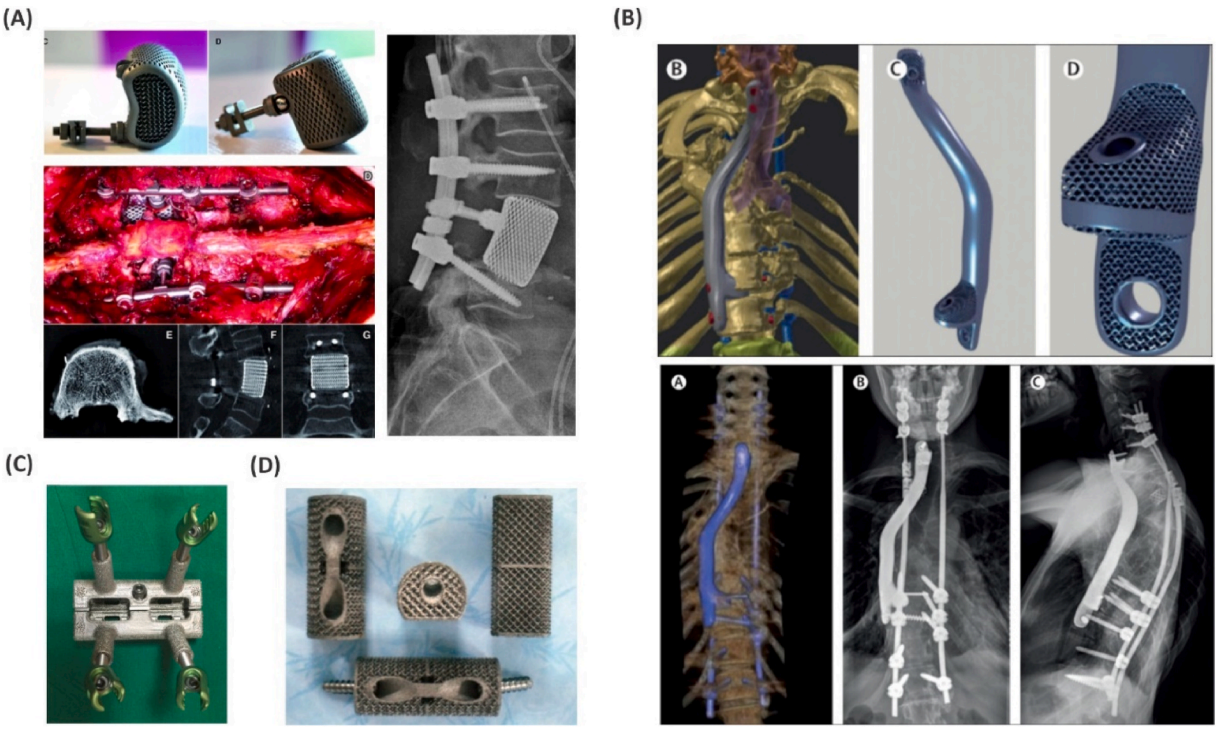

Fig. 15. Applications of metal additive manufacturing (AM) in spinal cord tissue regeneration. (A) Anterior column reconstruction using a customized metal prosthesis fabricated by electron beam powder bed fusion (EPBF) technology. The prosthesis includes a lattice design at the center of the implant that mimics cancellous bone and a fine shell to resemble the cortical bone. Reproduced with permission from Ref. [314]. Copyright 2018, Springer Nature. (B) Customized 3D printed prosthesis to bridge the unstable parts to the nearest stable vertebra. Reproduced with permission from Ref. [315]. Copyright 2019, Elsevier. (C) Reconstructing large vertebral defects using a 3D printed metal prosthesis. Reproduced with permission from Ref. [318]. Copyright 2019, Elsevier. (D) Porous self-stabilizing vertebral body prosthesis. Reproduced with permission from Ref. [317]. Copyright 2014, Lippincott Williams & Wilkins.

plates, and meshes) [319]. Fig. 16Ai summarizes the cranial implant design procedure. First, a 3D model of the skull is obtained through CT imaging. Then, the model is divided *via* the mid-plane. The healthy side is then used to reconstruct the defective area. Fixation lips *i.e.*, tapered holes for the screws are also introduced to the implant model for stable attachment and fixation of the implant to the target zone. After determining design volume, internal porous designs are conducted by patterning unit cells into the generated implant solid model (Fig. 16Aii). Before the development of the final metallic implants, plastic models of the skull and implant can be fabricated by desktop plastic 3D printers to evaluate the fitting and precision of the design (Fig. 16Aiii) [320]. Various types of customized 3D-printed metallic cranial implants and surgical guides for non-human primates have been introduced in the literature (Fig. 16B) to fix specific chambers or guides for access to different regions of the brain. Mandibular reconstruction has been addressed by metal AM technologies (Fig. 16C and D). Yan et al. [321] developed a porous Ti-based prosthesis for whole mandible replacement. After X-ray imaging and reconstruction of the 3D model of the human mandible, the proper porosity and pore size for the reliable strength were calculated using finite element analysis, and the customized mandibular prosthesis was additively manufacturing using EPBF technology (Fig. 16Di). It was demonstrated that the strength of the manufactured prosthesis enhances and reaches the strength of the native mandible after 12 months from implantation (Fig. 16Dii, iii) [321].

6.4. Dental

Dental implants are used to replace damaged or missing teeth and are considered a routine treatment for mouth rehabilitation. However, complications such as peri-implantitis and marginal bone loss remain major challenges [324,325]. Ehlers-Danlos syndrome affects the connective tissues such as those in the mouth and jaw. This disease limits the process of oral construction and healing of edentulous patients [326]. Hence, to improve the quality of life for patients, a vast number of studies have been conducted to address these concerns and increase the duration, aesthetics, and functionality of implants [327].

Biomaterials used for dental applications should be considerately selected. These materials must be strong enough to withstand cyclic forces. The average of the axial bite forces for normal humans varies in different areas of the jaw and may reach 500 N in the canine area, 600 N in the premolar area, and 800 N in the molar area [328]. The β-type Ti alloys with high wear resistance and low elastic modulus closely mimic human bone and its composites are shown to effectively inhibit the stress shielding effects [329]. In addition, Co–Cr metallic alloys are also widely used in dental implants. Bassoli et al. [330] studied the mechanical properties of Co–Cr–Mo, and Ti–6Al–4V alloys processed by LPBF. The elongation at break, tensile strength, densification, and hardness of the two alloys mentioned in this study were in close agreement with the values reported in the datasheets for the dental application, regardless of their built orientation. In another study, Revilla-Leon [331] investigated the effects of surface roughness, chemical composition, as well as the ceramic shear bond strength of metal frameworks fabricated with subtractive and AM processes for the Co–Cr dental implants. Meaningful changes in topographical properties and surface roughness were observed due to their different chemical compositions and AM procedures [332]. The metal-ceramic shear bond strength in the Co–Cr alloys was not found to be sensitive to manufacturing parameters [331]. The bonding strength of porcelain to LPBF manufactured Co–Cr alloys was ~67 ± 15 MPa, which is acceptable for dental applications [333,334]. Khan and Dickens [335] used a 24-carat gold powder to additively manufacture dental crowns for providing adhesion for porcelain-fused-to-metal implants. Xiong et al. [328] developed a porous Ti–6Al–4V scaffold with dense cores of varying diameters for

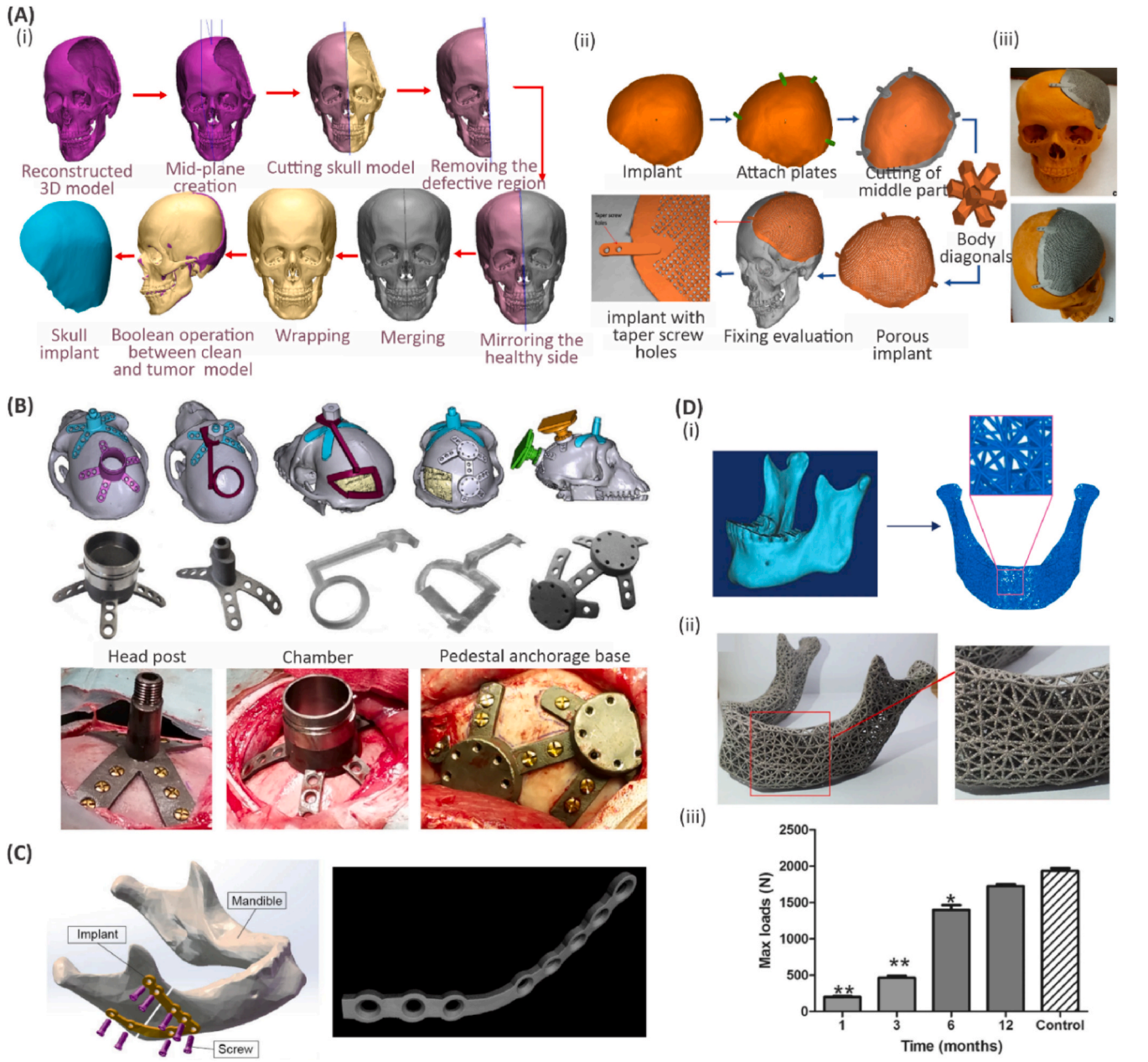

Fig. 16. Applications of metal AM in craniofacial implants and maxillofacial reconstructions. (A) Design steps for (i) bulk cranial implant and converting to (ii) porous implant. (iii) 3D printed metallic cranial implant on the skull. Reproduced with permission from Ref. [320]. Copyright 2017, Elsevier. (B) Customized models of cranial implants and guide for non-human primates. Reproduced with permission from Ref. [322]. Copyright 2017, Elsevier. (C) Customized V-shaped craniomaxillofacial 3D-printed metallic implant. Reproduced with permission from Ref. [323]. Copyright 2020, Elsevier. (D) (i) Designing 3D human mandible porous model. (ii) Metal 3D printed mandibular scaffold. (iii) Mechanical characterization of the mandibular scaffold after implantation. After 12 months from implantation, the strength of the implant was about the strength of the native mandible. Reproduced with permission from Ref. [321]. Copyright 2018, Springer Nature.

dental implants (Fig. 17A). They examined the fatigue performance and mechanical properties of the additively manufactured structures and investigated osseointegration responses through *in vitro* and *in vivo* tests. It was demonstrated that designing a dense core in a porous structure can significantly enhance the mechanical properties while maintaining the desired porosity for osseointegration. Among different specimens, PT-1.8 (porous Ti structure with a 1.8 mm diameter solid core) showed the best mechanical properties. A clinical study investigated the manufacturing of a metal-based denture using LPBF for the treatment of the Ehlers-Danlos syndrome (Fig. 17B) [336]. It was shown that metal bases are useful in the production of dentures with limited restorative space. Fig. 17C illustrates the most common techniques used in dental implant production to develop bioactive surfaces while combining antimicrobial activity to maximize healing and antibacterial capacities and consequently improve osseointegration [337].

7. Clinical translation

Metals have been used to manufacture body implants since the 1950s [338]. Traditional manufacturing techniques have been utilized for fabricating prostheses during the last decades and yet, they fail to meet fundamental requirements such as long-term stability and tissue integration. Since the late 1980s, AM techniques were used to prototype biomedical models and devices for application in tissue regeneration.

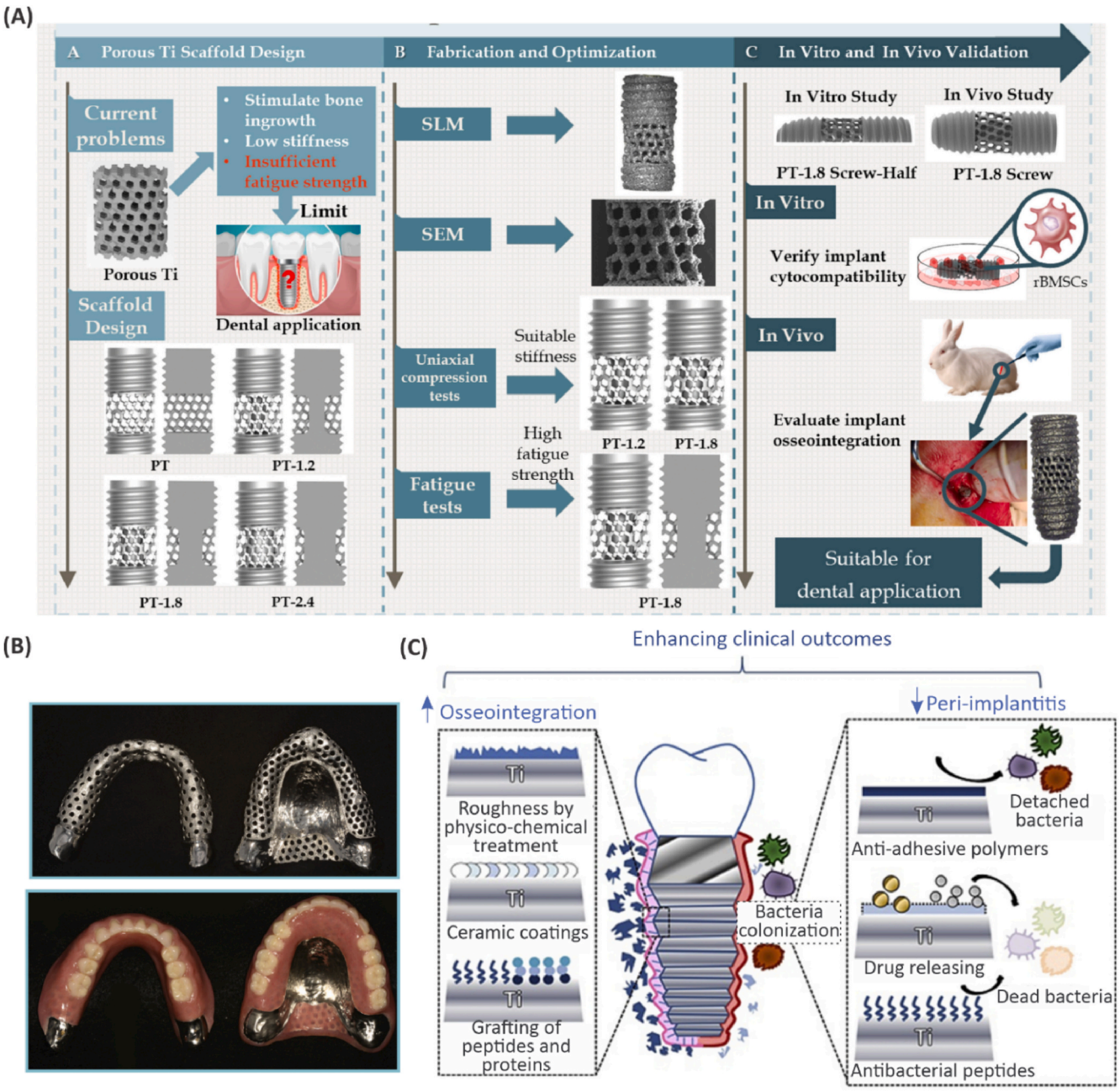

Fig. 17. Application of metal AM in dental implants. (A) The design and experimental steps for a three-dimensional (3D) printed metallic dental implant. Reproduced with permission from Ref. [328]. Copyright 2020, Elsevier. (B) (i) 3D printed metallic maxillary and mandibular base for dentures (ii) Complete denture including the metallic base. Reproduced with permission from Ref. [336]. Copyright 2020, Elsevier. (C) Surface functionalization of the dental implants for improved osseointegration and controlling the peri-implantitis issues. Reproduced with permission from Ref. [337]. Copyright 2019, Multidisciplinary Digital Publishing Institute.

Nevertheless, the AM implants have not achieved full approval for clinical implantation in many countries [330,339]. Significant efforts have been made towards clinical translation of additively manufactured implants to address challenges in orthopedic surgery not only for manufacturing the implants and medical tools but also for producing training tools. Being able to simulate a complex surgery provides surgeons with valuable experience before performing the actual procedure [340]. The medical industry has been using digital imaging for a long time. Mating those imaging technologies and CAD with the advanced metal AM techniques has motivated a surge of interest towards clinical translation of personalized medicine approaches for tissue regenerative applications [341].

Mandible reconstruction surgery is an extremely invasive procedure. Inflammation, trauma, and tumors may cause mandibular defects and necessitates reconstructive surgical operations. Conventional surgical approaches rely on reconstruction Ti plates and autograft bone substitutions. Patients going through the operation utilizing conventional replacement methods suffer from complications such as joint pain, lower mouth opening range, asymmetric facial contour, and implant loosening [341,342]. To improve surgical outcomes, the use of AM for fabricating mandibular prostheses has been researched. Xia et al. [342] conducted a case study where additively manufactured metal prostheses in mandible surgery were evaluated and compared to that of conventional methods. In this study, a total of 20 patients were selected. Customized 3D printed implants were inserted for 4 patients and conventional methods were applied to the remaining 16 patients. Lower operative time and

increased post-operative recovery were the two most significant advantages in the case of additively manufactured implants. Grecchi et al. [343] additively manufactured a full mandibular customed prosthesis and implanted it in a 67-year-old patient. Traditional reconstruction techniques were difficult due to the state of the patient's mandible. The AM was especially useful since the complexity of the design could not allow its manufacturing *via* the traditional techniques. As expected, Ti alloys, especially Ti–6Al–4V, play an important role in manufacturing customized mandibular implants.

In the medical industry, AM is the most accepted in dental applications [344]. Metal AM methods enable manufacturing dental implants such as crowns and bridges. Different materials have been studied to determine the suitability of different metallic biomaterials such as gold, titanium, chromium, and their alloys [335,344,345] for commercial implementation. Using the conventional methods, it takes up to 2 weeks for the dental crowns to be manufactured for a temporary crown placement [345]. To reduce the manufacturing time and problems related to this delay, AM has been suggested as an alternative manufacturing technique.

Overall, the AM technologies have seen a greater acceptance in medical applications over the last few years. In 2007, only 2 research articles were published regarding AM medical implementation whereas, in 2017, the number of published articles increased to 68 [340]. This increasing interest has provided clinicians with better information on the advantages of such technological advancements. The AM is revolutionizing the medical industry, but some are yet skeptical since long-term effects on patients have not been yet proved even in the dental industry where AM has the most acceptance [346]. Great advantages are clear when applying AM to medical such as the ability to manufacture complex designs, less waste material, and better prosthesis acceptance by the body. On the other hand, important disadvantages and uncertainties are still present. High cost, long-term effects, and government regulations represent some of the most important challenges of AM [340,344]. In the years to come, AM is expected to gain more attention in medical applications.

Several additively manufactured metal implants have been FDA-approved for commercialization. The iFuse porous titanium implants, developed by SI-BONE Inc. for sacroiliac (SI) joint treatment, demonstrated better bone fixation at the clinical trials [347]. Osseus Fusion Systems have introduced their patient-specific porous spinal implants that could be manufactured in demanded sizes and shapes based on the surgeon's needs. The high porosity of the manufactured implants (*i.e.*, ~80%) has led to products with mechanical properties close to natural bone [348]. Stryker developed additively manufactured porous Tritanium® TL curved posterior lumbar cage with pore shapes mimicking that of cancellous bone [349]. The FDA-approved craniofacial titanium implants designed by BioArchitects and processed by EPBF technology are lightweight and possess greater tensile strength over their conventional counterparts where separate attachments and brackets are used to fix the plate in place [350]. Recently, the first customized talus 3D printed cobalt-chromium implant for the ankle joint was approved by FDA [351]. Furthermore, NGMedical introduced a Ti cervical implant based on a honeycomb structure, namely BEE cage design, approved recently for better bone proliferation [352]. An ongoing effort is currently under progress by the orthopedic companies to obtain FDA approval for additively manufactured metal implants.

8. Conclusions and future perspectives

Metal AM techniques have revolutionized the design and processing of implantable biomaterials, in particular, for hard tissue regeneration. Those techniques have opened new opportunities towards personalized treatment plans for the regeneration of a wide range of tissue types such as bone, cartilage, and dental components. Simultaneously, CAD methods have advanced to facilitate modeling processes based on the imaging data obtained from the patients to address their specific needs. Complex design problems, however, require expensive computational tools. The STL models of porous scaffolds (particularly those comprising of a large number of unit cells) have a large file size, and therefore, it is often difficult to import them into the commercial AM machines. Besides, post-processing and modification of those STL files are time-consuming if not impossible. Given the augmented interest in porous unit cell topologies, the current commercially available CAD software still lacks proper toolboxes for direct modeling of mathematically defined TPMS-based unit cells. Likewise, more user-friendly modules are required for defining lattice-based unit cell networks. Toolpath generation algorithms can be further adapted specifically for scaffolds with repetitive unit cells. Current design models are often unnecessarily large as they replicate data of the same unit cell to define the final geometry; hence, efficient CAD file formats and computational modeling processes may be developed for efficient design and toolpath generation for metal AM implants by eliminating that repetitive information. With the aid of machine learning (ML) tools in combination with metal AM techniques, many obstacles in adopting AM for the industries that need high-throughput high-precision parts can be addressed. Due to the complexity of the metal AM and the multitude of processing parameters, metallic AM parts usually deviate from the designed model. Integrating ML in different stages of fabrication, from design to process optimization, post-processing, and quality control can improve the quality of the end part. The ML algorithms can be trained by previous datasets to predict the optimized process parameters and consequently minimize the inconsistency of the AM parts [353,354]. Since incorporating ML in metal AM is a new approach, there is still space for generating high-quality supervised and unsupervised ML algorithms and adopting active learning to further improve prediction accuracy.

The current AM technologies have shown great flexibility for integration with different metal biomaterials. However, switching the powder material in AM machines is a difficult process and requires an expert operator. This issue necessitates further attention to AM techniques such as DED for their further expansion in biomedical applications. Although the currently high manufacturing times using AM do not present a major obstacle for personalized treatments, the slow AM process hinders industrial mass production of metal implants and solutions for production rate is of high demand. Furthermore, more efforts are required to identify approaches to prevent anisotropic properties in the additively manufactured components while the heat treatment and topology optimization methods are evolving to address this issue.

The AM machines can be further advanced in many ways to add more functionalities to the implant structures. *In situ* monitoring of the 3D printing process for instance, is one emerging way of improving quality control. Self-training algorithms can be developed to eliminate the structural defects in AM biomedical products. Likewise, artificial intelligence can help automate the entire AM process for instance, by setting the printing parameters according to the design topology and metal biomaterial type. It is envisioned that enabling the current metal 3D printers to produce multi-material structures, can lead to a paradigm shift towards smart self-sensing implants. In this scenario, *in situ* structural health monitoring of the implants may be pursued by co-3D printing of the implant structure with sensing elements, as well as energy harvesting piezoelectric materials [355–359]. Those sensing elements may enable the long-term monitoring of physical failures and evolutions, as well as chemical changes around the implant structures (*e.g.*, to monitor the release of metal ions or detached metal particles). Simultaneous printing of biological components in composites with biopolymers (such as hydrogels) [360,361] along with metals has not been touched in the literature due to the harsh and incompatible printing conditions demanded by metals. Feasibility studies on the heat transfer characteristics of melt pool for potential integration of those biological moieties (and hydrogels [362]) within the metallic structures can also open up new directions for research and development. In addition, advanced metal 4D printing approaches can be pushed forward to adapt the implant structures with long-term physiological

changes of the natural bone. Likewise, more understanding of the degradable metallic biomaterials and development of predictive models for their overtime changes in physical properties and biological responses are necessary.

Porous internal architecture design has been recently paid significant attention in the literature due to its critical role in achieving long-term integration *in vivo*. While topology optimization techniques continue to address mechanobiological requirements of tissue scaffolds, a surge of interest has been directed at the ordered porous structures based on the different unit cell designs. The state-of-the-art research is currently emphasizing the capability of gradient designs to meet the conflicting needs in scaffold design and thereby, the *in vitro* and *in vivo* characterization of gradient scaffolds are under rigorous investigation. The research progress on graded scaffolds thus far has primarily addressed the implant retraction-induced loosening, stress shielding effects, as well as strength-permeability design conflicts. Further research is encouraged to recapitulate the natural gradients such as bone-cartilage interface for their regeneration. The overall success achieved by additively manufactured metal implants from both biological and physical perspectives suggests the promising potential of metal AM techniques as an alternative to traditional manufacturing methods for the development of functional and durable implant structures.

Declaration of competing interest

None.

Acknowledgements

The authors acknowledge funding from the National Institutes of Health (1R01AR073135-01A1). The authors appreciate the financial support of The Natural Sciences and Engineering Research Council of Canada (NSERC), and Network for Holistic Innovation in Additive Manufacturing (HI-AM).

References

[1] D.O. Visscher, E. Farre-Guasch, M.N. Helder, S. Gibbs, T. Forouzanfar, P.P. van Zuijlen, J. Wolff, Advances in bioprinting technologies for craniofacial reconstruction, Trends Biotechnol. 34 (2016) 700–710.
[2] E. Davoodi, Additive Manufacturing of Architected Structures for Healthcare Applications, Mechanical and Mechatronics Engineering, University of Waterloo, Waterloo, 2021.
[3] M. Coffigniez, L. Gremillard, S. Balvay, J. Lachambre, J. Adrien, X. Boulnat, Direct-ink writing of strong and biocompatible titanium scaffolds with bimodal interconnected porosity, Addit. Manuf. 39 (2021), 101859.
[4] P. Kumar, U. Ramamurty, Microstructural optimization through heat treatment for enhancing the fracture toughness and fatigue crack growth resistance of selective laser melted Ti6Al4V alloy, Acta Mater. 169 (2019) 45–59.
[5] P. Renner, S. Jha, Y. Chen, A. Raut, S.G. Mehta, H. Liang, A review on corrosion and wear of additively manufactured alloys, J. Tribol. 143 (2021), 050802.
[6] N. Taniguchi, S. Fujibayashi, M. Takemoto, K. Sasaki, B. Otsuki, T. Nakamura, T. Matsushita, T. Kokubo, S. Matsuda, Effect of pore size on bone ingrowth into porous titanium implants fabricated by additive manufacturing: an *in vivo* experiment, Mater. Sci. Eng. C 59 (2016) 690–701.
[7] E. Davoodi, M. Zhianmanesh, H. Montazerian, A.S. Milani, M. Hoorfar, Nanoporous anodic alumina: fundamentals and applications in tissue engineering, J. Mater. Sci. Mater. Med. 31 (2020) 60.
[8] A.A. Al-Tamimi, C. Peach, P.R. Fernandes, A. Cseke, P.J.D.S. Bartolo, Topology optimization to reduce the stress shielding effect for orthopedic applications, in: *3rd Cirp Conference On Biomanufacturing* vol. 65, 2017, pp. 202–206.
[9] T. Iqbal, L. Wang, D. Li, E. Dong, H. Fan, J. Fu, C. Hu, A general multi-objective topology optimization methodology developed for customized design of pelvic prostheses, Med. Eng. Phys. 69 (2019) 8–16.
[10] A. Rahbari, H. Montazerian, E. Davoodi, S. Homayoonfar, Predicting permeability of regular tissue engineering scaffolds: scaling analysis of pore architecture, scaffold length, and fluid flow rate effects, Comput. Methods Biomech. Biomed. Eng. 20 (2017) 231–241.
[11] M. Zhianmanesh, M. Varmazyar, H. Montazerian, Fluid permeability of graded porosity scaffolds architectured with minimal surfaces, ACS Biomater. Sci. Eng. 5 (2019) 1228–1237.
[12] F.H. Kim, F.H. Kim, S.P. Moylan, in: Literature Review of Metal Additive Manufacturing Defects, US Department of Commerce, National Institute of Standards and Technology, 2018.
[13] X. Li, X.D. Jia, Q.B. Yang, J. Lee, Quality analysis in metal additive manufacturing with deep learning, J. Intell. Manuf. 31 (2020) 2003–2017.
[14] W.Y. Cui, Y.L. Zhang, X.C. Zhang, L. Li, F. Liou, Metal additive manufacturing parts inspection using convolutional neural network, Appl. Sci. 10 (2020) 545.
[15] Y. Li, W. Yang, X. Li, X. Zhang, C. Wang, X. Meng, Y. Pei, X. Fan, P. Lan, C. Wang, X. Li, Z. Guo, Improving osteointegration and osteogenesis of three-dimensional porous Ti6Al4V scaffolds by polydopamine-assisted biomimetic hydroxyapatite coating, ACS Appl. Mater. Interfaces 7 (2015) 5715–5724.
[16] S. Mellor, L. Hao, D. Zhang, Additive manufacturing: a framework for implementation, Int. J. Prod. Econ. 149 (2014) 194–201.
[17] H. Attar, S. Ehtemam-Haghighi, D. Kent, M.S. Dargusch, Recent developments and opportunities in additive manufacturing of titanium-based matrix composites: a review, Int. J. Mach. Tool Manufact. 133 (2018) 85–102.
[18] D. Dev Singh, T. Mahender, A. Raji Reddy, Powder bed fusion process: a brief review, Mater. Today Proc. 46 (2021) 350–355.
[19] M. Doubenskaia, A. Domashenkov, I. Smurov, P. Petrovskiy, Study of selective laser melting of intermetallic TiAl powder using integral analysis, Int. J. Mach. Tool Manufact. 129 (2018) 1–14.
[20] R. Esmaeilizadeh, U. Ali, A. Keshavarzkermani, Y. Mahmoodkhani, E. Marzbanrad, E. Toyserkani, On the effect of spatter particles distribution on the quality of hastelloy X parts made by laser powder-bed fusion additive manufacturing, J. Manuf. Process. 37 (2019) 11–20.
[21] L. Cao, Mesoscopic-scale numerical investigation including the inuence of process parameters on LPBF multi-layer multi-path formation, Comput. Model. Eng. Sci. 126 (2021) 5–23.
[22] E. Toyserkani, D. Sarker, O. Ibhadode, F. Liravi, P. Russo, K. Taherkhani, Metal Additive Manufacturing, first ed. ed., John Wiley & Sons Ltd, Hoboken, New Jersey, USA, 2021.
[23] E. Hosseini, V.A. Popovich, A review of mechanical properties of additively manufactured inconel, Addit. Manuf. 30 (2019), 100877.
[24] H. Fayazfar, M. Salarian, A. Rogalsky, D. Sarker, P. Russo, V. Paserin, E. Toyserkani, A critical review of powder-based additive manufacturing of ferrous alloys: process parameters, microstructure and mechanical properties, Mater. Des. 144 (2018) 98–128.
[25] A. Keshavarzkermani, R. Esmaeilizadeh, U. Ali, P.D. Enrique, Y. Mahmoodkhani, N.Y. Zhou, A. Bonakdar, E. Toyserkani, Controlling mechanical properties of additively manufactured hastelloy X by altering solidification pattern during laser powder-bed fusion, Mater. Sci. Eng., A 762 (2019), 138081.
[26] R. Olsson, J. Powell, A. Palmquist, R. Branemark, J. Frostevarg, A.F.H. Kaplan, formation of osseointegrating (bone integrating) surfaces on titanium by laser irradiation, J. Laser Appl. 31 (2019), 022508.
[27] S. Bremen, W. Meiners, A. Diatlov, Selective laser melting, Laser Technol. J. 9 (2012) 33–38.
[28] M.K. Kolamroudi, M. Asmael, M. Ilkan, N. Kordani, Developments on electron beam melting (EBM) of Ti-6Al-4V: a review, Trans. Indian Inst. Met. 74 (2021) 783–790.
[29] S. Biamino, A. Penna, U. Ackelid, S. Sabbadini, O. Tassa, P. Fino, M. Pavese, P. Gennaro, C. Badini, Electron beam melting of Ti-48Al-2Cr-2Nb alloy: microstructure and mechanical properties investigation, Intermetallics 19 (2011) 776–781.
[30] M. Larsson, U. Lindhe, O. Harrysson, Rapid Manufacturing with Electron Beam Melting (EBM) - A Manufacturing Revolution, 2003 International Solid Freeform Fabrication Symposium, 2003.
[31] L.E. Murr, S.M. Gaytan, A. Ceylan, E. Martinez, J.L. Martinez, D.H. Hernandez, B. I. Machado, D.A. Ramirez, F. Medina, S. Collins, R.B. Wicker, Characterization of titanium aluminide alloy components fabricated by additive manufacturing using electron beam melting, Acta Mater. 58 (2010) 1887–1894.
[32] D. Herzog, V. Seyda, E. Wycisk, C. Emmelmann, Additive manufacturing of metals, Acta Mater. 117 (2016) 371–392.
[33] D.G. Ahn, Directed energy deposition (DED) process: state of the art, Int. J. Precis. Eng. Manuf. 8 (2021) 703–742.
[34] W.S.W. Harun, M.S.I.N. Kamariah, N. Muhamad, S.A.C. Ghani, F. Ahmad, Z. Mohamed, A review of powder additive manufacturing processes for metallic biomaterials, Powder Technol. 327 (2018) 128–151.
[35] B.E. Carroll, T.A. Palmer, A.M. Beese, Anisotropic tensile behavior of Ti-6Al-4V components fabricated with directed energy deposition additive manufacturing, Acta Mater. 87 (2015) 309–320.
[36] M. Yan, P. Yu, An Overview of Densification, Microstructure and Mechanical Property of Additively Manufactured Ti-6Al-4v—Comparison Among Selective Laser Melting, Electron Beam Melting, Laser Metal Deposition and Selective Laser Sintering, and with Conventional Powder, Sintering Techniques of Materials, 2015. IntechOpen.
[37] J.X. Fang, S.Y. Dong, Y.J. Wang, B.S. Xu, Z.H. Zhang, D. Xia, P. He, The effects of solid-state phase transformation upon stress evolution in laser metal powder deposition, Mater. Des. 87 (2015) 807–814.
[38] G.P. Dinda, L. Song, J. Mazumder, Fabrication of Ti-6Al-4V scaffolds by direct metal deposition, Metall. Mater. Trans. 39a (2008) 2914–2922.
[39] J. Yang, F.D. Wang, 3D finite element temperature field modelling for direct laser fabrication, Int. J. Adv. Manuf. Technol. 43 (2009) 1060–1068.
[40] A. Saboori, A. Aversa, G. Marchese, S. Biamino, M. Lombardi, P. Fino, Application of directed energy deposition-based additive manufacturing in repair, Appl. Sci. 9 (2019), 3316.
[41] B.V. Krishna, W.C. Xue, S. Bose, A. Bandyopadhyay, Functionally graded Co-Cr-Mo coating on Ti-6Al-4V alloy structures, Acta Biomater. 4 (2008) 697–706.
[42] J. Yu, M. Rombouts, G. Maes, F. Motmans, Material properties of Ti6Al4V parts produced by laser metal deposition, Phys. Procedia 39 (2012) 416–424.

[43] V.K. Balla, S. Bodhak, S. Bose, A. Bandyopadhyay, Porous tantalum structures for bone implants: fabrication, mechanical and *in vitro* biological properties, Acta Biomater. 6 (2010) 3349–3359.

[44] J.J. Marattukalam, A.K. Singh, S. Datta, M. Das, V.K. Balla, S. Bontha, S. K. Kalpathy, Microstructure and corrosion behavior of laser processed niti alloy, Mater. Sci. Eng. C 57 (2015) 309–313.

[45] D. Svetlizky, M. Das, B. Zheng, A.L. Vyatskikh, S. Bose, A. Bandyopadhyay, J. M. Schoenung, E.J. Lavernia, N. Eliaz, Directed energy deposition (DED) additive manufacturing: physical characteristics, defects, challenges and applications, Mater. Today 49 (2021) 271–295.

[46] F.A. España, V.K. Balla, S. Bose, A. Bandyopadhyay, Design and fabrication of cocrmo alloy based novel structures for load bearing implants using laser engineered net shaping, Mater. Sci. Eng. C 30 (2010) 50–57.

[47] J. Cornie, D. Brancazio, P. Williams, M. Cima, E. Sachs, Three dimensional printing: rapid tooling and prototypes directly from a CAD model, J. Ind. Eng. Int. 114 (1992) 481–488.

[48] I. Gibson, D.W. Rosen, B. Stucker, Additive Manufacturing Technologies, 2014. Springer.

[49] C.L. Cramer, P. Nandwana, R.A. Lowden, A.M. Elliott, Infiltration studies of additive manufacture of Wc with Co using binder jetting and pressureless melt method, Addit. Manuf. 28 (2019) 333–343.

[50] K. Inaekyan, V. Paserin, I. Bailon-Poujol, V. Brailovski, Binder-jetting additive manufacturing with water atomized iron powders, in: Proceedings of the AMPM 2016 Conference on Additive Manufacturing, Held with MPIF/APMI International Conference on Powder Metallurgy & Particulate Materials, Boston, MA, USA, 2016.

[51] W. Du, X. Ren, C. Ma, Z. Pei, Binder Jetting Additive Manufacturing of Ceramics: A Literature Review, ASME 2017 International Mechanical Engineering Congress and Exposition, American Society of Mechanical Engineers Digital Collection, 2017.

[52] S.-J.L. Kang, Sintering: Densification, Grain Growth and Microstructure, Elsevier, 2004.

[53] A. Yegyan Kumar, J. Wang, Y. Bai, S.T. Huxtable, C.B. Williams, Impacts of process-induced porosity on material properties of copper made by binder jetting additive manufacturing, Mater. Des. 182 (2019), 108001.

[54] A. Basalah, Y. Shanjani, S. Esmaeili, E. Toyserkani, Characterizations of additive manufactured porous titanium implants, J. Biomed. Mater. Res. Part B 100B (2012) 1970–1979.

[55] Y. Bai, C.B. Williams, An Exploration of binder jetting of copper, Rapid Prototyp. J. 21 (2015) 177–185.

[56] M. Li, W. Du, A. Elwany, Z. Pei, C. Ma, Metal binder jetting additive manufacturing: a literature review, J. Manuf. Sci. Eng. 142 (2020).

[57] A. Bailey, A. Merriman, A. Elliott, M. Basti, in: Preliminary Testing of Nanoparticle Effectiveness in Binder Jetting Applications, 27th Annual International Solid Freeform Fabrication Symposium, 2016, pp. 1069–1077.

[58] A. Park, B. Wu, L.G. Griffith, Integration of surface modification and 3D fabrication techniques to prepare patterned poly(L-lactide) substrates allowing regionally selective cell adhesion, J. Biomater. Sci. Polym. Ed. 9 (1998) 89–110.

[59] A. Butscher, M. Bohner, C. Roth, A. Ernstberger, R. Heuberger, N. Doebelin, P. R. von Rohr, R. Muller, Printability of calcium phosphate powders for three-dimensional printing of tissue engineering scaffolds, Acta Biomater. 8 (2012) 373–385.

[60] C. Wu, W. Fan, Y. Zhou, Y. Luo, M. Gelinsky, J. Chang, Y. Xiao, 3D-Printing of highly uniform $CaSiO_3$ ceramic scaffolds: preparation, characterization and *in vivo* osteogenesis, J. Mater. Chem. 22 (2012) 12288–12295.

[61] Z.X. Zhou, F. Buchanan, C. Mitchell, N. Dunne, Printability of calcium phosphate: calcium sulfate powders for the application of tissue engineered bone scaffolds using the 3D printing technique, Mater. Sci. Eng. C 38 (2014) 1–10.

[62] B. Dermeik, N. Travitzky, Laminated object manufacturing of ceramic-based materials, Adv. Eng. Mater. 22 (2020), 2000256.

[63] S. Attarilar, M. Ebrahimi, F. Djavanroodi, Y. Fu, L. Wang, J. Yang, 3D printing technologies in metallic implants: a thematic review on the techniques and procedures, Int. J. Bioprinting 7 (2020), 306-306.

[64] S. Yi, F. Liu, J. Zhang, S. Xiong, Study of the key technologies of LOM for functional metal parts, J. Mater. Process. Technol. 150 (2004) 175–181.

[65] I. Gibson, D.W. Rosen, B. Stucker, Sheet lamination processes, in: I. Gibson, D. W. Rosen, B. Stucker (Eds.), Additive Manufacturing Technologies: Rapid Prototyping to Direct Digital Manufacturing, Springer US, Boston, MA, 2010, pp. 223–252.

[66] J. Zhang, N. Amini, D.A.V. Morton, K.P. Hapgood, 3D printing with particles as feedstock materials, Adv. Powder Technol. 32 (2021) 3324–3345.

[67] M. Salmi, Additive manufacturing processes in medical applications, Materials 14 (2021) 191.

[68] C.K. Chua, K.F. Leong, J. An, Introduction to rapid prototyping of biomaterials, in: R. Narayan (Ed.), Rapid Prototyping of Biomaterials, second ed., Woodhead Publishing, 2020, pp. 1–15.

[69] Q. Hamid, J. Snyder, C. Wang, M. Timmer, J. Hammer, S. Guceri, W. Sun, Fabrication of three-dimensional scaffolds using precision extrusion deposition with an assisted cooling device, Biofabrication 3 (2011), 034109.

[70] M. Vaezi, G. Zhong, H. Kalami, S. Yang, Extrusion-based 3D printing technologies for 3D scaffold engineering, in: Y. Deng, J. Kuiper (Eds.), Functional 3D Tissue Engineering Scaffolds, Woodhead Publishing, 2018, pp. 235–254.

[71] M. Galati, P. Minetola, Analysis of density, roughness, and accuracy of the atomic diffusion additive manufacturing (ADAM) process for metal parts, Materials 12 (2019) 4122.

[72] L.E. Murr, Global trends in the development of complex, personalized, biomedical, surgical implant devices using 3D printing/additive manufacturing: a review, Med. Devices Sens. 3 (2020), e10126.

[73] W. Liu, S.F. Liu, L.Q. Wang, Surface modification of biomedical titanium alloy: micromorphology, microstructure evolution and biomedical applications, Coatings 9 (2019) 249.

[74] M. Cronskär, M. Bäckström, L.E. Rännar, Production of customized hip stem prostheses – a comparison between conventional machining and electron beam melting (EBM), Rapid Prototyp. J. 19 (2013) 365–372.

[75] A. Ataee, Y.C. Li, M. Brandt, C. Wen, Ultrahigh-strength titanium gyroid scaffolds manufactured by selective laser melting (SLM) for bone implant applications, Acta Mater. 158 (2018) 354–368.

[76] L. Thijs, F. Verhaeghe, T. Craeghs, J.V. Humbeeck, J.-P. Kruth, A study of the microstructural evolution during selective laser melting of Ti–6Al–4V, Acta Mater. 58 (2010) 3303–3312.

[77] X.C. Yan, R. Lupoi, H.J. Wu, W.Y. Ma, M. Liu, G. O'Donnel, S. Yin, Effect of hot isostatic pressing (hip) treatment on the compressive properties of Ti6Al4V lattice structure fabricated by selective laser melting, Mater. Lett. 255 (2019), 126537.

[78] A. Pandey, A. Awasthi, K.K. Saxena, Metallic implants with properties and latest production techniques: a review, Adv. Mater. Process. Technol. 6 (2020) 405–440.

[79] D. Zhang, S. Sun, D. Qiu, M.A. Gibson, M.S. Dargusch, M. Brandt, M. Qian, M. Easton, Metal alloys for fusion-based additive manufacturing, Adv. Eng. Mater. 20 (2018), 1700952.

[80] Q. Zhang, J. Chen, Z. Zhao, H. Tan, X. Lin, W. Huang, Microstructure and anisotropic tensile behavior of laser additive manufactured TC21 titanium alloy, Mater. Sci. Eng., A 673 (2016) 204–212.

[81] M.-W. Wu, P.-H. Lai, J.-K. Chen, Anisotropy in the impact toughness of selective laser melted Ti–6Al–4V alloy, Mater. Sci. Eng., A 650 (2016) 295–299.

[82] L.Y. Chen, J.C. Huang, C.H. Lin, C.T. Pan, S.Y. Chen, T.L. Yang, D.Y. Lin, H.K. Lin, J.S.C. Jang, Anisotropic response of Ti-6Al-4V alloy fabricated by 3D printing selective laser melting, Mater. Sci. Eng., A 682 (2017) 389–395.

[83] D.J. Newell, R.P. O'Hara, G.R. Cobb, A.N. Palazotto, M.M. Kirka, L.W. Burggraf, J.A. Hess, Mitigation of scan strategy effects and material anisotropy through supersolvus annealing in LPBF IN718, Mater. Sci. Eng., A 764 (2019), 138230.

[84] T. Mukherjee, J.S. Zuback, A. De, T. DebRoy, Printability of alloys for additive manufacturing, Sci. Rep. 6 (2016) 19717.

[85] M. Niinomi, Recent metallic materials for biomedical applications, Metall. Mater. Trans. 33 (2002) 477–486.

[86] L.C. Zhang, D. Klemm, J. Eckert, Y.L. Hao, T.B. Sercombe, Manufacture by selective laser melting and mechanical behavior of a biomedical Ti-24Nb-4Zr-8Sn alloy, Scripta Mater. 65 (2011) 21–24.

[87] H. Qian, T. Lei, P. Lei, Y. Hu, Additively manufactured tantalum implants for repairing bone defects: a systematic review, Tissue Eng. Part B 27 (2021) 166–180.

[88] T. Miyazaki, H.M. Kim, T. Kokubo, C. Ohtsuki, H. Kato, T. Nakamura, Mechanism of bonelike apatite formation on bioactive tantalum metal in a simulated body fluid, Biomaterials 23 (2002) 827–832.

[89] V.K. Balla, S. Bose, N.M. Davies, A. Bandyopadhyay, Tantalum-A bioactive metal for implants, JOM (J. Occup. Med.) 62 (2010) 61–64.

[90] V.K. Balla, S. Banerjee, S. Bose, A. Bandyopadhyay, Direct laser processing of a tantalum coating on titanium for bone replacement structures, Acta Biomater. 6 (2010) 2329–2334.

[91] H. Wang, K. Su, L. Su, P. Liang, P. Ji, C. Wang, Comparison of 3D-printed porous tantalum and titanium scaffolds on osteointegration and osteogenesis, Mater. Sci. Eng. C 104 (2019), 109908.

[92] S.L. Sing, W.Y. Yeong, F.E. Wiria, Selective laser melting of titanium alloy with 50 wt% tantalum: microstructure and mechanical properties, J. Alloys Compd. 660 (2016) 461–470.

[93] A. Francis, Y. Yang, S. Virtanen, A.R. Boccaccini, Iron and iron-based alloys for temporary cardiovascular applications, J. Mater. Sci. Mater. Med. 26 (2015) 138.

[94] R. Gorejova, L. Haverova, R. Orinakova, A. Orinak, M. Orinak, Recent advancements in Fe-based biodegradable materials for bone repair, J. Mater. Sci. 54 (2019) 1913–1947.

[95] K. Prasad, O. Bazaka, M. Chua, M. Rochford, L. Fedrick, J. Spoor, R. Symes, M. Tieppo, C. Collins, A. Cao, D. Markwell, K.K. Ostrikov, K. Bazaka, Metallic biomaterials: current challenges and opportunities, Materials 10 (2017) 884.

[96] L. Patnaik, S.R. Maity, S. Kumar, Status of nickel free stainless steel in biomedical field: a review of last 10 Years and what Else can Be done, Mater. Today Proc. 26 (2020) 638–643.

[97] G.X. Sun, A.W. Yu, S.C. Sun, C.T. Ji, Z.H. Jiang, J.S. Lian, Plastic deformation and fracture behaviour of high-nitrogen nickel-free austenitic stainless steel, Mater. Sci. Technol. 33 (2017) 1635–1644.

[98] J.M. Jeon, J.M. Park, J.-H. Yu, J.G. Kim, Y. Seong, S.H. Park, H.S. Kim, Effects of microstructure and internal defects on mechanical anisotropy and asymmetry of selective laser-melted 316L austenitic stainless steel, Mater. Sci. Eng., A 763 (2019), 138152.

[99] H. Yu, J. Yang, J. Yin, Z. Wang, X. Zeng, Comparison on mechanical anisotropies of selective laser melted Ti-6Al-4V alloy and 304 stainless steel, Mater. Sci. Eng., A 695 (2017) 92–100.

[100] Y. Kajima, A. Takaichi, N. Kittikundecha, T. Nakamoto, T. Kimura, N. Nomura, A. Kawasaki, T. Hanawa, H. Takahashi, N. Wakabayashi, Effect of heat-treatment temperature on microstructures and mechanical properties of Co-Cr-Mo alloys fabricated by selective laser melting, Mater. Sci. Eng., A 726 (2018) 21–31.

[101] A.J. Saldivar-Garcia, H.F. Lopez, Temperature effects on the lattice constants and crystal structure of a Co-27Cr-5Mo low-carbon alloy, Metall. Mater. Trans. 35a (2004) 2517–2523.
[102] E.C. Kim, M.K. Kim, R. Leesungbok, S.W. Lee, S.J. Ahn, Co-Cr dental alloys induces cytotoxicity and inflammatory responses *via* activation of NRF2/antioxidant signaling pathways in human gingival fibroblasts and osteoblasts, Dent. Mater. 32 (2016) 1394–1405.
[103] A. Chiba, K. Kumagai, N. Nomura, S. Miyakawa, Pin-on-Disk wear behavior in a like-on-like configuration in a biological environment of high carbon cast and low carbon forged Co-29Cr-6Mo alloys, Acta Mater. 55 (2007) 1309–1318.
[104] X.Z. Xin, N. Xiang, J. Chen, B. Wei, *In vitro* biocompatibility of Co-Cr alloy fabricated by selective laser melting or traditional casting techniques, Mater. Lett. 88 (2012) 101–103.
[105] A. Cutolo, B. Neirinck, K. Lietaert, C. de Formanoir, B. Van Hooreweder, Influence of layer thickness and post-process treatments on the fatigue properties of CoCr scaffolds produced by laser powder bed fusion, Addit. Manuf. 23 (2018) 498–504.
[106] R. Karunakaran, S. Ortgies, A. Tamayol, F. Bobaru, M.P. Sealy, Additive manufacturing of magnesium alloys, Bioact. Mater. 5 (2020) 44–54.
[107] J. Ni, H. Ling, S. Zhang, Z. Wang, Z. Peng, C. Benyshek, R. Zan, A.K. Miri, Z. Li, X. Zhang, J. Lee, K.J. Lee, H.J. Kim, P. Tebon, T. Hoffman, M.R. Dokmeci, N. Ashammakhi, X. Li, A. Khademhosseini, Three-dimensional printing of metals for biomedical applications, Mater. Today Bio 3 (2019) 100024.
[108] C.X. Zhang, J.J. Lin, H.N. Liu, Magnesium-based biodegradable materials for biomedical applications, MRS Adv 3 (2018) 2359–2364.
[109] Y. Li, J. Zhou, P. Pavanram, M.A. Leeflang, L.I. Fockaert, B. Pouran, N. Tumer, K. U. Schroder, J.M.C. Mol, H. Weinans, H. Jahr, A.A. Zadpoor, Additively manufactured biodegradable porous magnesium, Acta Biomater. 67 (2018) 378–392.
[110] N.T. Kirkland, N. Birbilis, Magnesium Biomaterials: Design, Testing, and Best Practice, Springer, 2014.
[111] B. Xie, M.-C. Zhao, R. Xu, Y.-C. Zhao, D. Yin, C. Gao, A. Atrens, Biodegradation, antibacterial performance, and cytocompatibility of a novel ZK30-Cu-Mn biomedical alloy produced by selective laser melting, Int. J. Bioprinting 7 (2020), 300-300.
[112] H. Hornberger, S. Virtanen, A.R. Boccaccini, Biomedical coatings on magnesium alloys - a review, Acta Biomater. 8 (2012) 2442–2455.
[113] V. Manakari, G. Parande, M. Gupta, Selective laser melting of magnesium and magnesium alloy powders: a review, Metals 7 (2017) 2.
[114] A. Ferrández-Montero, M. Lieblich, R. Benavente, J.L. González-Carrasco, B. Ferrari, Study of the matrix-filler interface in PLA/Mg composites manufactured by material extrusion using a colloidal feedstock, Addit. Manuf. 33 (2020), 101142.
[115] M. Shahinpoor, Fundamentals of smart materials, Royal Society of Chemistry, 2020.
[116] I.Z. Awan, A.Q. Khan, Fascinating shape memory alloys, J. Chem. Soc. Pakistan 40 (2018) 1–23.
[117] Y. Zhang, S. Attarilar, L. Wang, W. Lu, J. Yang, Y. Fu, A review on design and mechanical properties of additively manufactured NiTi implants for orthopedic applications, Int. J. Bioprinting 7 (2021), 340-340.
[118] C. Lexcellent, Shape-Memory Alloys Handbook, John Wiley & Sons, 2013.
[119] E. Farber, J.N. Zhu, A. Popovich, V. Popovich, A review of NiTi shape memory alloy as a smart material produced by additive manufacturing, Mater. Today Proc. 30 (2020) 761–767.
[120] J. Ma, B. Franco, G. Tapia, K. Karayagiz, L. Johnson, J. Liu, R. Arroyave, I. Karaman, A. Elwany, Spatial control of functional response in 4D-printed active metallic structures, Sci. Rep. 7 (2017) 46707.
[121] S.O. Omid, Z. Goudarzi, L.M. Kangarshahi, A. Mokhtarzade, F. Bahrami, Self-expanding stents based on shape memory alloys and shape memory polymers, J. Compos. Compd. 2 (2020) 92–98.
[122] N.A. Obaisi, M.T. Galang-Boquiren, C.A. Evans, T.G. Tsay, G. Viana, D. Berzins, S. Megremis, Comparison of the transformation temperatures of heat-activated nickel-titanium orthodontic archwires by two different techniques, Dent. Mater. 32 (2016) 879–888.
[123] W.A. Brantley, Evolution, clinical applications, and prospects of nickel-titanium alloys for orthodontic purposes, J. World Fed. Orthod. 9 (2020) S19–S26.
[124] M. Mirjalili, M. Momeni, N. Ebrahimi, M.H. Moayed, Comparative study on corrosion behaviour of nitinol and stainless steel orthodontic wires in simulated saliva solution in presence of fluoride ions, Mater. Sci. Eng. C 33 (2013) 2084–2093.
[125] A. Wadood, Brief overview on nitinol as biomaterial, Adv. Mater. Sci. Eng. (2016), 2016.
[126] C. Constant, S. Nichols, E. Wagnac, Y. Petit, A. Desrochers, V. Brailovski, Biocompatibility and mechanical stability of nitinol as biomaterial for intra-articular prosthetic devices, Materialia 9 (2020), 100567.
[127] H. Holman, M.N. Kavarana, T.K. Rajab, Smart materials in cardiovascular implants: shape memory alloys and shape memory polymers, Artif. Organs 45 (2021) 454–463.
[128] A. Vaicelyte, C. Janssen, M. Le Borgne, B. Grosgogeat, Cobalt–chromium dental alloys: metal exposures, toxicological risks, CMR classification, and EU regulatory framework, Crystals 10 (2020) 1151.
[129] J. Dong, N. Tümer, N.E. Putra, J. Zhu, Y. Li, M.A. Leeflang, P. Taheri, L.E. Fratila-Apachitei, J.M.C. Mol, A.A. Zadpoor, J. Zhou, Extrusion-based 3D printed magnesium scaffolds with multifunctional MgF_2 and MgF_2–CaP coatings, Biomater. Sci. 9 (2021) 7159–7182.
[130] H. Kabir, K. Munir, C. Wen, Y. Li, Recent research and progress of biodegradable zinc alloys and composites for biomedical applications: biomechanical and biocorrosion perspectives, Bioact. Mater. 6 (2021) 836–879.
[131] J. Kadkhodapour, H. Montazerian, M. Samadi, S. Schmauder, A. Abouei Mehrizi, Plastic deformation and compressive mechanical properties of hollow sphere aluminum foams produced by space holder technique, Mater. Des. 83 (2015) 352–362.
[132] O. Sigmund, K. Maute, Topology optimization approaches-A comparative review, Struct. Multidiscip. Optim. 48 (2013) 1031–1055.
[133] I. Goda, J.F. Ganghoffer, S. Czarnecki, R. Czubacki, P. Wawruch, Topology optimization of bone using cubic material design and evolutionary methods based on internal remodeling, Mech. Res. Commun. 95 (2019) 52–60.
[134] J. Feng, B. Liu, Z. Lin, J. Fu, Isotropic porous structure design methods based on triply periodic minimal surfaces, Mater. Des. 210 (2021), 110050.
[135] J. Feng, B. Liu, Z. Lin, J. Fu, Isotropic octet-truss lattice structure design and anisotropy control strategies for implant application, Mater. Des. 203 (2021), 109595.
[136] M. Zhou, G.I.N. Rozvany, The COC algorithm, Part II: topological, geometrical and generalized shape optimization, Comput. Methods Appl. Mech. Eng. 89 (1991) 309–336.
[137] J. Park, A. Sutradhar, J.J. Shah, G.H. Paulino, Design of complex bone internal structure using topology optimization with perimeter control, Comput. Biol. Med. 94 (2018) 74–84.
[138] A. Carnicero, A. Peláez, A. Restoy-Lozano, I. Jacquott, R. Perera, Improvement of an additively manufactured subperiosteal implant structure design by finite elements based topological optimization, Sci. Rep. 11 (2021), 15390.
[139] H. Kang, J.P. Long, G.D. Urbiel Goldner, S.A. Goldstein, S.J. Hollister, A paradigm for the development and evaluation of novel implant topologies for bone fixation: implant design and fabrication, J. Biomech. 45 (2012) 2241–2247.
[140] H. Wang, Y. Wan, Q. Li, Y. Xia, X. Liu, Z. Liu, X. Li, Porous fusion cage design *via* integrated global-local topology optimization and biomechanical analysis of performance, J. Mech. Behav. Biomed. Mater. 112 (2020), 103982.
[141] J.J. Lang, M. Bastian, P. Foehr, M. Seebach, J. Weitz, C. von Deimling, B. J. Schwaiger, C.M. Micheler, N.J. Wilhelm, C.U. Grosse, M. Kesting, R. Burgkart, Improving mandibular reconstruction by using topology optimization, patient specific design and additive manufacturing?—a biomechanical comparison against miniplates on human specimen, PLoS One 16 (2021), e0253002.
[142] A.A. Al-Tamimi, B.Y. Huang, C. Vyas, M. Hernandez, C. Peach, P. Bartolo, Topology optimised metallic bone plates produced by electron beam melting: a mechanical and biological study, Int. J. Adv. Manuf. Technol. 104 (2019) 195–210.
[143] J. Wu, N. Aage, R. Westermann, O. Sigmund, Infill optimization for additive manufacturing-approaching bone-like porous structures, IEEE Trans. Visual. Comput. Graph. 24 (2018) 1127–1140.
[144] Y. He, D. Burkhalter, D. Durocher, J.M. Gilbert, in: Solid-Lattice Hip Prosthesis Design: Applying Topology and Lattice Optimization to Reduce Stress Shielding from Hip Implants, 2018 Design of Medical Devices Conference, 2018.
[145] K.J. Cheng, Y.F. Liu, R. Wang, J.X. Zhang, X.F. Jiang, X.T. Dong, X. Xu, Topological optimization of 3D printed bone analog with pekk for surgical mandibular reconstruction, J. Mech. Behav. Biomed. Mater. 107 (2020), 103758.
[146] K.J. Cheng, Y.F. Liu, C.Y. Yao, W.Q. Zhao, X. Xu, A personalized mandibular implant with supporting and porous structures designed with topology optimization - a case study of canine, Rapid Prototyp. J. 25 (2019) 417–426.
[147] Z.D. Zhang, O. Ibhadode, U. Ali, C.F. Dibia, P. Rahnama, A. Bonakdar, E. Toyserkani, Topology optimization parallel-computing framework based on the inherent strain method for support structure design in laser powder-bed fusion additive manufacturing, Int. J. Mech. Mater. Des. 16 (2020) 897–923.
[148] O. Ibhadode, Z.D. Zhang, P. Rahnama, A. Bonakdar, E. Toyserkani, Topology optimization of structures under design-dependent pressure loads by a boundary identification-load evolution (bile) model, Struct. Multidiscip. Optim. 62 (2020) 1865–1883.
[149] L. Jiang, S. Chen, C. Sadasivan, X. Jiao, in: Structural Topology Optimization for Generative Design of Personalized Aneurysm Implants: Design, Additive Manufacturing, and Experimental Validation, 2017 IEEE Healthcare Innovations and Point of Care Technologies (HI-POCT), 2017, pp. 9–13.
[150] L.X. Guo, J.Y. Yin, Finite element analysis and design of an interspinous device using topology optimization, Med. Biol. Eng. Comput. 57 (2019) 89–98.
[151] H.C. Liu, J.S. Jiang, C.L. Lin, Biomechanical investigation of a novel hybrid dorsal double plating for distal radius fractures by integrating topology optimization and finite element analysis, Injury 51 (2020) 1271–1280.
[152] M.A. Al-Ali, M.A. Al-Ali, A. Takezawa, M. Kitamura, Topology optimization and fatigue analysis of temporomandibular joint prosthesis, World J. Mech. (2017) 323–339, 07.
[153] J.D. Deaton, R.V. Grandhi, Stress-based design of thermal structures *via* topology optimization, Struct. Multidiscip. Optim. 53 (2016) 253–270.
[154] C.A. Gómez Pérez, H.I. Medellín-Castillo, R. Espinosa-Castañeda, Computer Assisted Design and Structural Topology Optimization of Customized Craniofacial Implants, Biomedical and Biotechnology Engineering, 2017.
[155] A. Sutradhar, J. Park, D. Carrau, M.J. Miller, Experimental validation of 3D printed patient-specific implants using digital image correlation and finite element analysis, Comput. Biol. Med. 52 (2014) 8–17.
[156] N. Dai, J.F. Zhu, M. Zhang, L.Y. Meng, X.L. Yu, Y.H. Zhang, B.Y. Liu, S.L. Zhang, Design of a maxillofacial prosthesis based on topology optimization, J. Mech. Med. Biol. 18 (2018), 1850024.

[157] X. Deng, Y. Wang, J. Yan, T. Liu, S. Wang, Topology optimization of total femur structure: application of parameterized level set method under geometric constraints, J. Mech. Des. 138 (2016), 011402.
[158] C. Pan, Y.F. Han, J.P. Lu, Design and optimization of lattice structures: a review, Appl. Sci. 10 (2020), 6374.
[159] F. Tamburrino, S. Graziosi, M. Bordegoni, The design process of additively manufactured mesoscale lattice structures: a review, J. Comput. Inf. Sci. Eng. 18 (2018), 040801.
[160] W. Tao, M.C. Leu, in: Design of Lattice Structure for Additive Manufacturing, 2016 International Symposium on Flexible Automation (ISFA), IEEE, 2016, pp. 325–332.
[161] K.F. Leong, C.M. Cheah, C.K. Chua, Solid freeform fabrication of three-dimensional scaffolds for engineering replacement tissues and organs, Biomaterials 24 (2003) 2363–2378.
[162] H. Lo, M.S. Ponticiello, K.W. Leong, Fabrication of controlled release biodegradable foams by phase separation, Tissue Eng. 1 (1995) 15–28.
[163] A.G. Mikos, G. Sarakinos, S.M. Leite, J.P. Vacant, R. Langer, Laminated three-dimensional biodegradable foams for use in tissue engineering, Biomaterials 14 (1993) 323–330.
[164] H. Montazerian, M. Zhianmanesh, E. Davoodi, A.S. Milani, M. Hoorfar, Longitudinal and radial permeability analysis of additively manufactured porous scaffolds: effect of pore shape and porosity, Mater. Des. 122 (2017) 146–156.
[165] S. Ghouse, S. Babu, K. Nai, P.A. Hooper, J.R.T. Jeffers, The influence of laser parameters, scanning strategies and material on the fatigue strength of a stochastic porous structure, Addit. Manuf. 22 (2018) 290–301.
[166] M. Fantini, M. Curto, Interactive design and manufacturing of a voronoi-based biomimetic bone scaffold for morphological characterization, Int. J. Interact. Des. 12 (2018) 585–596.
[167] H. Chen, Y. Liu, C. Wang, A. Zhang, B. Chen, Q. Han, J. Wang, Design and properties of biomimetic irregular scaffolds for bone tissue engineering, Comput. Biol. Med. 130 (2021), 104241.
[168] H. Chen, Q. Han, C. Wang, Y. Liu, B. Chen, J. Wang, Porous scaffold design for additive manufacturing in orthopedics: a review, Front. Bioeng. Biotechnol. 8 (2020) 609.
[169] H.X. Liang, Y.W. Yang, D.Q. Xie, L. Li, N. Mao, C.J. Wang, Z.J. Tian, Q. Jiang, L. D. Shen, Trabecular-like Ti-6Al-4V scaffolds for orthopedic: fabrication by selective laser melting and *in vitro* biocompatibility, J. Mater. Sci. Technol. 35 (2019) 1284–1297.
[170] T. Liu, S. Guessasma, J.H. Zhu, W.H. Zhang, Designing cellular structures for additive manufacturing using Voronoi-Monte Carlo approach, Polymers 11 (2019) 1158.
[171] G. Savio, S. Rosso, R. Meneghello, G. Concheri, Geometric modeling of cellular materials for additive manufacturing in biomedical field: a review, Appl. Bionics Biomechanics 2018 (2018), 1654782.
[172] G. Wang, L. Shen, J. Zhao, H. Liang, D. Xie, Z. Tian, C. Wang, Design and compressive behavior of controllable irregular porous scaffolds: based on voronoi-tessellation and for additive manufacturing, ACS Biomater. Sci. Eng. 4 (2018) 719–727.
[173] Y. Du, H.X. Liang, D.Q. Xie, N. Mao, J.F. Zhao, Z.J. Tian, C.J. Wang, L.D. Shen, Design and statistical analysis of irregular porous scaffolds for orthopedic reconstruction based on Voronoi tessellation and fabricated *via* selective laser melting (SLM), Mater. Chem. Phys. 239 (2020), 121968.
[174] H.Y. Lei, J.R. Li, Z.J. Xu, Q.H. Wang, Parametric design of voronoi-based lattice porous structures, Mater. Des. 191 (2020), 108607.
[175] S. Ghouse, N. Reznikov, O.R. Boughton, S. Babu, K.C. Geoffrey Ng, G. Blunn, J. P. Cobb, M.M. Stevens, J.R.T. Jeffers, The design and *in vivo* testing of a locally stiffness-matched porous scaffold, Appl. Mater. Today 15 (2019) 377–388.
[176] M.M. Barak, M.A. Black, A novel use of 3D printing model demonstrates the effects of deteriorated trabecular bone structure on bone stiffness and strength, J. Mech. Behav. Biomed. Mater. 78 (2018) 455–464.
[177] R.M. Gorguluarslan, U.N. Gandhi, R. Mandapati, S.-K. Choi, Design and fabrication of periodic lattice-based cellular structures, Comput. Aided Des. Appl. 13 (2016) 50–62.
[178] T.A. Schaedler, W.B. Carter, Architected cellular materials, Annu. Rev. Mater. Res. 46 (2016) 187–210.
[179] M. Helou, S. Kara, Design, analysis and manufacturing of lattice structures: an overview, Int. J. Comput. Integrated Manuf. 31 (2018) 243–261.
[180] A. Bandyopadhyay, Y. Zhang, S. Bose, Recent developments in metal additive manufacturing, Curr. Opin. Chem. Eng. 28 (2020) 96–104.
[181] M. McMillan, M. Jurg, M. Leary, M. Brandt, Programmatic lattice generation for additive manufacture, in: Proceedings of the 1st International Design Technology Conference, Destech2015, 2015, pp. 178–184.
[182] N.A. Meisel, C.B. Williams, A. Druschitz, Lightweight metal cellular structures *via* indirect 3D printing and casting, in: Proceedings of the International Solid Freeform Fabrication Symposium, 2012, pp. 162–176.
[183] C. Lu, M.X. Qi, S. Islam, P. Chen, S.S. Gao, Y.R. Xu, X.D. Yang, Mechanical performance of 3D-printing plastic honeycomb sandwich structure, Int. J. Precis. Eng. Manuf. 5 (2018) 47–54.
[184] Y. Du, H.X. Liang, D.Q. Xie, N. Mao, J.F. Zhao, Z.J. Tian, C.J. Wang, L.D. Shen, Finite element analysis of mechanical behavior, permeability of irregular porous scaffolds and lattice-based porous scaffolds, Mater. Res. Express 6 (2019), 105407.
[185] H.M.A. Kolken, C.P. de Jonge, T. van der Sloten, A.F. Garcia, B. Pouran, K. Willemsen, H. Weinans, A.A. Zadpoor, Additively manufactured space-filling meta-implants, Acta Biomater. 125 (2021) 345–357.
[186] J. Kadkhodapour, H. Montazerian, A. Darabi, A.P. Anaraki, S.M. Ahmadi, A. A. Zadpoor, S. Schmauder, Failure mechanisms of additively manufactured porous biomaterials: effects of porosity and type of unit cell, J. Mech. Behav. Biomed. Mater. 50 (2015) 180–191.
[187] H.M.A. Kolken, S. Janbaz, S.M.A. Leeflang, K. Lietaert, H.H. Weinans, A. A. Zadpoor, Rationally designed meta-implants: a combination of auxetic and conventional meta-biomaterials, Mater. Horiz. 5 (2018) 28–35.
[188] P.F. Egan, V.C. Gonella, M. Engensperger, S.J. Ferguson, K. Shea, Computationally designed lattices with tuned properties for tissue engineering using 3D printing, PLoS One 12 (2017), e0182902.
[189] Y. Yang, G. Wang, H. Liang, C. Gao, S. Peng, L. Shen, C. Shuai, Additive manufacturing of bone scaffolds, Int. J. Bioprinting 5 (2019) 148.
[190] J. Shi, L. Zhu, L. Li, Z. Li, J. Yang, X. Wang, A TPMS-based method for modeling porous scaffolds for bionic bone tissue engineering, Sci. Rep. 8 (2018) 7395.
[191] E. Davoodi, H. Montazerian, R. Haghniaz, A. Rashidi, S. Ahadian, A. Sheikhi, J. Chen, A. Khademhosseini, A.S. Milani, M. Hoorfar, E. Toyserkani, 3D-Printed ultra-robust surface-doped porous silicone sensors for wearable biomonitoring, ACS Nano 14 (2020) 1520–1532.
[192] E. Davoodi, H. Montazerian, A. Khademhosseini, E. Toyserkani, Sacrificial 3D printing of shrinkable silicone Elastomers for enhanced feature resolution in flexible tissue scaffolds, Acta Biomater. 117 (2020) 261–272.
[193] M.R. Mansouri, H. Montazerian, S. Schmauder, J. Kadkhodapour, 3D-Printed multimaterial composites tailored for compliancy and strain recovery, Compos. Struct. 184 (2018) 11–17.
[194] O. Al-Ketan, D.W. Lee, R. Rowshan, R.K. Abu Al-Rub, Functionally graded and multi-morphology sheet TPMS lattices: design, manufacturing, and mechanical properties, J. Mech. Behav. Biomed. Mater. 102 (2020), 103520.
[195] H. Montazerian, M.G.A. Mohamed, M.M. Montazeri, S. Kheiri, A.S. Milani, K. Kim, M. Hoorfar, Permeability and mechanical properties of gradient porous PDMS scaffolds fabricated by 3D-printed sacrificial templates designed with minimal surfaces, Acta Biomater. 96 (2019) 149–160.
[196] S. Vijayavenkataraman, L. Zhang, S. Zhang, J.Y.H. Fuh, W. Feng, Triply periodic minimal surfaces sheet scaffolds for tissue engineering applications: an optimization approach toward biomimetic scaffold design, ACS Appl. Bio Mater. 1 (2018) 259–269.
[197] J. Kadkhodapour, H. Montazerian, S. Raeisi, Investigating internal architecture effect in plastic deformation and failure for TPMS-based scaffolds using simulation methods and experimental procedure, Mater. Sci. Eng. C 43 (2014) 587–597.
[198] J. Kadkhodapour, H. Montazerian, A.C. Darabi, A. Zargarian, S. Schmauder, The relationships between deformation mechanisms and mechanical properties of additively manufactured porous biomaterials, J. Mech. Behav. Biomed. Mater. 70 (2017) 28–42.
[199] L. Yang, C.Z. Yan, C.J. Han, P. Chen, S.F. Yang, Y.S. Shi, Mechanical response of a triply periodic minimal surface cellular structures manufactured by selective laser melting, Int. J. Mech. Sci. 148 (2018) 149–157.
[200] R. Ambu, A.E. Morabito, Porous scaffold design based on minimal surfaces: development and assessment of variable architectures, Symmetry 10 (2018) 361.
[201] O. Al-Ketan, R. Rezgui, R. Rowshan, H. Du, N.X. Fang, R.K. Abu Al-Rub, Microarchitected stretching-dominated mechanical metamaterials with minimal surface topologies, Adv. Eng. Mater. 20 (2018), 1800029.
[202] D.W. Abueidda, M. Bakir, R.K. Abu Al-Rub, J.S. Bergstrom, N.A. Sobh, I. Jasiuk, Mechanical properties of 3D printed polymeric cellular materials with triply periodic minimal surface architectures, Mater. Des. 122 (2017) 255–267.
[203] D.W. Abueidda, M. Elhebeary, C.S. Shiang, S.Y. Pang, R.K. Abu Al-Rub, I. M. Jasiuk, Mechanical properties of 3D printed polymeric gyroid cellular structures: experimental and finite element study, Mater. Des. 165 (2019), 107597.
[204] S.C. Han, J.W. Lee, K. Kang, A new type of low density material: shellular, Adv. Mater. 27 (2015) 5506–5511.
[205] M.G. Lee, J.W. Lee, S.C. Han, K. Kang, Mechanical analyses of "shellular", an ultralow-density material, Acta Mater. 103 (2016) 595–607.
[206] D. Ali, M. Ozalp, S.B.G. Blanquer, S. Onel, Permeability and fluid flow-induced wall shear stress in bone scaffolds with TPMS and lattice architectures: a CFD analysis, Eur. J. Mech. B Fluid 79 (2020) 376–385.
[207] S.X. Yu, J.X. Sun, J.M. Bai, Investigation of functionally graded tpms structures fabricated by additive manufacturing, Mater. Des. 182 (2019), 108021.
[208] E. Davoodi, H. Montazerian, R. Esmaeilizadeh, A.C. Darabi, A. Rashidi, J. Kadkhodapour, H. Jahed, M. Hoorfar, A.S. Milani, P.S. Weiss, A. Khademhosseini, E. Toyserkani, Additively manufactured gradient porous Ti-6Al-4V hip replacement implants embedded with cell-laden gelatin methacryloyl hydrogels, ACS Appl. Mater. Interfaces 13 (2021) 22110–22123.
[209] H. Montazerian, E. Davoodi, M. Asadi-Eydivand, J. Kadkhodapour, M. Solati-Hashjin, Porous scaffold internal architecture design based on minimal surfaces: a compromise between permeability and elastic properties, Mater. Des. 126 (2017) 98–114.
[210] C. Han, Y. Li, Q. Wang, S. Wen, Q. Wei, C. Yan, L. Hao, J. Liu, Y. Shi, Continuous functionally graded porous titanium scaffolds manufactured by selective laser melting for bone implants, J. Mech. Behav. Biomed. Mater. 80 (2018) 119–127.
[211] X.G. Miao, D. Sun, Graded/gradient porous biomaterials, Materials 3 (2010) 26–47.
[212] M. Afshar, A. Pourkamali Anaraki, H. Montazerian, Compressive characteristics of radially graded porosity scaffolds architectured with minimal surfaces, Mater. Sci. Eng. C 92 (2018) 254–267.

[213] D.S.J. Al-Saedi, S.H. Masood, M. Faizan-Ur-Rab, A. Alomarah, P. Ponnusamy, Mechanical properties and energy absorption capability of functionally graded F2BCC lattice fabricated by SLM, Mater. Des. 144 (2018) 32–44.
[214] S.Y. Choy, C.N. Sun, K.F. Leong, J. Wei, Compressive properties of functionally graded lattice structures manufactured by selective laser melting, Mater. Des. 131 (2017) 112–120.
[215] F. Liu, Z.F. Mao, P. Zhang, D.Z. Zhang, J.J. Jiang, Z.B. Ma, Functionally graded porous scaffolds in multiple patterns: new design method, physical and mechanical properties, Mater. Des. 160 (2018) 849–860.
[216] L. Li, J. Shi, K. Zhang, L. Yang, F. Yu, L. Zhu, H. Liang, X. Wang, Q. Jiang, Early osteointegration evaluation of porous Ti6Al4V scaffolds designed based on triply periodic minimal surface models, J. Orthop. Translat. 19 (2019) 94–105.
[217] M. Afshar, A.P. Anaraki, H. Montazerian, J. Kadkhodapour, Additive manufacturing and mechanical characterization of graded porosity scaffolds designed based on triply periodic minimal surface architectures, J. Mech. Behav. Biomed. Mater. 62 (2016) 481–494.
[218] X. Li, J. Ding, J. Wang, X. Zhuang, X. Chen, Biomimetic biphasic scaffolds for osteochondral defect repair, Regener. Biomater. 2 (2015) 221–228.
[219] E. Garner, H.M.A. Kolken, C.C.L. Wang, A.A. Zadpoor, J. Wu, Compatibility in microstructural optimization for additive manufacturing, Addit. Manuf. 26 (2019) 65–75.
[220] A. Berner, M.A. Woodruff, C.X. Lam, M.T. Arafat, S. Saifzadeh, R. Steck, J. Ren, M. Nerlich, A.K. Ekaputra, I. Gibson, D.W. Hutmacher, Effects of scaffold architecture on cranial bone healing, Int. J. Oral Maxillofac. Surg. 43 (2014) 506–513.
[221] C.M. Bidan, K.P. Kommareddy, M. Rumpler, P. Kollmannsberger, P. Fratzl, J.W. C. Dunlop, Geometry as a factor for tissue growth: towards shape optimization of tissue engineering scaffolds, Adv. Healthcare Mater. 2 (2013) 186–194.
[222] A. Di Luca, I. Lorenzo-Moldero, C. Mota, A. Lepedda, D. Auhl, C. Van Blitterswijk, L. Moroni, Tuning cell differentiation into a 3D scaffold presenting a pore shape gradient for osteochondral regeneration, Adv. Healthcare Mater. 5 (2016) 1753–1763.
[223] P.L. Lewis, R.M. Green, R.N. Shah, 3D-Printed gelatin scaffolds of differing pore geometry modulate hepatocyte function and gene expression, Acta Biomater. 69 (2018) 63–70.
[224] M. Kurita, T. Araoka, T. Hishida, D.D. O'Keefe, Y. Takahashi, A. Sakamoto, M. Sakurai, K. Suzuki, J. Wu, M. Yamamoto, R. Hernandez-Benitez, A. Ocampo, P. Reddy, M.N. Shokhirev, P. Magistretti, E. Nunez Delicado, H. Eto, K. Harii, J. C. Izpisua Belmonte, *In vivo* reprogramming of Wound-resident cells generates skin Epithelial tissue, Nature 561 (2018) 243–247.
[225] S. Baiguera, C. Del Gaudio, P. Di Nardo, V. Manzari, F. Carotenuto, L. Teodori, 3D printing decellularized extracellular matrix to design biomimetic scaffolds for skeletal muscle tissue engineering, BioMed Res. Int. 2020 (2020) 2689701.
[226] C.F. Guimarães, L. Gasperini, A.P. Marques, R.L. Reis, The stiffness of living tissues and its implications for tissue engineering, Nat. Rev. Mater. 5 (2020) 351–370.
[227] T.T. Xia, W.Q. Liu, L. Yang, A review of gradient stiffness hydrogels used in tissue engineering and regenerative medicine, J. Biomed. Mater. Res. 105 (2017) 1799–1812.
[228] L.M. Cross, K. Shah, S. Palani, C.W. Peak, A.K. Gaharwar, Gradient nanocomposite hydrogels for interface tissue engineering, Nanomedicine 14 (2018) 2465–2474.
[229] B. Zhang, J. Huang, R.J. Narayan, Gradient scaffolds for osteochondral tissue engineering and regeneration, J. Mater. Chem. B 8 (2020) 8149–8170.
[230] R. Sinha, M. Camara-Torres, P. Scopece, E. Verga Falzacappa, A. Patelli, L. Moroni, C. Mota, A hybrid additive manufacturing platform to create bulk and surface composition gradients on scaffolds for tissue regeneration, Nat. Commun. 12 (2021) 500.
[231] L. Li, J. Wang, P. Lin, H. Liu, Microstructure and mechanical properties of functionally graded TiCp/Ti6Al4V composite fabricated by laser melting deposition, Ceram. Int. 43 (2017) 16638–16651.
[232] Y.N. Zhang, A. Bandyopadhyay, Direct fabrication of compositionally graded Ti-Al2-O3 multi-material structures using laser engineered net shaping, Addit. Manuf. 21 (2018) 104–111.
[233] T. Gualtieri, A. Bandyopadhyay, Additive manufacturing of compositionally gradient metal-ceramic structures: stainless steel to vanadium carbide, Mater. Des. 139 (2018) 419–428.
[234] L. Liu, P. Kamm, F. Garcia-Moreno, J. Banhart, D. Pasini, Elastic and failure response of imperfect three-dimensional metallic lattices: the role of geometric defects induced by selective laser melting, J. Mech. Phys. Solid. 107 (2017) 160–184.
[235] T. Maconachie, M. Leary, B. Lozanovski, X.Z. Zhang, M. Qian, O. Faruque, M. Brandt, SLM lattice structures: properties, performance, applications and challenges, Mater. Des. 183 (2019), 108137.
[236] X.Z. Zhang, M. Leary, H.P. Tang, T. Song, M. Qian, Selective electron beam manufactured Ti-6Al-4V lattice structures for orthopedic implant applications: current status and outstanding challenges, Curr. Opin. Solid State Mater. Sci. 22 (2018) 75–99.
[237] D. Melancon, Z.S. Bagheri, R.B. Johnston, L. Liu, M. Tanzer, D. Pasini, Mechanical characterization of structurally porous biomaterials built *via* additive manufacturing: Experiments, predictive models, and design maps for load-bearing bone replacement implants, Acta Biomater. 63 (2017) 350–368.
[238] I. Echeta, X. Feng, B. Dutton, R. Leach, S. Piano, Review of defects in lattice structures manufactured by powder bed fusion, Int. J. Adv. Manuf. Technol. 106 (2020) 2649–2668.
[239] Z.S. Bagheri, D. Melancon, L. Liu, R.B. Johnston, D. Pasini, Compensation strategy to reduce geometry and mechanics mismatches in porous biomaterials built with selective laser melting, J. Mech. Behav. Biomed. Mater. 70 (2017) 17–27.
[240] M. Dallago, B. Winiarski, F. Zanini, S. Carmignato, M. Benedetti, On the effect of geometrical imperfections and defects on the fatigue strength of cellular lattice structures additively manufactured *via* selective laser melting, Int. J. Fatig. 124 (2019) 348–360.
[241] S. Arabnejad, R.B. Johnston, J.A. Pura, B. Singh, M. Tanzer, D. Pasini, High-strength porous biomaterials for bone replacement: a strategy to assess the interplay between cell morphology, mechanical properties, bone ingrowth and manufacturing constraints, Acta Biomater. 30 (2016) 345–356.
[242] Z. Alomar, F. Concli, A review of the selective laser melting lattice structures and their numerical models, Adv. Eng. Mater. 22 (2020), 2000611.
[243] A. El Elmi, D. Melancon, M. Asgari, L. Liu, D. Pasini, Experimental and numerical investigation of selective laser melting–induced defects in Ti–6Al–4V octet truss lattice material: the role of material microstructure and morphological variations, J. Mater. Res. 35 (2020) 1900–1912.
[244] E. Yang, M. Leary, B. Lozanovski, D. Downing, M. Mazur, A. Sarker, A. Khorasani, A. Jones, T. Maconachie, S. Bateman, M. Easton, M. Qian, P. Choong, M. Brandt, Effect of geometry on the mechanical properties of Ti-6Al-4V gyroid structures fabricated *via* SLM: a numerical study, Mater. Des. 184 (2019), 108165.
[245] D. Mahmoud, K.S. Al-Rubaie, M.A. Elbestawi, The influence of selective laser melting defects on the fatigue properties of Ti6Al4V porosity graded gyroids for bone implants, Int. J. Mech. Sci. 193 (2021), 106180.
[246] A. Sola, A. Nouri, Microstructural porosity in additive manufacturing: the Formation and detection of pores in metal parts fabricated by powder bed fusion, J. Adv. Manuf. Process. 1 (2019), e10021.
[247] A. du Plessis, I. Yadroitsava, I. Yadroitsev, Effects of defects on mechanical properties in metal additive manufacturing: a review focusing on X-ray tomography insights, Mater. Des. 187 (2020), 108385.
[248] E. Hernández-Nava, S. Tammas-Williams, C. Smith, F. Leonard, P.J. Withers, I. Todd, R. Goodall, X-ray tomography characterisation of lattice structures processed by selective electron beam melting, Metals 7 (2017) 300.
[249] L.C. Zhang, Y.J. Liu, S.J. Li, Y.L. Hao, Additive manufacturing of titanium alloys by electron beam melting: a review, Adv. Eng. Mater. 20 (2018), 1700842.
[250] C.Z. Yan, L. Hao, A. Hussein, D. Raymont, Evaluations of cellular lattice structures manufactured using selective laser melting, Int. J. Mach. Tool Manufact. 62 (2012) 32–38.
[251] V.I. Perumal, A.R. Najafi, A. Kontsos, A novel digital design approach for metal additive manufacturing to address local thermal effects, Design 4 (2020) 41.
[252] R. Vrana, D. Koutny, D. Palousek, L. Pantelejev, J. Jaros, T. Zikmund, J. Kaiser, Selective laser melting strategy for fabrication of thin struts useable in lattice structures, Materials 11 (2018) 1763.
[253] S.L. Sing, F.E. Wiria, W.Y. Yeong, Selective laser melting of lattice structures: a statistical approach to manufacturability and mechanical behavior, Robot. Comput. Integrated Manuf. 49 (2018) 170–180.
[254] E. Maleki, S. Bagherifard, M. Bandini, M. Guagliano, Surface post-treatments for metal additive manufacturing: progress, challenges, and opportunities, Addit. Manuf. 37 (2020), 101619.
[255] C. Yan, L. Hao, A. Hussein, P. Young, Ti-6Al-4V triply periodic minimal surface structures for bone implants fabricated *via* selective laser melting, J. Mech. Behav. Biomed. Mater. 51 (2015) 61–73.
[256] F. Calignano, Design optimization of supports for overhanging structures in aluminum and titanium alloys by selective laser melting, Mater. Des. 64 (2014) 203–213.
[257] A. Moussa, D. Melancon, A. El Elmi, D. Pasini, Topology optimization of imperfect lattice materials built with process-induced defects *via* powder bed fusion, Addit. Manuf. 37 (2020), 101608.
[258] G. Campoli, M.S. Borleffs, S.A. Yavari, R. Wauthle, H. Weinans, A.A. Zadpoor, Mechanical properties of open-cell metallic biomaterials manufactured using additive manufacturing, Mater. Des. 49 (2013) 957–965.
[259] B. Lozanovski, D. Downing, P. Tran, D. Shidid, M. Qian, P. Choong, M. Brandt, M. Leary, A Monte Carlo simulation-based approach to realistic modelling of additively manufactured lattice structures, Addit. Manuf. 32 (2020), 101092.
[260] M. Dallago, F. Zanini, S. Carmignato, D. Pasini, M. Benedetti, Effect of the geometrical defectiveness on the mechanical properties of SLM biomedical Ti6Al4V lattices, Procedia Struct. Integrity 13 (2018) 161–167.
[261] S. Arabnejad, B. Johnston, M. Tanzer, D. Pasini, Fully porous 3D printed titanium femoral stem to reduce stress-shielding following total hip arthroplasty, J. Orthop. Res. 35 (2017) 1774–1783.
[262] A. Sarker, M. Leary, K. Fox, Metallic additive manufacturing for bone-interfacing implants, Biointerphases 15 (2020), 050801.
[263] Y.J. Wang, S. Arabnejad, M. Tanzer, D. Pasini, Hip implant design with three-dimensional porous architecture of optimized graded density, J. Mech. Des. 140 (2018), 111406.
[264] D. Mahmoud, M.A. Elbestawi, Lattice structures and functionally graded materials applications in additive manufacturing of orthopedic implants: a review, J. Manuf. Mater. Process. 1 (2017) 13.
[265] G. Welsch, R. Boyer, E. Collings, Materials Properties Handbook: Titanium Alloys, ASM international, 1993.
[266] P. Xiu, Z. Jia, J. Lv, C. Yin, Y. Cheng, K. Zhang, C. Song, H. Leng, Y. Zheng, H. Cai, Z. Liu, Tailored surface treatment of 3D printed porous Ti6Al4V by microarc oxidation for enhanced osseointegration *via* optimized bone in-growth patterns and interlocked bone/implant interface, ACS Appl. Mater. Interfaces 8 (2016) 17964–17975.

[267] S. Guo, Y. Lu, S. Wu, L. Liu, M. He, C. Zhao, Y. Gan, J. Lin, J. Luo, X. Xu, J. Lin, Preliminary study on the corrosion resistance, antibacterial activity and cytotoxicity of selective-laser-melted Ti6Al4V-xCu alloys, Mater. Sci. Eng. C 72 (2017) 631–640.
[268] Y.J. Liu, H.L. Wang, S.J. Li, S.G. Wang, W.J. Wang, W.T. Hou, Y.L. Hao, R. Yang, L.C. Zhang, Compressive and fatigue behavior of beta-type titanium porous structures fabricated by electron beam melting, Acta Mater. 126 (2017) 58–66.
[269] M. Nakatani, H. Masuo, Y. Tanaka, Y. Murakami, in: Effect of Surface Roughness on Fatigue Strength of Ti-6Al-4V Alloy Manufactured by Additive Manufacturing, Fatigue Design 2019, International Conference on Fatigue Design, eighth ed., 2019, pp. 294–301.
[270] F.S.L. Bobbert, K. Lietaert, A.A. Eftekhari, B. Pouran, S.M. Ahmadi, H. Weinans, A. A. Zadpoor, Additively manufactured metallic porous biomaterials based on minimal surfaces: a unique combination of topological, mechanical, and mass transport properties, Acta Biomater. 53 (2017) 572–584.
[271] K. Lietaert, A. Cutolo, D. Boey, B. Van Hooreweder, Fatigue life of additively manufactured Ti6Al4V scaffolds under tension-tension, tension-compression and compression-compression fatigue load, Sci. Rep. 8 (2018) 4957.
[272] P. Zhang, A.N. He, F. Liu, K.F. Zhang, J.J. Jiang, D.Z. Zhang, Evaluation of low cycle fatigue performance of selective laser melted titanium alloy Ti-6Al-4V, Metals 9 (2019) 1041.
[273] H.E. Burton, N.M. Eisenstein, B.M. Lawless, P. Jamshidi, M.A. Segarra, O. Addison, D.E.T. Shepherd, M.M. Attallah, L.M. Grover, S.C. Cox, The design of additively manufactured lattices to increase the functionality of medical implants, Mater. Sci. Eng. C 94 (2019) 901–908.
[274] F. Aljenaei, I. Catelas, H. Louati, P.E. Beaule, M. Nganbe, Effects of hip implant modular neck material and assembly method on fatigue life and distraction force, J. Orthop. Res. 35 (2017) 2023–2030.
[275] M. Armentia, M. Abasolo, I. Coria, J. Albizuri, Fatigue design of dental implant assemblies: a nominal stress approach, Metals 10 (2020) 744.
[276] G. Asala, J. Andersson, O.A. Ojo, Improved dynamic impact behaviour of wire-arc additive manufactured ATI 718 Plus, Mater. Sci. Eng., A 738 (2018) 111–124.
[277] G. Puppala, A. Moitra, S. Sathyanarayanan, R. Kaul, G. Sasikala, R.C. Prasad, L. M. Kukreja, Evaluation of fracture toughness and impact toughness of laser rapid manufactured inconel-625 structures and their Co-relation, Mater. Des. 59 (2014) 509–515.
[278] Z. Ozdemir, E. Hernandez-Nava, A. Tyas, J.A. Warren, S.D. Fay, R. Goodall, L. Todd, H. Askes, Energy absorption in lattice structures in dynamics: experiments, Int. J. Impact Eng. 89 (2016) 49–61.
[279] J.A. Harris, R.E. Winter, G.J. McShane, Impact response of additively manufactured metallic hybrid lattice materials, Int. J. Impact Eng. 104 (2017) 177–191.
[280] L.J. Xiao, W.D. Song, Additively-manufactured functionally graded Ti-6Al-4V lattice structures with high strength under static and dynamic loading: experiments, Int. J. Impact Eng. 111 (2018) 255–272.
[281] D.D. Radford, G.J. McShane, V.S. Deshpande, N.A. Fleck, Dynamic compressive response of stainless-steel square honeycombs, J. Appl. Mech. 74 (2007) 658–667.
[282] J. Li, D. Chen, Y. Fan, Evaluation and prediction of mass transport properties for porous implant with different unit cells: a numerical study, BioMed Res. Int. 2019 (2019) 3610785.
[283] S. Van Bael, Y.C. Chai, S. Truscello, M. Moesen, G. Kerckhofs, H. Van Oosterwyck, J.P. Kruth, J. Schrooten, The effect of pore geometry on the *in vitro* biological behavior of human periosteum-derived cells seeded on selective laser-melted Ti6Al4V bone scaffolds, Acta Biomater. 8 (2012) 2824–2834.
[284] S. Ma, Q. Tang, X.X. Han, Q.X. Feng, J. Song, R. Setchi, Y. Liu, Y. Liu, A. Goulas, D.S. Engstrom, Y.Y. Tse, N. Zhen, Manufacturability, mechanical properties, mass-transport properties and biocompatibility of triply periodic minimal surface (TPMS) porous scaffolds fabricated by selective laser melting, Mater. Des. 195 (2020), 109034.
[285] S.J. Hollister, Scaffold design and manufacturing: from concept to clinic, Adv. Mater. 21 (2009) 3330–3342.
[286] A.A. Zadpoor, Additively manufactured porous metallic biomaterials, J. Mater. Chem. B 7 (2019) 4088–4117.
[287] S. Truscello, G. Kerckhofs, S. Van Bael, G. Pyka, J. Schrooten, H. Van Oosterwyck, Prediction of permeability of regular scaffolds for skeletal tissue engineering: a combined computational and experimental study, Acta Biomater. 8 (2012) 1648–1658.
[288] L. Wu, P. Shrestha, M. Iapichino, Y. Cai, B. Kim, B. Stoeber, Characterization method for calculating diffusion coefficient of drug from polylactic acid (PLA) microneedles into the skin, J. Drug Deliv. Sci. Technol. 61 (2021), 102192.
[289] A.A. Zadpoor, Bone tissue regeneration: the role of scaffold geometry, Biomater. Sci. 3 (2015) 231–245.
[290] X.Y. Zhang, G. Fang, L.L. Xing, W. Liu, J. Zhou, Effect of porosity variation strategy on the performance of functionally graded Ti-6Al-4V scaffolds for bone tissue engineering, Mater. Des. 157 (2018) 523–538.
[291] D. Ali, S. Sen, Finite element analysis of mechanical behavior, permeability and fluid induced wall shear stress of high porosity scaffolds with gyroid and lattice-based architectures, J. Mech. Behav. Biomed. Mater. 75 (2017) 262–270.
[292] K. Kapat, P.K. Srivas, A.P. Rameshbabu, P.P. Maity, S. Jana, J. Dutta, P. Majumdar, D. Chakrabarti, S. Dhara, Influence of porosity and pore-size distribution in Ti6Al4V foam on physicomechanical properties, osteogenesis, and quantitative validation of bone ingrowth by micro-computed tomography, ACS Appl. Mater. Interfaces 9 (2017) 39235–39248.
[293] P.O. Glantz, G. Ryge, M.D. Jendresen, K. Nilner, Quality of extensive fixed prosthodontics after five years, J. Prosthet. Dent 52 (1984) 475–479.
[294] B.E. Pjetursson, K. Tan, N.P. Lang, U. Bragger, M. Egger, M. Zwahlen, A systematic review of the survival and complication rates of fixed partial dentures (FPDS) after an observation period of at least 5 years, Clin. Oral Implants Res. 15 (2004) 625–642.
[295] G. Marinelli, F. Martina, S. Ganguly, S. Williams, Grain refinement in an unalloyed tantalum structure by combining Wire+Arc additive manufacturing and vertical cold rolling, Addit. Manuf. 32 (2020), 101009.
[296] R. Ding, Z. Guo, A. Wilson, Microstructural evolution of a Ti-6Al-4V alloy during thermomechanical processing, Mater. Sci. Eng., A 327 (2002) 233–245.
[297] R. Filip, K. Kubiak, W. Ziaja, J. Sieniawski, The effect of microstructure on the mechanical properties of two-phase titanium alloys, J. Mater. Process. Technol. 133 (2003) 84–89.
[298] K. Vanmeensel, K. Lietaert, B. Vrancken, S. Dadbakhsh, X. Li, J.-P. Kruth, P. Krakhmalev, I. Yadroitsev, J. Van Humbeeck, Additively manufactured metals for medical applications, in: J. Zhang, Y.-G. Jung (Eds.), Addit. Manuf., Butterworth-Heinemann, 2018, pp. 261–309.
[299] T.C. Dzogbewu, L. Monaheng, J. Els, I. van Zyl, W. Du Preez, I. Yadroitsava, I. Yadroitsev, in: Evaluation of the Compressive Mechanical Properties of Cellular Dmls Structures for Biomedical Applications, 17th Annual Conference of the Rapid Product Development Association of South Africa, 2016.
[300] M. Kanayama, B.W. Cunningham, C.J. Haggerty, K. Abumi, K. Kaneda, P. C. McAfee, *In vitro* biomechanical investigation of the stability and stress-shielding effect of lumbar interbody fusion devices, J. Neurosurg. 93 (2000) 259–265.
[301] A. Nouri, P.D. Hodgson, C.e. Wen, Biomimetic Porous Titanium Scaffolds for Orthopaedic and Dental Applications, InTech, 2010.
[302] H. Attar, L. Lober, A. Funk, M. Calin, L.C. Zhang, K.G. Prashanth, S. Scudino, Y. S. Zhang, J. Eckert, Mechanical behavior of porous commercially pure Ti and Ti-TiB composite materials manufactured by selective laser melting, Mater. Sci. Eng., A 625 (2015) 350–356.
[303] H. Attar, S. Ehtemam-Haghighi, D. Kent, M.S. Dargusch, Recent developments and opportunities in additive manufacturing of titanium-based matrix composites: a review, Int. J. Mach. Tool Manufact. 133 (2018) 85–102.
[304] Y. Li, C. Yang, H. Zhao, S. Qu, X. Li, Y. Li, New developments of Ti-based alloys for biomedical applications, Materials 7 (2014) 1709–1800.
[305] S. Dadbakhsh, M. Speirs, G. Yablokova, J.-P. Kruth, J. Schrooten, J. Luyten, J. Van Humbeeck, in: Microstructural Analysis and Mechanical Evaluation of Ti-45Nb Produced by Selective Laser Melting towards Biomedical Applications, TMS 2015 144th Annual Meeting & Exhibition, Springer International Publishing, Cham, 2016, pp. 421–428.
[306] D. Carluccio, C. Xu, J. Venezuela, Y. Cao, D. Kent, M. Bermingham, A.G. Demir, B. Previtali, Q. Ye, M. Dargusch, Additively manufactured iron-manganese for biodegradable porous load-bearing bone scaffold applications, Acta Biomater. 103 (2020) 346–360.
[307] C. Shuai, C. He, G. Qian, A. Min, Y. Deng, W. Yang, X. Zang, Mechanically driving supersaturated Fe–Mg solid solution for bone implant: preparation, solubility and degradation, Composites, Part B 207 (2021), 108564.
[308] C. Fang, H. Cai, E. Kuong, E. Chui, Y.C. Siu, T. Ji, I. Drstvensek, Surgical applications of three-dimensional printing in the pelvis and acetabulum: from models and tools to implants, Unfallchirurg 122 (2019) 278–285.
[309] T. Bedir, S. Ulag, C.B. Ustundag, O. Gunduz, 3D bioprinting applications in neural tissue engineering for spinal cord injury repair, Mater. Sci. Eng. C 110 (2020), 110741.
[310] K.S. Straley, C.W. Foo, S.C. Heilshorn, Biomaterial design strategies for the treatment of spinal cord injuries, J. Neurotrauma 27 (2010) 1–19.
[311] B. Shrestha, K. Coykendall, Y.C. Li, A. Moon, P. Priyadarshani, L. Yao, Repair of injured spinal cord using biomaterial scaffolds and stem cells, Stem Cell Res. Ther. 5 (2014) 1–11.
[312] A. Warburton, S.J. Girdler, C.M. Mikhail, A. Ahn, S.K. Cho, Biomaterials in spinal implants: a review, Neurospine 17 (2020) 101–110.
[313] N.A. Che Lah, M.H. Hussin, Titanium and titanium based alloys as metallic biomaterials in medical applications-spine implant case study, Pertanika J. Sci. & Technol 27 (2019).
[314] M. Girolami, S. Boriani, S. Bandiera, G. Barbanti-Brodano, R. Ghermandi, S. Terzi, G. Tedesco, G. Evangelisti, V. Pipola, A. Gasbarrini, Biomimetic 3D-printed custom-made prosthesis for anterior column reconstruction in the thoracolumbar spine: a tailored option following En bloc resection for spinal tumors : preliminary results on a case-series of 13 patients, Eur. Spine J. 27 (2018) 3073–3083.
[315] K. Willemsen, R. Nizak, H.J. Noordmans, R.M. Castelein, H. Weinans, M.C. Kruyt, Challenges in the design and regulatory approval of 3D-printed surgical implants: a two-case series, Lancet Digit. Health 1 (2019) e163–e171.
[316] G. Zheng, W. Tian, X. Zhuang, Intelligent Orthopaedics: Artificial Intelligence and Smart Image-Guided Technology for Orthopaedics, Springer, 2018.
[317] J. Yang, H. Cai, J. Lv, K. Zhang, H. Leng, C. Sun, Z. Wang, Z. Liu, *In vivo* study of a self-stabilizing artificial vertebral body fabricated by electron beam melting, Spine 39 (2014) E486–E492.
[318] K.S. Chung, D.A. Shin, K.N. Kim, Y. Ha, D.H. Yoon, S. Yi, Vertebral reconstruction with customized 3-dimensional-printed spine implant replacing large vertebral defect with 3-year follow-up, World Neurosurg 126 (2019) 90–95.
[319] S. Jindal, F. Manzoor, N. Haslam, E. Mancuso, 3D printed composite materials for craniofacial implants: current concepts, challenges and future directions, Int. J. Adv. Manuf. Technol. 112 (2020) 635–653.
[320] K. Moiduddin, S. Darwish, A. Al-Ahmari, S. ElWatidy, A. Mohammad, W. Ameen, Structural and mechanical characterization of custom design cranial implant created using additive manufacturing, Electron. J. Biotechnol. 29 (2017) 22–31.

[321] R. Yan, D. Luo, H. Huang, R. Li, N. Yu, C. Liu, M. Hu, Q. Rong, Electron beam melting in the fabrication of three-dimensional mesh titanium mandibular prosthesis scaffold, Sci. Rep. 8 (2018) 750.
[322] X. Chen, J.K. Possel, C. Wacongne, A.F. van Ham, P.C. Klink, P.R. Roelfsema, 3D printing and modelling of customized implants and surgical guides for non-human primates, J. Neurosci. Methods 286 (2017) 38–55.
[323] R.X. Du, Y.X. Su, Y. Yan, W.S. Choi, W.F. Yang, C.Y. Zhang, X.S. Chen, J.P. Curtin, J.L. Ouyang, B.T. Zhang, A systematic approach for making 3D-printed patient-specific implants for craniomaxillofacial reconstruction, Engineering 6 (2020) 1291–1301.
[324] D. Buser, L. Sennerby, H. De Bruyn, Modern implant dentistry based on osseointegration: 50 Years of progress, current trends and open questions, Periodontol 2000 (73) (2017) 7–21.
[325] D.R. Dixon, R.M. London, Restorative design and associated risks for peri-implant diseases, Periodontol 2000 (81) (2019) 167–178.
[326] Y. Letourneau, R. Perusse, H. Buithieu, Oral manifestations of Ehlers-danlos syndrome, J. Can. Dent. Assoc. 67 (2001) 330–334.
[327] G. Schmalz, P. Garhammer, Biological interactions of dental cast alloys with oral tissues, Dent. Mater. 18 (2002) 396–406.
[328] Y.Z. Xiong, W. Wang, R.N. Gao, H. Zhang, L.L. Dong, J.W. Qin, B.B. Wang, W. T. Jia, X. Li, Fatigue behavior and osseointegration of porous Ti-6Al-4V scaffolds with dense core for dental application, Mater. Des. 195 (2020), 108994.
[329] I.V. Okulov, A.S. Volegov, H. Attar, M. Bonisch, S. Ehtemam-Haghighi, M. Calin, J. Eckert, Composition optimization of low modulus and high-strength tinb-based alloys for biomedical applications, J. Mech. Behav. Biomed. Mater. 65 (2017) 866–871.
[330] E. Bassoli, L. Denti, Assay of secondary anisotropy in additively manufactured alloys for dental applications, Materials 11 (2018) 1831.
[331] M. Revilla-Leon, N. Al-Haj Husain, M.M. Methani, M. Ozcan, Chemical composition, surface roughness, and ceramic bond strength of additively manufactured cobalt-chromium dental alloys, J. Prosthet. Dent 125 (2021) 825–831.
[332] M.W. McDonald, W.S. Gora, S.G. Stevenson, N.J. Weston, D.P. Hand, Practical implementation of laser polishing on additively manufactured metallic components, J. Laser Appl. 32 (2020), 042019.
[333] H.W. Roberts, D.W. Berzins, B.K. Moore, D.G. Charlton, Metal-ceramic alloys in dentistry: a review, J. Prosthodont. 18 (2009) 188–194.
[334] T. Akova, Y. Ucar, A. Tukay, M.C. Balkaya, W.A. Brantley, Comparison of the bond strength of laser-sintered and cast base metal dental alloys to porcelain, Dent. Mater. 24 (2008) 1400–1404.
[335] M. Khan, P. Dickens, Selective laser melting (SLM) of pure gold for manufacturing dental crowns, Rapid Prototyp. J. 20 (2014) 471–479.
[336] F.X. Azpiazu-Flores, D.J. Lee, F. Zheng, The use of selective laser melting in the fabrication of maxillary and mandibular metal base complete dentures for a patient with Ehlers-danlos syndrome: a clinical report, J. Prosthet. Dent 124 (2020) 509–513.
[337] G. Asensio, B. Vazquez-Lasa, L. Rojo, Achievements in the topographic design of commercial titanium dental implants: towards anti-peri-implantitis surfaces, J. Clin. Med. 8 (2019) 1982.
[338] S.R. Knight, R. Aujla, S.P. Biswas, Total hip arthroplasty - over 100 Years of operative history, Orthop. Rev. 3 (2011) e16.
[339] C. Weller, R. Kleer, F.T. Piller, Economic implications of 3D printing: market structure models in light of additive manufacturing revisited, Int. J. Prod. Econ. 164 (2015) 43–56.
[340] M. Javaid, A. Haleem, Current status and challenges of additive manufacturing in orthopaedics: an overview, J. Clin. Orthop. Trauma. 10 (2019) 380–386.
[341] D. Miljanovic, M. Seyedmahmoudian, A. Stojcevski, B. Horan, Design and fabrication of implants for mandibular and craniofacial defects using different medical-additive manufacturing technologies: a review, Ann. Biomed. Eng. 48 (2020) 2285–2300.
[342] Y. Xia, Z.C. Feng, C. Li, H. Wu, C. Tang, L. Wang, H. Li, Application of additive manufacturing in customized titanium mandibular implants for patients with oral tumors, Oncol. Lett. 20 (2020) 51.
[343] F. Grecchi, P.A. Zecca, A. Macchi, A. Mangano, F. Riva, E. Grecchi, C. Mangano, Full-digital Workflow for fabricating a custom-made direct metal laser sintering (DMLS) mandibular implant: a case report, Int. J. Environ. Res. Publ. Health 17 (2020) 2693.
[344] M. Lowther, S. Louth, A. Davey, A. Hussain, P. Ginestra, L. Carter, N. Eisenstein, L. Grover, S. Cox, Clinical, industrial, and research perspectives on powder bed fusion additively manufactured metal implants, Addit. Manuf. 28 (2019) 565–584.
[345] D.I. Wimpenny, P.M. Pandey, L.J. Kumar, Advances in 3D Printing & Additive Manufacturing Technologies, Springer, 2017.
[346] E. Atzeni, A. Salmi, Evaluation of additive manufacturing (AM) techniques for the production of metal-ceramic dental restorations, J. Manuf. Process. 20 (2015) 40–45.
[347] R.F. MacBarb, D.P. Lindsey, S.A. Woods, P.A. Lalor, M.I. Gundanna, S.A. Yerby, Fortifying the bone-implant interface Part 2: an *in vivo* evaluation of 3D-printed and TPS-coated triangular implants, Internet J. Spine Surg. 11 (2017) 1–13.
[348] S. Davies, FDA-approved 3D Printed Implants Just the Start as Osseus Prepares to Go International, Rapid News Publications Ltd, TCT Magazine, 2018. https://www.tctmagazine.com/additive-manufacturing-3d-printing-news/fda-3d-printed-implants-osseus-international/.
[349] B. Sullivan, Stryker's 3D Printed Tritanium TL Curved Posterior Lumbar Cage Receives FDA 510(k) Clearance, Rapid News Publications Ltd, TCT Magazine, 2018. https://www.tctmagazine.com/additive-manufacturing-3d-printing-news/stryker-3d-printed-tritanium-tl-curved-posterior-lumbar-cage-fda/.
[350] A.R. Thryft, First 3D-printed titanium cranial implant to get FDA approval, in: B. L.V. Lundin (Ed.), Informa Markets Design News, 2016. https://www.designnews.com/medical/first-3d-printed-titanium-cranial-implant-get-fda-approval.
[351] D. Sher, FDA Approves First Patient-specific, 3D Printed Talus Implant in the US, 3dpbm, 3D Printing Media Network, 2021. https://www.3dprintingmedia.network/fda-approves-first-patient-specific-3d-printed-talus-spacer-implant-in-the-us/.
[352] A. Strömbergsson, NGMedical Cleared by FDA for AM-Made Cervical BEE Cage, 3dpbm, 3D Printing Media Network, 2021. https://www.3dprintingmedia.network/ngmedical-cleared-by-fda-for-am-made-cervical-bee-cage/.
[353] S.L. Sing, C.N. Kuo, C.T. Shih, C.C. Ho, C.K. Chua, Perspectives of using machine learning in laser powder bed fusion for metal additive manufacturing, Virtual Phys. Prototyp. 16 (2021) 372–386.
[354] J. An, C.K. Chua, V. Mironov, Application of machine learning in 3D bioprinting: focus on development of big data and digital twin, Int. J. Bioprinting 7 (2021), 342-342.
[355] H. Montazerian, A. Rashidi, A.S. Milani, M. Hoorfar, Integrated sensors in advanced composites: a critical review, Crit. Rev. Solid State Mater. Sci. 45 (2020) 187–238.
[356] E. Jabari, F. Liravi, E. Davoodi, L. Lin, E. Toyserkani, High speed 3D material-jetting additive manufacturing of viscous graphene-based ink with high electrical conductivity, Addit. Manuf. 35 (2020), 101330.
[357] E. Davoodi, H. Fayazfar, F. Liravi, E. Jabari, E. Toyserkani, Drop-on-Demand high-speed 3D printing of flexible milled carbon fiber/silicone composite sensors for wearable biomonitoring devices, Addit. Manuf. 32 (2020), 101016.
[358] H. Montazerian, A. Rashidi, A. Dalili, H. Najjaran, A.S. Milani, M. Hoorfar, Graphene-coated spandex sensors embedded into silicone sheath for composites health monitoring and wearable applications, Small 15 (2019), 1804991.
[359] H. Montazerian, A. Dalili, A.S. Milani, M. Hoorfar, Piezoresistive sensing in chopped carbon fiber embedded pdms yarns, Composites, Part B 164 (2019) 648–658.
[360] N. Ashammakhi, S. Ahadian, C. Xu, H. Montazerian, H. Ko, R. Nasiri, N. Barros, A. Khademhosseini, Bioinks and bioprinting technologies to make heterogeneous and biomimetic tissue constructs, Mater. Today Bio 1 (2019), 100008.
[361] E. Davoodi, E. Sarikhani, H. Montazerian, S. Ahadian, M. Costantini, W. Swieszkowski, S.M. Willerth, K. Walus, M. Mofidfar, E. Toyserkani, A. Khademhosseini, N. Ashammakhi, Extrusion and microfluidic-based bioprinting to fabricate biomimetic tissues and organs, Adv. Mater. Technol. 5 (2020), 1901044.
[362] H. Montazerian, A. Baidya, R. Haghniaz, E. Davoodi, S. Ahadian, N. Annabi, A. Khademhosseini, P.S. Weiss, Stretchable and bioadhesive gelatin methacryloyl-based hydrogels enabled by in situ dopamine polymerization, ACS Appl. Mater. Interfaces 13 (2021) 40290–40301.